SAPIENZA
UNIVERSITÀ DI ROMA

Reconstruction of the intensive variables and magmatic architecture of Vulcano Island (Aeolian Arc, Italy)

PhD Thesis

Flavia Palummo
XXXIV ciclo

Supervisor:
Prof. Silvio Mollo

Co-Supervisor:
Dr. Gianfilippo De Astis

Contents

Introduction

Over the last few decades, combining advanced of petrological and geochemical observations has greatly improved our understanding of the development of entire magma plumbing systems, allowing the identification of zones of melt accumulation, crystal mush development, and magma migration. Thus, the study of active volcanoes provides a lot of data that must be interpreted in light of understand pre-eruptive dynamics (e.g., fractional crystallization, magma mixing, assimilation of host rock by magma, degassing and ascent processes). Models concerning the internal structure and magma evolution of active volcanoes are important to establish reliable monitoring strategies and to forecast volcanic eruptions. Following this line of reasoning, the microanalysis of major/trace elements, as well as the characterization of intensive variables can be used to estimate the depth and temperature in which crystallization took place in polybaric magmatic chambers and to reconstruct the evolution of plumbing systems.

In this study, I have determined the magmatic variables (e.g., pressure, temperature, volatile content, and oxygen fugacity) governing the plumbing system evolution at Vulcano Island and how such variables change with time. In the first part of this PhD thesis, I present new mineralogical and petrological data on olivine, clinopyroxene, plagioclase, and titanomagnetite phenocrysts from fifteen eruptive products (scoriae, lava flows, lava domes, and lava dykes) over a long period of time, from 54 to 8 ka. The intensive variables driving the crystallization path of magmas were reconstructed through mineral-melt equilibrium and thermodynamic models, as well as barometers, thermometers, hygrometers and oxygen barometers. The resulting P-T-H_2O-fO_2 constraints have been also integrated with thermodynamic simulations reproducing the liquid line of descent of magma and major/trace element modeling, in order to better understand the differentiation processes operating at Vulcano Island and to reconstruct the plumbing system architecture.

In the second part of this PhD thesis, the compositional information recorded in chemically zoned clinopyroxene phenocrysts from the last ~54 ka of eruptive activity have been used to unravel the most effective pre-eruptive volcanic processes driving the geochemical evolution of the plumbing system. Although clinopyroxene is an important recorder of differentiation mechanisms and its complex texture may help to reconstruct the recharge dynamics of magma reservoirs, no studies have yet investigated the zoning patterns of clinopyroxene at Vulcano Island. For this reason, microanalytical data and trace element modeling of clinopyroxene phenocrysts from twenty-one basaltic-to-rhyolitic products have been combined. The textural and compositional changes of phenocrysts shed light on the physico-chemical changes of magma under the effects of closed- and open-system processes. Temporal informations of magmatic processes are also locked within the chemical zoning profiles of clinopyroxene. Constraining the timescales of pre-eruptive magmatic processes allowed to understand magma dynamics and the potential triggers for volcanic eruptions.

Petrological and geochemical modeling of magmas erupted at Vulcano Island in the period 54-8 ka: Quantitative constraints on the sub-volcanic architecture of the plumbing system

[1]Flavia Palummo, [1,2]Silvio Mollo, [2]Gianfilippo De Astis, [2]Flavio Di Stefano, [2]Manuela Nazzari, [2]Piergiorgio Scarlato

[1]Department of Earth Sciences, Sapienza - University of Rome, P. le Aldo Moro 5, 00185 Roma, Italy

[2]Istituto Nazionale di Geofisica e Vulcanologia - Department Roma 1, Via di Vigna Murata 605, 00143 Roma, Italy

Abstract

In this study, we present new mineralogical and petrological data from fifteen eruptive products erupted at Vulcano Island (Aeolian Arc, Italy) over a period of time from 54 to 8 ka and representative of the Eruptive Epochs from 5 to 8 of this volcanic system. These rocks show shoshonitic (SHO) to high-K calc-alkaline (HKCA) affinity, with compositions changing from primitive basalts-shoshonites ($Mg\#_{35-60}$) to intermediate latites ($Mg\#_{32-54}$) to evolved trachytes-rhyolites ($Mg\#_{23-40}$). The intensive variables driving the crystallization path of magmas were reconstructed through mineral-melt equilibrium and thermodynamic models, as well as barometers, thermometers, hygrometers and oxygen barometers. The stability of olivine (Fo_{59-91}), as first phase on the liquidus, is more favored at low-*P* (100-300 MPa) and high-H_2O (4 wt.%) contents dissolved in the melt. Afterwards, the melt is co-saturated with clinopyroxene ($Mg\#_{92}$, diopside), whose composition progressively evolves ($Mg\#_{71}$, augite) as the temperature decreases to 1100 °C. The crystallization pressure recorded by clinopyroxene decreases from basalts (550-750 MPa) to shoshonites-latites-trachytes (100-450 MPa) to rhyolites (~50 MPa). The melt-H_2O content (0.5-4.2 wt.%) is sensitive to either pressure or melt composition, thereby controlling the plagioclase stability and chemistry (An_{13-77}) within a thermal path of ~860-1100 °C. Titanomagnetite (Usp_{11-39}) equilibrates with progressively more oxidized melts as the magma composition changes from basalt (ΔQFM+1.5) to rhyolite (ΔQFM+3). Mass balance calculations and trace element modeling indicate that basaltic to trachytic magmas are prevalently controlled by fractional crystallization processes, in concert with variable degrees of assimilation of crustal rocks. Conversely, rhyolitic and highly differentiated trachytic magmas are generated by extraction of interstitial melts from shallow mush zones dominated by feldspar and titanomagnetite saturation. We conclude that the architecture of the plumbing system at Vulcano Island is characterized by multiple reservoirs

in which compositionally distinct magmas pond and undergo polybaric-polythermal differentiation, before erupting to the surface.

1. Introduction

Vulcano Island is an active volcano of the Aeolian Archipelago (Southern Tyrrhenian Sea, Italy) characterized by high-K calc-alkaline (HKCA), shoshonitic (SHO), and potassic (KS) rocks, with variable degree of evolution from basalt to rhyolite (Keller, 1980; De Astis, 1997a).

In the last decades, the geochemical and petrological evolution of Vulcano Island has been associated with complex magma differentiation processes, frequently controlled by open system phenomena due to either magma mixing and contamination within the crust (De Astis et al. 1997a, 2013; Gioncada et al., 1998, 2003; Frezzotti et al., 2004, Perugini et al., 2007; Piochi et al., 2009; Forni et al., 2015; Nicotra et al., 2018; Bullock et al., 2019) or partial melting and metasomatism of a heterogeneous mantle source (Ellam and Harmon, 1990; De Astis et al., 2000; Pinarelli et al., 2019). One important outcome from these studies is that the degree of chemical evolution of magmas increases over time, although with some exceptions within the lifespan of the volcanic system (De Astis et al., 2013). Generally, the eruptive products are characterized by potassium and incompatible trace element enrichments from the older mafic (basaltic) activity of Primordial Vulcano to the younger silicic (rhyolitic) eruptions which occurred at 1888-90 CE. This time-related compositional shift has been attributed to the uprising of distinct magmatic reservoirs towards shallower crustal levels, in which resident magmas tend to differentiate, as the intensity and efficacy of mafic recharges decreases (De Astis et al. 1997a; Zanon et al. 2003; Frezzotti and Peccerillo 2004).

The most recent petrological studies focus on the last 1000 years of activity at Vulcano Island, accounting for the crystallization conditions of rhyolitic magmas at La Fossa cone and the genetic relationships between more or less differentiated products with marked potassium enrichments (Vetere et al., 2015; Nicotra et al., 2018; Bullock et al., 2019; Rossi et al., 2019). The physical and chemical characterization of these historic silicic eruptions has attracted particular attention because of the importance of defining the most likely scenario for a future eruption (cf. Costa et al., 2020). However, there is no detailed and systematic knowledge on the polybaric and polythermal evolution of earlier magmatic reservoirs feeding mafic-to-silicic eruptions with both HCKCA and SHO affinities. To remedy this paucity of information, we have examined mineral and bulk rock compositions of scoriae, lava flows, lava domes, and lava dykes outpoured at Vulcano Island over an eruptive period of time from 54 ka to 8 ka. These rock samples were selected on the basis of their dissimilar volcanological and petrological attributes, as they represent the most important modifications of magma during the volcanic system evolution. Through the application of mineral-melt equilibrium models, barometers, thermometers, hygrometers, and oxygen barometers, we have obtained new and more accurate indications on the pre-eruptive crystallization conditions of the studied products. The resulting P-T-H_2O-fO_2 constraints have been also integrated with thermodynamic simulations, reproducing the liquid line of descent of magma and bulk rock major and trace element modeling in order to elucidate better the differentiation processes operating in distinct sub-volcanic magma reservoirs and to ultimately reconstruct the plumbing system architecture of Vulcano Island.

2. Geological background

Vulcano Island is an active volcanic system located in the southernmost sector of the Aeolian Archipelago (Fig. 1), a Quaternary volcanic archipelago consisting of seven islands and nine seamounts forming a ring-like structure, whose northwestern sector lies on the oceanic crust of the Tyrrhenian abyssal plain and eastern and southern sectors on ~18-25 km thick continental crust of the Calabro-Peloritano basement. Lipari, Salina and Vulcano have developed inside a graben-like structure controlled by the NNW-SSE strike-slip Tindari-Letojanni fault system (Gioncada et al., 2003) and they form a NNW-SSE-oriented volcanic belt that cross-cuts the archipelago in its central sector (De Astis et al., 1997a). Vulcano Island has a total surface area of ~22 km^2, its base lies at an average depth of ~1 km b.s.l. and the maximum height is ~499 m a.s.l. at Monte Aria (De Astis et al., 2013 and references therein).

Magmatism of Aeolian Volcanoes is related to the subduction of the Ionian plate under the Calabro-Peloritan Arc, with typical calc-alkaline eruptive products. Seismic data reveals the presence of a NW-dipping Benioff-Wadati zone (Ellam and Harmon, 1990), presently in the eastern sector. Vulcano Island started its activity 127 ka ago with the early Primordial Vulcano structure (Fig. 1), whereas its last eruption occurred from August 1888 to March 1890 at La Fossa cone (Keller, 1980). This is a 391-m-high tuff cone mainly formed through phreatomagmatic eruptions and minor lava flow effusions (Dellino et al., 2011). The peninsula of Vulcanello (Fig. 1) has been formed as a new islet which began to form Roman Times. It represents a northernmost structure located along the northern border of La Fossa caldera, consisting of a lava platform and three nested, ENE-WSW-aligned scoria cones (De Astis et al., 1997a, 2013; Davì et al., 2009).

The most recent and complete geologic study on Vulcano geology was published by De Astis et al. (2013), together with a 1:10000 scale geological map that can be accessed online at http://www.geolsoc.org.uk/Memoir37-electronic. In order to fully associate the products

studied in this work to the whole chrono-stratigraphy of Vulcano Island (Fig. 1), we conveniently refer to this geological map, where eight Eruptive Epochs characterize the whole Vulcano eruptive history. The Eruptive Epochs (Fig. 1) represent the principal building stages of the volcanic edifice interrupted by periods of quiescence sometimes associated with volcano-tectonic collapses. The products that we have studied occur between the final part of Eruptive Epoch 5 (~54-40 ka) and part of the Eruptive Epoch 8 (until ~8 ka), which includes several types of volcanic eruptions. Detailed lithological and age-related features of the studied rocks are reported in the next section, as well as a summary of the main volcanic and volcano-tectonic events.

3. Sample selection

A total of fifteen rock samples, compositionally from basalt to rhyolite, were collected from several strategic sectors and formations outcropping along Vulcano Island, in which the eruptive units were identified on the basis of their different litostratigraphic and compositional characteristics (Fig. 1). More specifically, the rock samples represent, as much as possible, the last Eruptive Epochs 5, 6, 7, and 8 (<53.7±2.6 ka and pre-8 ka; De Astis et al., 2013) of the plumbing system (Fig. 1). The rock samples have been divided in three distinct groups for primitive, intermediate and evolved bulk rock compositions (see below for further details): 1) basalt-shoshonites (VL168/2, VL194/1, VL168/12, VL230/7, VL209A/2, and VL180), 2) latites (VL175B/1, VL144/2, and VL213B/2), and 3) trachyte-rhyolites (VL229/6, VL175C/3, VL183/10, VL181, VL182/1, and VL17811A). Three rocks, corresponding to Eruptive Epoch 5 (from 53.7±2.6 to ~40 ka), are from the Strombolian fallout deposit of La Sommata Formation (VL194/1, VL168/2, and VL168/12), which consists of black basaltic scoria (De Astis et al., 2013; see Fig. 1). Five rocks related to Eruptive Epoch 6 (from ~27 to 21.3±3.4 ka)

were sampled from: Punta di Mastro Minico Formation (VL175B/1, latitic lava flow; 27.9±6.6 ka), Punta del Monaco Formation (VL175C/3, trachytic lava flow; 26.5±2.0 ka), Spiaggia Lunga Formation (VL230/7, shoshonitic scoria; 24.0±5.0 ka), Cala del Formaggio Formation (VL182/1, rhyolitic lava flow; 25.8±2.5 ka), and Quadrara - Faro Vecchio Formation (VL229/6, trachytic scoria; 21.3±3.4 ka). Punta di Mastro Minico Formation corresponds to the earliest scoria and lava flows of Eruptive Epoch 6 exposed in the lower part of the coastal cliff of the northernmost part of Vulcano Island (Fig.1; De Astis et al., 2013). Punta del Monaco e Cala del Formaggio Formation represent scoria and lava coulees of the lower portion of the Monte Lentia dome-field, constructed above the older Punta di Mastro Minico products (De Astis et al., 2013). Spiaggia Lunga and Quadrara - Faro Vecchio Formation are scoria blankets along the western and southern flanks of Primordial Vulcano (Fig. 1; De Astis et al., 2013). Spiaggia Lunga Formation corresponds to Spiaggia Lunga scoria in De Rosa et al. (1988). Three rocks, corresponding to Eruptive Epoch 7 (from 15.5±1.0 to 13.0±3.0 ka), were sampled from Cugni di Molinello Formation (VL144/2, latitic scoria), Monte Lentia Formation (VL17811A, rhyolitic lava; 15.5±1.0 ka) and Casa Lentia Formation (VL183/10, trachytic lava flow; 15.5±1.3 ka). Cugni di Molinello latitic scoriaceous lapilli are interlayered within the Piano Grotte dei Rossi Formation in several outcrops within the area of Il Piano caldera (De Astis et al., 2013). Monte Lentia and Casa Lentia Formations represent lava domes and coulees (De Astis et al., 2013) emplaced in the area of Monte Lentia dome-field (i.e., the Lentia group in Keller, 1980 and Lentia complex in De Astis et al., 1997a). Four rocks related to Eruptive Epoch 8 (<8.5±3.3 ka to Present) were sampled, one from the Carabinieri Formation (VL181, rhyolitic lava dyke; 8.5±3.3 ka) and three from Monte Saraceno Formation (VL209A/2, VL180, and VL213B/2, shoshonitic scoria, shoshonitic lava, and latitic lava, respectively; 8.3±1.6 ka). The Carabinieri Formation consists of three rhyolitic lava domes N-S aligned (De Astis et al., 2013). Monte Saraceno Formation comprises blankets of scoriae and various lava

flows outcropping at the junction between the Il Piano caldera and La Fossa caldera on both sides of the hill (Fig.1; De Astis et al., 2013).

4. Analytical methods

Microchemical analyses on minerals were carried out with an electron probe micro-analyzer (EPMA) installed at the High Pressure - High Temperature (HP-HT) Laboratory of Experimental Volcanology and Geophysics of the Istituto Nazionale di Geofisica e Vulcanologia (INGV) in Rome (Italy), whereas bulk rock analyses for major and trace elements were conducted with inductively coupled plasma optical emission spectrometry (ICP-OES) and inductively coupled plasma mass spectrometry (ICP-MS) at Actlabs (Activation Laboratories Ltd.) in Ancaster (Canada). A detailed description of the analytical equipments and conditions used is reported in the SM1.

5. Results

5.1. Petrography

Lavas and pyroclastic products of the last Eruptive Epochs 5, 6, 7, and 8 of Vulcano exhibit Porphyritic Index (PI = the total phenocrysts content) ranging from 3% to 30%, in agreement with the phenocryst content reported in previous works (De Astis et al., 2013; Mandarano et al., 2016). The mineral assemblage (phenocryst and microphenocryst) consists of olivine (0-5 vol%), clinopyroxene (40-70 vol%), feldspar (30-50 vol%) and titanomagnetite (<5 vol%). Generally, the groundmass consists of the same mineral assemblage, but it varies from microcrystalline (VL168/2, VL194/1, VL168/12, VL230/7, VL209A/2, VL180, VL175B/1, VL213B/2, VL183/1, VL182/1, and VL17811A) to cryptocrystalline (VL144/2,

VL229/6, VL175C/3, and VL181) with large vesicles in more evolved products. Glomerocrysts of clinopyroxene and plagioclase are also frequent, as crystal aggregates with sizes larger than 1-2 mm. In terms of maximum abundance and crystal size, clinopyroxene dominates the mineral association of glomerocrysts.

5.2. Mineral chemistry

Representative chemical analyses of minerals from the studied rock samples are reported in the SM2.

Olivine generally occurs as subhedral to anhedral phenocrysts with sizes varying from 0.5 to 1.5 mm. In terms of Mg-number [Mg# = 100 × molecular MgO / (FeO_{tot} + MgO)], crystal compositions are $Mg\#_{59-91}$. The olivine composition has been classified through the end-members (SM2): forsterite (Fo; Mg_2SiO_4), fayalite (Fa; Fe_2SiO_4), monticellite (Mtc; $CaMgSiO_4$), and kirschsteinite (Kir; $CaFeSiO_4$). Mtc and Kir contents are very low in olivine and do not substantially change within the rock samples. Olivine does not show appreciable core to rim zoning, and its composition ranges from Fo_{59-67} for primitive VL194/1 and VL230/7 samples to Fo_{65-72} for more evolved VL144/2 and VL175C/3 samples (SM2). The most primitive (Fo_{87-91}) olivine phenocrysts are found in sample VL168/12 from La Sommata Formation.

Clinopyroxene is the dominant mineral phase in all the investigated samples, showing euhedral to sub-euhedral habit and crystal size ranging from 0.5 to 3 mm. Most of the clinopyroxene phenocrysts are characterized by normal zonation, with cores ($Mg\#_{75-92}$) more primitive than rims ($Mg\#_{71-83}$). According to Morimoto (1988), clinopyroxene cores are classified as diopside-augite, whereas clinopyroxene rims are prevalently augite and subordinately diopside (SM3). According to the wollastonite (Wo; $Ca_2Si_2O_6$), enstatite (En;

$Mg_2Si_2O_6$) and ferrosilite (Fs; $Fe_2Si_2O_6$) end-members, clinopyroxenes compositions in primitive samples (VL168/2, VL194/1, VL168/12, VL230/7, and VL180) grade from En_{43-49}-Fs_{4-14}-Wo_{41-47} (core) to En_{34-47}-Fs_{8-22}-Wo_{40-50} (rim). In intermediate samples (VL175B/1, VL144/2, and VL213B/2), the composition of clinopyroxene becomes slightly enriched in En and Fs, with En_{41-50}-Fs_{5-15}-Wo_{40-48} (core) and En_{40-47}-Fs_{11-16}-Wo_{40-50} (rim). This compositional change is exacerbated for clinopyroxene phenocrysts from more evolved samples (VL175C/3, VL183/10, VL181, VL182/1, and VL17811A), with En_{43-50}-Fs_{6-14}-Wo_{43-50} (core) and En_{34-47}-Fs_{8-22}-Wo_{34-47} (rim).

Feldspar is the second most abundant mineral phase, showing euhedral tabular habit and crystal size ranging from 0.3 to 2 mm. Plagioclase is the most abundant feldspar, whereas the formation of sanidine is restricted to trachytic (VL182/1 and VL175C/3) and rhyolitic (VL181 and VL17811A) products. Plagioclase is normally zoned with more basic cores classified as bytownite, labradorite, and andesine, and more acid rims classified as labradorite, andesine, and rarely oligoclase to anorthoclase (SM4). Resorption and zonation are evident in a large number of phenocrysts. The anorthite (An; $CaAl_2Si_2O_8$), albite (Ab; $NaAlSi_3O_8$), and orthoclase (Or; $KAlSi_3O_8$) end-members change as follows: 1) from An_{50-77}-Ab_{21-46}-Or_{2-7} (core) to An_{27-60}-Ab_{35-65}-Or_{4-10} (rim) in primitive rock samples (VL194/1, VL168/12, VL230/7, and VL180), 2) from An_{51-63}-Ab_{34-43}-Or_{3-8} (core) to An_{47-62}-Ab_{34-45}-Or_{4-12} (rim) in intermediate rock samples (VL175B/1 and VL144/2), and 3) from An_{39-62}-Ab_{35-57}-Or_{2-5} (core) to An_{13-59}-Ab_{37-71}-Or_{3-16} (rim) in evolved rock samples (VL183/10, VL181, VL182/1, and VL17811A). Sanidine shows crystal size much lower than plagioclase and composition in the range of An_{4-8}-Ab_{24-54}-Or_{38-72}.

Titanomagnetite is the only Ti-Fe oxide found in the studied rock samples (SM5). The crystal habit is generally anhedral with maximum size of 0.3 mm. The ulvospinel (Usp; $TiFe_2O_4$) changes as Usp_{11-39}, Usp_{12-18}, and Usp_{11-34} for primitive (VL194/1, VL230/7, and

VL180), intermediate (VL175B/1, VL144/2, and VL213B/2) and evolved rock samples (VL175C/3, VL183/10, VL181, VL182/1, and VL17811A), respectively. The Fe^{3+}/Fe^{2+} ratio (on the basis of 4 oxygen atoms and 3 cations per formula unit) in titanomagnetite increases from primitive (0.9-1.6) to intermediate and evolved samples (1.0-1.8). The compositions of crystals show appreciable changes in Al_2O_3, MgO, CaO, and Cr_2O_3, with 1.2-7.5 wt.%, 0.7-5.5 wt.%, 0-0.4 wt.%, 0-1.8 wt.%, respectively, for primitive and intermediate samples and 1.6-4.6 wt.%, 0.3-1.9 wt.%, 0-0.2 wt.%, 0.1-0.6 wt.%, respectively, for more evolved samples.

Apatite is also present in a few traces in the most silicic products (VL182/1, VL175C/3, VL181, and VL17811A).

5.3. Bulk rock composition

Bulk rock major and trace element analyses of the studied sample are reported in the SM6.

As documented by previous authors (Keller, 1980; De Astis, 1995; De Astis et al., 1997a; De Astis et al., 2013), the products erupted at Vulcano Island display a wide spectrum of compositions (SM6), ranging from basalt to rhyolite in the total alkali vs. silica (TAS) diagram (Le Bas et al., 1986). Primitive basalts-shoshonites (VL168/2, VL194/1, VL168/12, VL230/7, VL209A/2, and VL180), intermediate latites (VL175B/1, VL144/2, and VL213B/2), and evolved trachytes-rhyolites (VL229/6, VL175C/3, VL183/10, VL181, VL182/1, and VL17811A) from this study have $Mg\#_{35\text{-}60}$, $Mg\#_{32\text{-}54}$, and $Mg\#_{23\text{-}40}$, respectively. The SiO_2 vs. K_2O (SM6) diagram (Peccerillo and Taylor, 1976) shows that most of these products have SHO and HKCA affinities. In particular, VL168/2, VL168/12, and VL230/7 (i.e., Eruptive Epochs 5 and 6) straddle the boundary between the HKCA and SHO series. VL175B/1, VL229/6, VL144/2, VL183/10, VL209A/2, and VL213B/2 (i.e., Eruptive Epochs 6, 7, and 8) are more

openly SHO, whereas VL194/1, VL175C/3, VL182/1, VL17811A, VL181, and VL180 (Eruptive Epochs 5, 6, 7 and 8) are HKCA. In general, for primitive and intermediate bulk rock compositions, Na_2O (2-5 wt.%) and K_2O (2-5 wt.%) progressively increase with increasing SiO_2 (49-57 wt.%). For the evolved products, the total alkali content (8-10 wt.%) remains constrained in a narrow range as the amount of silica further increases (> 62 wt.%) during magma differentiation.

The chondrite-normalized patterns (Sun and McDonough, 1989) of REE (rare earth elements; SM6) exhibits sub-parallel trends, shifting towards progressive REE enrichments from primitive to intermediate to evolved bulk rock compositions. Enrichments in LREE (light rare earth elements) relative to HREE (heavy rare earth elements) are also observed. Bulk rocks are characterized by weak (Eu/Eu* = 0.83-0.92 for VL168/12, VL194/1, VL168/2, VL230/7, and VL180) to strongly (Eu/Eu* = 0.21-0.29 for VL182/1, VL181, and VL178/11a) negative Eu anomalies, in concert with high (La_N/Yb_N = 13.4-18.8) to low (La_N/Yb_N = 10.3-10.7) values of normalized La/Yb ratios. The primordial mantle-normalized pattern (Sun and McDonough, 1989) of trace elements (SM6) shows typical features of arc magmas, with LILE (large ion lithophile elements) to HFSE (high field strength elements) ratios higher than the primitive mantle values. Consistently with this petrogenetic signature, all the products display troughs at Ta, Nb, P, and Ti, as well as lower LILE/HFSE (e.g., Ba/Ta from 1843 to 84) and LREE/HFSE (e.g., La/Ta from 69 to 23) ratios with progressing melt differentiation. The content of incompatible elements (e.g., Rb, La and Nb) increases systematically with SiO_2. The most silicic eruptions from Eruptive Epoch 8 are also considerably enriched in Rb, Nb, Th, U, and Ta. Negative spikes of Ba, Sr, P, and Ti are more marked for the trachytic (VL182/1, VL175C/3, and VL229/6) and rhyolitic (VL17811A and VL181) products, testifying to late-stage crystallization of feldspar + oxide ± apatite. Generally, the concentrations of compatible TE (transition elements), such as Ni (20-180 ppm) and Cr (14-970), decrease from basalt to

rhyolite, in accordance with lower MgO contents. Comparatively, the studied products show an increase in the degree of chemical evolution and incompatible trace element inventory from older to younger eruptions.

6. Discussion

6.1 Magma crystallization conditions

In volcanic rocks, the compositions of phenocrysts and residual melts feeding the crystal growth, change systematically along the differentiation path of magma and under the effect of magma dynamics triggering the late-stage crystallization of matrix minerals at both syn- and post-eruptive conditions. The chemical correspondence between a certain zoned mineral and the hosting melt (i.e., bulk rock composition) is important to correctly model the intensive and extensive variables of the plumbing system (Putirka, 2008). Because of the absence of residual glass, we have verified the attainment of (near-)equilibrium between crystal and bulk rock analyses using different equilibrium models for olivine, clinopyroxene, plagioclase, and titanomagnetite. These models were integrated with thermometers, barometers, hygrometers, and oxygen barometers from the literature, in order to minimize any potential uncertainty in P-T-H_2O-fO_2 estimates and to track the crystallization conditions of the bulk system (i.e., crystal + melt). A detailed description of this approach is reported in the SM7.

6.1.1. Olivine thermometry

$Fo_{59\text{-}72}$ olivines are in equilibrium with magma compositions of $Mg\#_{26\text{-}37}$ for VL194/1, VL230/7, VL144/2, and VL175C/3, over buffering conditions relative to ΔQFM (quartz-fayalite-magnetite) between +1.2 and +2.2 (SM7). In the thermal range of 1036-1110 °C, the crystallization temperature progressively increases with increasing Fo in olivine. These

estimates correlate well with the homogenization temperatures (T_{hom}) of melt inclusions in olivine phenocrysts (Fo_{56-82}) reported in Gioncada et al. (1998) and calculated for shoshonites (1040-1190 °C) and latites-trachytes (1040-1090 °C) representative of the eruptive activity of Vulcano Island in the past 50 ka. Fo_{87-91} olivines in the most primitive VL168/12 from La Sommata Formation are found to be in equilibrium with melt inclusion compositions ($Mg\#_{66}$) previously published for the same eruption (see Table 3a in Gioncada et al., 1998). The estimated crystallization temperatures are in the range of 1186-1207 °C (Fig. 2) and are comparable to T_{hom} = 1190-1250 °C calculated for Fo_{87-91} olivines (Gioncada et al., 1998). The much higher temperature range calculated for VL168/12 is also consistent with major and trace element analyses of olivine-hosted melt inclusions, suggesting that La Sommata magma is nearly in equilibrium at mantle depths (Gioncada et al., 1998) via partial melting of a depleted peridotitic source veined by metasomatic, clinopyroxene-rich regions (Kamenetsky and Clocchiatti, 1996). Vulcano Island is emplaced on several kilometers thick metamorphic basement belonging to the Calabrian arc and consisting of metapelitic, granulitic (upper crust) and mafic granulitic (lower crust) successions (De Astis et al., 2013 and references therein). The Moho depth has been estimated at ~21-25 km (Peccerillo et al., 2006 and references therein) and, rationally, mantle-derived olivine phenocrysts from VL168/12 (Gioncada et al., 1998) may have equilibrated at P = 620-740 MPa, presuming a continental crust density of 2.7 g/cm^3.

6.1.2. Clinopyroxene thermobarometry and hygrometry

Fig. 3 shows the Gaussian distribution plots resulting from probability density functions calculated at (near-)equilibrium condition for each P, T, and H_2O variable (SM7). As the composition of magma evolves from basalt ($Mg\#_{92}$) to rhyolite ($Mg\#_{71}$), the crystallization of clinopyroxene takes place at decreasing P and T conditions, as well as the amount of H_2O in

equilibrium with clinopyroxene decreases. Basaltic samples (VL168/2, VL194/1, and VL168/12) are characterized by probability peaks for *P*, *T*, and melt-H_2O contents, in the ranges of ~550-750 MPa, ~1190-1220 °C, and ~1.6-2.0 wt.% H_2O, respectively (Fig. 3). A P_{max} of 825±80 MPa (~28 km of depth) has been estimated by Bullock et al. (2019) for glomerocrysts-hosted clinopyroxenes in mafic cumulates from the Pietre Cotte lava flow (1739 CE) extruded on the northern slope of the active La Fossa cone. Petrological and geophysical data retrieved on historic products from La Fossa cone and Vulcanello support the idea of a unique deep level of basaltic magma storage at 620-740 MPa (~18.5-21 km of depth; cf. Zanon et al., 2003), corresponding to the Moho depth (Gioncada et al., 1998; Zanon et al., 2003; De Ritis et al., 2013). For the most recent Pietre Cotte lava flow, consisting of multiple mingling events of compositionally distinct magmas, *P* and *T* conditions of 707±80 MPa (above the Moho) and 1089-1149 °C, respectively, have been derived for the shoshonitic-latitic components (Bullock et al., 2019). On the other hand, probability peaks for the much older (from 27.9±6.6 to 8.3±1.6 ka) shoshonitic (VL230/7 and VL180), latitic (VL175B/1, VL144/2, and VL213B/2) and trachytic (VL183/10 and VL175C/3) samples from Eruptive Epochs 6, 7, and 8 indicate clinopyroxene saturation at intermediate crystallization conditions of ~100-450 MPa, ~1100-1180 °C, and ~0.5-1.6 wt.% H_2O (Fig. 3). A zoned shoshonitic-latitic reservoir is located between 12.5 and 16.8 km of depth during the last 1000 years of activity (De Astis et al., 2013). Nicotra et al. (2018) suggested mingling with latitic and trachytic magmas at 3.6-5.5 km depth under La Fossa cone. Rhyolites (VL181 and VL182/1) samples reflect shallower, colder and more degassed magmatic environments, with probability distributions bounded at ~50 MPa, ~1100 °C, and ~0.7 wt.% H_2O (Fig. 3). The concurrent decrease of *P* and H_2O observed in this study is consistent with basaltic melt inclusion data from Clocchiatti et al. (1994) and Gioncada et al. (1998), documenting maximum H_2O contents of 1.8-3.8 wt.% in equilibrium with primitive Fo_{88-91} olivine phenocrysts. The same authors highlight that, in the

pre-15 ka period of volcanic activity, the magmatic reservoirs underwent an open-system differentiation with loss of the volatile species (H_2O, Cl and S) at shallow crustal levels. This period of activity is related to a collapse phase which occurred in the northern sector of Vulcano Island and the consequent ascent of more degassed (0.3-1.9 wt.% H_2O) magmas feeding the explosive (shoshonitic scoriae) and effusive (shoshonitic/latitic lavas) eruptions of Monte Saraceno (VL180, VL213B/2 and VL209A/2 dated at ~8.3 ka; De Astis et al., 1989), as well as the rhyolitic domes of the Carabinieri Formation (VL181 dated at ~8.5 ka; Soligo et al. 2000). Notably, the differentiation of magmas from Eruptive Epochs 6, 7, and 8 is accompanied by a decreasing crystallization temperature (from 1180 to 1100 °C), in close agreement with that reconstructed by Gioncada et al. (1998) for the pre-15 ka period (from 1180±20 to 1080±10 °C). Conversely, clinopyroxene-based thermobarometric estimates conducted on the historic Pietre Cotte lava flow, illustrate a different scenario in which the trachytic mineral assemblage yields deep clinopyroxene crystallization conditions of ~640±74 MPa and 1000-1130 °C (Bullock et al., 2019). Over the most recent volcanic history of La Fossa and Vulcanello, shallower shoshonitic and latitic reservoirs have been also identified by De Astis et al. (2013) at ~350-470 MPa and further corroborated by thermodynamic calculations of Nicotra et al. (2018) on the stability field of An_{62-68} plagioclase phenocrysts. The geochemical signature of these reservoirs has been envisaged by Mandarano et al. (2016) as the main source of intense fumarolic emissions from the summit of La Fossa cone, together with additional fumarolic fluids originated by shallower degassing of latitic and trachytic magmas potentially stored at 100-160 MPa (Zanon et al., 2003; Vetere et al., 2015; Nicotra et al., 2018). This pressure range conforms to probability distributions retrieved for latitic (VL213B/2) and trachytic (VL175C/3 and VL183/10) magmas from Eruptive Epochs 6, 7, and 8 (Fig. 3). Probability peaks corresponding to P_{min} of ~50 MPa are also observed for rhyolitic (VL181 and VL182/1) products of Eruptive Epochs 6 and 8, in parallel with the knowledge of small volume rhyolitic

reservoirs (e.g., Commenda, Pietre Cotte, and 1888–90 CE magmas) stored at *P* of 30-60 MPa and *T* of 940-965 °C (Clocchiatti et al., 1998; Paonita et al., 2013; Nicotra et al., 2018; Bullock et al., 2019). Overall, barometric (Zanon et al., 2003; Frezzotti et al., 2004) and petrological data (De Astis et al., 1997a) constrain the shallower magma ponding system to depths of 3-4 km.

6.1.3. Plagioclase thermometry and hygrometry

The melt-H_2O content progressively increases from ~0.5 to ~4.2 wt.% with increasing magma differentiation and the progressive decrease of the temperature (~860-1100 °C) at which the melt is saturated with plagioclase (SM7). Basaltic (VL168/12) and shoshonitic (VL230/7 and VL180) samples yield H_2O contents (~0.5-2.5 wt.%) in equilibrium with plagioclase (Fig. 4). Conversely, for intermediate (VL175B/1 and VL144/2) and evolved (VL183/10, VL181, VL182/1, and VL17811A) samples, the amount of H_2O in equilibrium with plagioclase (~1.0-4.2 wt.% H_2O; Fig. 4) is markedly higher than that estimated either for clinopyroxene-saturated magmas (~0.8-1.7 wt.% H_2O; Fig. 3) or for melt inclusions in mafic minerals from compositionally similar historic products (0.3-1.9 wt.% H_2O; Clocchiatti et al., 1994; Gioncada et al., 1998). The different H_2O estimates obtained by comparing mafic and felsic minerals has been explained by previous studies focusing on the crystallization paths of alkaline magmas at Mt. Etna (Mollo et al., 2015) and Stromboli (Di Stefano et al., 2020). Regarding the early formation of olivine and clinopyroxene, the degree of crystallization may increase up to ~50% during titanomagnetite and plagioclase growth, as these mineral phases crystallize at the late stage of cooling and differentiation of alkaline magmas (cf. Vetere et al., 2015). Owing to the abundant segregation of anhydrous minerals, the original H_2O content recorded by early-formed mafic phenocrysts inevitably increases in the residual and more silicic melt (Mollo et al., 2015; Di Stefano et al., 2020). Cooling and decompression of magmas

during ascent towards the surface contribute also to expand the stability field of titanomagnetite and plagioclase (Mandarano et al., 2016). The combined effects of magma uprising and crystallization of anhydrous minerals leads to H_2O saturation in shallow magmatic reservoirs (i.e., second boiling and generation of volatile overpressure; Stock et al., 2016), with the consequent outgassing of great amounts of volatile components at Vulcano Island (Mandarano et al., 2016). The solubility model of Papale et al. (2006) confirms that, at shallow conditions of 50-100 MPa, the maximum amount of H_2O dissolved in more evolved trachytic and rhyolitic magmas is ~2.5-4.0 wt.%. The value of $^{plg-melt}Kd_{Ca-Na}$ is also a good proxy for the concentration of H_2O in the melt phase (Sisson and Grove, 1993; Ushioda et al., 2014; Scarlato et al., 2017) and trachytic-rhyolitic products show Ca-Na exchange of ~2.0-4.0 (SM7), which correspond to melt-H_2O contents of ~2.0-5.0 wt.% (cf. Sisson and Grove, 1993). Through the iterative solution of plagioclase- and clinopyroxene-based hygrometers and thermobarometers, Costa et al. (2020) have calculated similar H_2O concentrations (~2.0-3.5 wt.%) for silicic magmas erupted at La Fossa cone in the last 1000 years. Dissolved hydroxyl groups preferentially bond with Na rather than Ca, thus lowering the activity of Na_2O relative to CaO in the melt (Crabtree and Lange, 2011) and favoring the growth of a more calcic plagioclase with increasing H_2O in the melt phase (Masotta and Mollo, 2019). However, as SiO_2 and Na_2O+K_2O increase in more differentiated and crystal-rich magmas, the composition of plagioclase becomes more sodic (Blundy and Wood, 1991) and the solubility of H_2O systematically increases from basalt to rhyolite (Papale et al., 2006). For H_2O-rich silicic magmas, the hypothetical Ab-An binary diagram is characterized by a plagioclase loop at low temperature because of the high volatile content (Kuritani, 1999). The convex upward liquidus curve is also shifted towards very low temperatures due to the silicic bulk composition of the system and the incipient titanomagnetite and plagioclase saturation. For example, phase equilibrium experiments conducted on rhyolitic compositions by Waters et al. (2015) show that An_{50} plagioclases saturate the melt at 100 MPa,

850 °C and melt-H_2O content of ~4.0 wt.%, as calculated for several phenocryst populations from rhyolitic samples VL181, VL182/1, and VL17811A (Fig. 4). In this scenario, the growth of more sodic (An_{30-62}) plagioclases in trachytes and rhyolites at Vulcano Island can be attributed to a late stage crystallization process accompanied by H_2O concentration in excess of 2.5-4.0 wt.% at 50-100 MPa (Papale et al. 2006). For similar rhyolites erupted at Lipari between 22 and 42 ka, Gioncada et al. (2003) estimated a H_2O saturation of ~4.6 wt.% at ~150 MPa. Additionally, the degree of undercooling is expected to be very high when H_2O exsolves (Kuritani, 1999) and a rapid gas loss leads to a kinetic delay in crystallization followed by a high plagioclase nucleation rate. These cooling conditions typically produce abundant groundmass crystallization, together with a drop in An content of newly formed plagioclase microlites (Hammer and Rutherford, 2002). According to Guilbaud et al. (2007), core-to-rim compositional gradients in plagioclase phenocrysts and the formation An-poor microlites at Vulcano Island indicate that the crystal growth continued during degassing and progressive H_2O exsolution (see the thermodynamic simulations discussed below).

6.1.4. Spinel thermometry and oxygen barometry

In general, trachytic and rhyolitic products depict a thermal path (~900-950 °C) lower than that (up to ~1080 °C) measured for more primitive compositions. Under such circumstances, titanomagnetite (Usp_{11-29}) equilibrates with progressively more evolved and oxidized melts, with fO_2 between ΔQFM+1.5 and ΔQFM+3 (Fig. 5). Notably, when magmas approach to H_2O saturation at shallower depths (Fig. 4), the value of fO_2 increases with increasing H_2O in excess, as observed in several experimental studies (e.g., Moore et al., 1995). For different alkaline volcanic systems in Italy (Mollo et al., 2015), the oxygen fugacity has been showed to increase by 1 to 2 log units by H_2O exsolution and degassing. The state of the magmatic system changes from H_2O-undersaturated to H_2O-saturated regimes, thus controlling

the compositional evolution of magma and the incorporation of cations sensitive to melt-redox conditions (i.e., Fe^{3+}-Ti^{4+} exchange) in titanomagnetite (SM7). To better constrain such variation, the experimental calibration of Fe_2O_3/FeO in the melt proposed by Kress and Carmichael (1991) has been applied to bulk rock compositions over a *T* interval varying from 1100 to 1250 °C, as derived by olivine- and clinopyroxene-based thermometry. Resulting fO_2 values increase from ΔQFM+1.2 to ΔQFM+2.7, in agreement with those measured using titanomagnetite and confirming that the oxidation state of the system effectively increases as a function of magma differentiation.

6.2. Thermodynamic constraints on the liquid line of descent

The rhyolite-MELTS code (v.1.2.0; Gualda et al., 2012) has been employed to perform thermodynamic simulations based on the detection of phase saturation and energy convergence by Gibbs free energy minimization. The rhyolite-MELTS runs started at $T_{liquidus}$ > 1160 °C and continued along a crystallization path terminated at $T \approx 900$ °C. In order to guarantee a stable phase assemblage consistent with that observed in the natural products, the fractional crystallization process was simulated at 100, 300, and 600 MPa, initial melt-H_2O contents of 2 and 4 wt.%, and initial buffering conditions of ΔQFM+1.5 (SM8). As starting parental compositions, we selected two of the most primitive basaltic lavas from La Sommata Formation (cf. De Astis et al., 2013), showing either SHO (49.49 wt.% SiO_2 and 8.62 wt.% MgO) or HKCA (51.80 wt.% SiO_2 and 7.89 wt.% MgO) affinities (SM6). Therefore, each thermodynamic simulation was replicated for two distinct parental magmas, according to the following geochemical considerations: 1) the modeling of changes in trace elements and radiogenic isotope ratios fails to reproduce the transition from HKCA to SHO and KS magmatism by simple crustal processes (De Astis et al., 2000; Frezzotti et al., 2004), 2) a general agreement exists on the hypothesis that mafic rocks, with different degrees of

enrichment in incompatible trace elements and potassium, represent distinct magma types generated from heterogeneous mantle sources (Ellam and Harmon, 1990; Gioncada et al., 1998, 2003; De Astis et al., 2000, 2013), and 3) mafic products are the expression of geochemically distinct primary melts originated by both MORB- and OIB-type mantle sources which undergo variable degrees of metasomatism by subducted sediments (Pinarelli et al., 2019).

Fig. 6 shows the stability and proportion of minerals obtained by the best case set of rhyolite-MELTS runs (see the SM8 for the whole data set). For the SHO series, olivine (Fo_{70-83}) is the first phase on the liquidus at 100 MPa and its crystallization increases with increasing H_2O dissolved in the melt phase (Fig. 6). In contrast, clinopyroxene is the liquidus phase at 600 MPa in close correspondence with thermobarometric probability density curves yielding early crystallization at ~1190-1230 °C and ~500-800 MPa. Additionally, the thermodynamically-derived composition ($Mg\#_{73-82}$) of clinopyroxene approximates to that observed for phenocrysts from natural rock samples. Notably, natural Fo_{87-91} olivines found in the most primitive VL168/12 from La Sommata Formation are never obtained by thermodynamic simulations, in agreement with a mantle-derived origin as suggested by Gioncada et al. (1998). The segregation of spinel (i.e., titanomagnetite with Usp_{10-24}) and plagioclase (An_{52-83}) is low, due to the late crystallization of plagioclase at 900 °C and crystal content >50% (Fig. 6). For the HKCA series, the modeled mineral compositions do not substantially change with respect to those derived for the SHO composition, but olivine appears as the liquidus phase at both 100 MPa and 600 MPa with initial H_2O content of 4 wt.% (Fig. 6). As the amount of H_2O increases from 2 to 4 wt.%, the effect of pressure is inhibited and the stability field of olivine expands at the expense of clinopyroxene (Metrich and Rutherford, 1998). The saturation of plagioclase from the HKCA magma is more favored at 100 MPa and 1000-1050 °C (Fig. 6), but its degree of crystallization remains much lower than that observed for the natural modal content. This finding suggests that most of the plagioclase growth is driven by a dynamic crystallization

regime related to abundant H_2O exsolution and degassing (cf. Mandarano et al., 2016), rather than simple equilibrium crystallization under closed-system conditions. The crystallization path and composition of clinopyroxene from rhyolite-MELTS runs conducted at 100 MPa (1080-1150 °C) and 600 MPa (1140-1220 °C) are comparable to those obtained by thermobarometric calculations based on natural phenocrysts (Fig. 3). Such a good convergence reinforces the plumbing system constraints found for the pre-8 ka magmas, especially if we consider that rhyolite-MELTS and thermobarometers rely on very different parameterization procedures, accounting for free energy change reactions solved by thermochemical data and multiple linear regression analysis of experimentally-derived compositions, respectively.

The liquid lines of descent modeled by rhyolite-MELTS simulations track the differentiation path for both SHO and HKCA parental compositions (Fig. 7). For the sake of completeness, these thermodynamically-derived data are also compared with the overall natural compositional variability of natural products plotted in the TAS diagram, as well as in the SiO_2 v s. CaO and MgO diagrams. The modeled liquids resemble the differentiation paths of both SHO and HKCA magmas, evolving from basalts to latites to relatively undifferentiated trachytes (Fig. 7). Following the evolutionary trajectories, we observe that 1) SiO_2 and $Na_2O + K_2O$ increase up to ~61 (SHO) and ~64 (HKCA) wt.% and ~10 (SHO) and ~9 (HKCA) wt.%, respectively, whereas 2) CaO and MgO decrease down to ~5 (SHO) and ~3 (HKCA) wt.% and ~1.5 (SHO) and ~1.2 (HKCA) wt.%, respectively. As *P* increases from 100 to 600 MPa or melt-H_2O content decreases from 4 to 2 wt.%, the stability field of clinopyroxene increases, thus favoring to alkali enrichments and CaO + MgO depletions with respect to SiO_2 (Fig. 7).

It is worth stressing that Rhyolite-MELTS simulations fail to reproduce trachytic and rhyolitic residual melt compositions with SiO_2 >64 wt.%, corresponding to a threshold of 50% of solid fractionated. For this reason, we have performed least-square balance calculations starting from the most differentiated SHO (~61 wt.% SiO_2, ~10 wt.% $Na_2O + K_2O$, ~5 wt.%

CaO, and ~1.5 wt.% MgO) and HKCA (~64 wt.% SiO_2, ~9 wt.% $Na_2O + K_2O$, ~3 wt.% CaO, and ~1.2 wt.% MgO) trachytic compositions attained by MELTS thermodynamic simulations (SM8). The fractionated solid assemblage consists of the average analyses of clinopyroxene, feldspar (plagioclase + sanidine) and titanomagnetite. Results from calculations yield reliable residual sum of squares (Σr^2 = 0.02-0.32), accounting for the dominant fractionation of feldspar (7-23%) relative to clinopyroxene (1-6%) and titanomagnetite (1-5%) (see the SM9 for further details). Four representative residual melts modeled for either shoshonitic (SHO1-4) or high-K calc-alkaline (HKCA1-4) affinities are plotted in Fig. 7. These melts reproduce very well the most silicic differentiation of trachytic and rhyolitic magmas, as the degree of feldspar fractionation increases. Considering that the differentiation of basalts to trachytes takes place at crystal content of 50-55% (Fig. 7), the formation of rhyolitic melts requires a magmatic system with total crystallinity of 59-84%, in which the main paragenetic sequence shifts from olivine + clinopyroxene for basaltic-latitic magmas to feldspar for more silicic compositions (Fig. 6). Models of interstitial melt extraction based on compaction and hindered settling equations applied to highly crystalline magma reservoirs (i.e., crystal mushes) suggest that the most favorable window for crystal-melt separation occurs at a crystallinity of ~50-70% (Dufek and Bachmann, 2010). This process is likely to proceed throughout the compositional spectrum from basalt to rhyolite, when mantle-derived magmas differentiate within the crust to form crystal mushes (Dufek and Bachmann, 2010). According to Bachmann and Bergantz (2004), more evolved melts can be produced by a process of melt extraction from homogeneous silicic mushes when a connected crystal framework develops. The authors found also that, at crystallinity >70%, crystal-liquid separation is primarily caused by low melt fraction compaction, despite a reduced permeability of the system that may inhibit the extraction of melt. As an alternative to compaction, the upward extraction of interstitial melts formed in the mush region can be explained by the failure and detachment of the growing crystal network at

the roof of the solidification front (Marsh, 2002; Masotta et al., 2016; Di Stefano et al., 2020). The interstitial liquid phase extracted is chemically very similar to crystal-poor silicic magmas (Cashman and Blundy, 2000), making the crystal mush a natural source and storage region for high-SiO_2 melts in the upper crust (Bachmann and Bergantz, 2004). The development of a crystal-rich region may also account for the compositional gap observed at SiO_2 contents between ~65 and ~66 wt.%, corresponding to the transition between more evolved trachytes and rhyolites (see the TAS diagrams in Fig. 7 and SM6). Magmatic compositional gaps can be generated by melt-crystal dynamics responsible for the formation of a solidification front at the top of the magmatic reservoir and further extraction of silicic melts (Marsh, 2000; Bachmann and Bergantz, 2004; Dufek and Bachmann, 2010; Masotta et al., 2016). Consistently with results from our least-square mass balance calculations, Costa et al. (2020) have recently observed that the role of shallow crystal mushes is important at Vulcano Island for the production of small volumes of silicic magmas through repeated episodes of melt extraction. By integrating thermobarometric calculations and temperature gradient experiments, these authors found that both trachytic and rhyolitic compositions at Vulcano Island can be effectively derived through differentiation of a common latitic magma by varying the proportions of the mineral assemblage within the mush region.

6.3. Major and trace element modeling

Open-system contamination phenomena have been widely documented at Vulcano Island during interaction between more or less evolved magmas and metamorphic rocks belonging to the Calabro-Peloritano basement (Clocchiatti et al., 1994; De Astis et al., 1997a; Gioncada et al., 1998; Del Moro et al., 1998; Frezzotti et al., 2004). This latter consists of a 18-25 km thick continental crust whose structure can be inferred from deep seismic sounding data (Peccerillo et al., 2006): 1) a uppermost crustal layer and representative of the sedimentary and

volcanic cover (depth of ~2 km and Vp of 3.2 km/s), 2) the Calabrian Arc metapelites (depth of ~2-5 km and Vp of 5.2 km/s), 3) an upper crust of granitoids or felsic granulites (depth of 5-15 km and ~Vp of 5.5-6.0 km/s), and 4) a lower crust of mafic granulites (depth of ~15-25 km and Vp of 6.6 km/s). Mafic magmas erupted during the early activity of Vulcano Island are characterized by variable enrichments in incompatible trace elements (i.e., Nb, Zr, Rb, Ta, and Yb; De Astis et al., 1997a; Del Moro et al., 1998) and isotopic signatures (i.e., $^{87}Sr/^{86}Sr$, $^{143}Nd/^{144}Nd$, and $^{207}Pb/^{204}Pb$; De Astis et al., 1997a, 2000, 2003; Del Moro et al., 1998) indicative of significant wall-rock assimilation. At the early stage of magmatic evolution, continuous arrival of magmas from mantle depths inhibited the geochemical differentiation of the original plumbing system towards more evolved compositions. In contrast, younger magmas from Eruptive Epoch 8 were dominated by abundant fractional crystallization of felsic minerals with minor crustal assimilation, thus generating trachytic and rhyolitic products with variable isotopic signatures (De Astis et al., 1997a, 2003; Peccerillo et al., 2006; Bullock et al., 2019). Rhyolites display a higher $^{87}Sr/^{86}Sr$, a lower $^{143}Nd/^{144}Nd$ and a slightly lower $^{206}Pb/^{204}Pb$ than the latites, denoting a fractional crystallization process plus low degrees of crustal assimilation (De Astis et al., 2000; Gioncada et al., 2003).

In this context, we have modeled the geochemical behavior of some selected major (TiO_2 and K_2O) and trace (Nb, Zr, and Sr) elements that were most frequently analyzed by previous authors and reported in literature for either magmatic or crustal materials. Fractional crystallization (FC), and assimilation and fractional crystallization (AFC) processes have been simulated using the equations and input parameters reported in the SM10. Starting from the Eruptive Epoch 6, mixing phenomena between mafic and felsic end-members have been documented at Vulcano Island, especially to interpret the origin of trachytic magmas by injection of latitic melts into rhyolitic reservoirs (Clocchiatti et al. 1994; De Astis et al. 1997a; Gioncada et al., 1998, 2003; Del Moro et al., 1998) or the genetic relationship between latitic-

to-rhyolitic enclaves and their host rhyolitic magmas (Frezzotti et al., 2004; Perugini et al., 2007; Piochi et al., 2009; Forni et al., 2015; Vetere et al., 2015; Bullock et al., 2019; Rossi et al., 2019). One important outcome from previous studies is that rectilinear trends from binary mixing modeling do not capture in full the variation of trace elements for several natural bulk rocks (see for example Fig. 8 in De Astis et al., 1997a). Furthermore, Rb, Sr, and Ni inventory in silicic products from Eruptive Epochs 6 and 7 depict hyperbolic trajectories that preclude a pure binary mixing process. The petrogenesis of rhyolitic products with a pronounced negative Eu anomaly (Eu/Eu* = 0.1-0.2) has been recently attributed to feldspar-liquid separation processes in a plagioclase-dominated mush located at shallow depths (Nicotra et al., 2018). The formation of crystal-poor rhyolites is also better explained by segregation of the interstitial melt from latitic-trachytic crystal mushes, possibly favored by the second boiling of the melt and consequent exsolution of a fluid phase (Costa et al., 2020). In an attempt to model these conditions, the in-situ crystallization (ISC) equation has been also employed in this study to reproduce the contribution of silica-rich residual melts trapped/extracted from the crystal mush (see the SM10 for further details). Bearing in mind that simple rhyolite-MELTS thermodynamic simulations fail to reproduce the more silicic trachytic and rhyolitic products from Eruptive Epochs 6, 7, and 8 (SiO_2 > 64 wt.% and $Na_2O + K_2O$ > 10 wt.%; Fig. 7), the ISC trajectory is modeled starting from a putative poorly differentiated trachytic composition with ~0.6 wt.% TiO_2, ~7 wt.% K_2O, ~18 ppm Nb, ~150 ppm Zr, and ~ 900 ppm Sr.

Results from the application of FC-AFC and ISC equations are presented for simplicity by bi-plot Nd vs. K_2O (Fig. 8a), Zr (Fig. 8b), TiO_2 (Fig. 8c) and Sr (Fig. 8d) diagrams. Most of the primitive (VL168/2, VL194/1, VL168/12, VL230/7, VL209A/2 and VL180), intermediate (VL175B/1, VL144/2, and VL213B/2) and evolved (VL229/6 and VL183/10) bulk rock compositions are constrained by FC-AFC trajectories, in which *F* is always kept below the threshold value of 0.5, comparable to previous MELTS calculations (Fig. 6). Such a melt

fraction makes more reliable the differentiation path of magma, thus preventing crystal-melt separation effects typical of mush systems and documented at a crystallinity between ~50% and 70% (Dufek and Bachmann, 2010). The FC-AFC trajectories depict an increase of major (TiO_2 and K_2O) and trace (Nb, Zr, and Sr) element concentrations, as the result of prevalent fractionation of olivine + clinopyroxene phenocrysts from basaltic (VL168/2, VL194/1, and VL168/12) to shoshonitic (VL230/7, VL209A/2, and VL180) to poorly evolved latitic (VL175B/1, VL144/2, and VL213B/2) magmas. The degrees of crustal assimilation (r = 0.2-0.4) are consistent with previous AFC models reported in literature (De Astis et al., 1997a; Gioncada et al., 2003; Bullock et al., 2019). Under these open-system conditions, most of the trace element systematics referring to Eruptive Epochs 6 (VL175B/1), 7 (VL144/2), and 8 (VL180, VL213B/2, and VL209A/2) are faithfully reproduced. However, the assimilation of crustal material is also accompanied by significant inputs of hot, mafic, and water-rich magmas from depth that inhibit abundant feldspar fractionation over time (De Astis et al., 1997a, 2013). Therefore, the evolutionary process of older products (VL194/1, VL168/2, and VL168/12) is effectively explained by AFC in a deep, continuously refilled and tapped magma chamber (i.e., RAFC process as originally proposed by De Astis et al., 1997a). On the other hand, at the beginning of Eruptive Epoch 6, there is an abrupt compositional shift of the magma towards highly differentiated trachytes (VL175C/3) and rhyolites (VL182/1) (De Astis et al., 2013). These magmas are generally associated with minor mafic-intermediate eruptions due to the activation of new vents in the northern and north-western sectors. In this scenario, the ISC trajectory may shift downward (or upward) with increasing (or decreasing) f, thus capturing very well both major and trace element inventory of the most silicic products from Eruptive Epochs 6, 7, and 8, with particular regard to the compositions of rhyolites (Fig. 8). Melt-crystal dynamics play an important role during the magmatic evolution, particularly for the abrupt decrease of TiO_2 (Fig. 8c) and Sr (Fig. 8d) concentrations, as these cations are more easily

incorporated in a felsic (feldspar + oxide) paragenesis. Most of the evolutionary path is controlled by incipient late-stage plagioclase crystallization (De Astis et al., 2013; Nicotra et al., 2018), corroborated by the strong Eu anomaly of highly differentiated trachytes and rhyolites (Eu/Eu* = 0.21-0.29) and the Ca-Na exchange between plagioclase and melt (SM7). The ISC trajectory is also supported by the increasing concentration of incompatible trace elements (Nb vs. Zr; Fig. 8b), as the proportion of interstitial melt migrating from the solidification front increases from 20% to 60% (i.e., f = 0.2-0.6; Fig. 8b). This compositional change pairs with the substantial enrichments in Rb, Nb, Th, U, and Ta of all the rhyolitic samples from Eruptive Epoch 8, resembling the compositions of silicic magmas extracted from a shallow crustal mush and/or distinct magma-mush pockets within the volcanic plumbing system (Dufek and Bachmann, 2010). Furthermore, De Astis et al. (2013) have documented a weak variation of $^{87}Sr/^{86}Sr$ for silicic products from Eruptive Epoch 6, denoting very low degrees of interaction with the continental crust. The increase in the proportions of silicic vs. mafic magmas over time has been attributed to an overall migration of the magmatic reservoirs towards shallow levels (De Astis et al. 1997a; Zanon et al. 2003; Frezzotti and Peccerillo 2004), as attested by the decrease of clinopyroxene saturation pressure (from ~600-800 to ~50 MPa; Fig. 3) and the change of magma redox state from ΔQFM+1.5 to ΔQFM+3 (Fig. 5) for more differentiated bulk systems. In this context, the interplay between magma differentiation and crystal-melt separation may be an effective mechanism to control the eruption dynamics of rhyolites. As for the younger products outpoured at La Fossa caldera, the development of shallow crystal mushes starting from Eruptive Epoch 6 is important for the production of silicic magmas by repeated episodes of melt extraction (Costa et al., 2020). The inability to reproduce natural bulk rock compositions by FC-AFC equations (Fig. 8) and results from temperature gradient experiments presented by Costa et al. (2020) lead to the conclusion that open-system phenomena at Vulcano Island are intimately related to mush dynamics, in which silicic

interstitial melts are produced by ISC processes (Fig. 8). We also do not exclude that silicic melts can be extracted from a crystal-rich region and subsequently mixed with the free magmas hosted in interconnected shallow reservoirs (cf. Bachmann and Bergantz, 2004; Dufek and Bachmann, 2010; Cashman and Blundy, 2003), thereby providing local evidences of magma mixing (De Astis et al., 1997a, 2013).

6.4. Sub-volcanic plumbing system architecture

Several studies have provided inferences on the configuration of different magma storage zones beneath Vulcano Island on the basis of petrological, geochemical, fluid inclusion, and geophysical constraints (e.g., Zanon et al., 2003; De Astis et al., 2013; Nicotra et al., 2018; Bullock et al., 2019; Costa et al., 2020). Here, we put forward an integrated model for the magma plumbing system architecture at Vulcano island for the period 54-8 ka (Fig. 9). Through interpolation of thermobarometric and hygrometric data with thermodynamic modeling results, we provide evidence that the deepest level of basaltic magma storage (VL168/2, VL194/1, and VL168/12 from La Sommata Formation) is located at depth ≥19 km (and close to the Moho transition zone; Peccerillo et al., 2006 and references therein), where more primitive magmas crystallize a mafic assemblage at relative high-T (~1190-1250 °C), low-fO_2 (ΔQFM+1.5) and H_2O undersaturated (~1.6-2.0 wt.%) conditions (Fig. 9). Coherently, Nicotra et al. (2018) and Bullock et al. (2019) support the idea of a unique deep level of magma storage for La Fossa and Vulcanello during the last 1000 years of activity, located between 18.5 and 21 km of depth, where a basaltic magma is present (Zanon et al., 2003). The basaltic reservoirs proposed in the present work are dominated by crystallization of prevalent olivine + clinopyroxene phenocrysts. At the early stage of magmatic evolution, some of these magmas can reach the surface directly (e.g., La Sommata Formation), while other magmas can evolve stalling at intermediate to shallower levels. The deeper to shallower crystallization path of basaltic

magmas is related to the tectonic control exerted by regional fault systems in the area, a feature widely invoked in literature (cf. Ruch et al., 2016). In the crust below Vulcano Island, there is a wide multi-level storage between 5.5 and 16 km (i.e., ~100-450 MPa and ~1100-1180 °C), related to magmatic reservoirs with shoshonitic-latitic-trachytic compositions (Fig. 9). Regarding to the most recent shoshonites and latites from this study, the volcanological and petrological features of rock samples from Monte Saraceno Formation (VL209A/2, VL180, and VL213B/2) document the complex interplay between the previous, repeated episodes of volcano-tectonic collapse (the last of which involving the western sector of La Fossa caldera) and volcanism rejuvenation. Strombolian products and lavas of Monte Saraceno were emitted along the edge of La Fossa caldera, due to the formation of fractures and dykes bypassing the central portion of the caldera structure. This pattern is similar to that observed for Vulcanello magmas in more recent years and related to the opening of vents along the caldera edge, outside the system of La Fossa cone. In both cases the system was fed by the ascent of less viscous shoshonitic magmas (De Astis et al., 2013). The differentiation proceeds by continuous fractional crystallization and crustal assimilation processes. Moreover, starting from the Eruptive Epoch 6, the abundant segregation of feldspar phenocrysts from latitic-trachytic magmas favored the development of crystal mushes. Comparatively to the most recent La Fossa feeding system, intermediate (12.5-16.8 km of depth) and shallow (3.6-5.5 km of depth) crustal storage regions have been proposed for shoshonitic-latitic and latitic-trachytic magmas, respectively (De Astis et al., 2013; Nicotra et al., 2018; Costa et al., 2020). Regarding to the 1739 CE Pietre Cotte lava flow, fractional crystallization of shoshonitic-latitic magma to a trachytic magma has been also suggested to occur at ~16-24 km of depth and ~1000-1130 °C (Bullock et al., 2019). On the other hand, thermobarometric, mass balance, and in-situ crystallization calculations from this study suggest that the uppermost rhyolitic magmas are located at depth of ~2 km (Fig. 9) and, likely, in association with highly differentiated trachytic

magmas (cf. Paonita et al., 2013). These silicic reservoirs are generated by the extraction of interstitial melts from mush zones dominated by feldspar and titanomagnetite saturation at ~860-1100 °C, more oxidized crystallization conditions (ΔQFM+3), and H_2O concentrations in excess of 2.5-4.0 wt.% (cf. Gioncada et al., 2003). In this context, the plumbing system model proposed for the older rhyolites from Eruptive Epoch 6 accounts for the remobilization of the crystal mush via multiple injections of hotter shoshonitic-latitic magmas from depth. Part of these magmas are erupted, and the remaining part interact with the mush system.

7. Concluding remarks

By investigating mineral and bulk rock compositional changes at Vulcano Island, we have provided new petrological constraints on the crystallization conditions (i.e., *P*-*T*-H_2O-fO_2) that have controlled the differentiation of both SHO and HKCA magmas erupted in the period 54-8 ka. The most important outcomes from this study can be summarized as follows:

1) mafic magmas are characterized by $T_{liquidus}$ > 1160 °C, in which olivine occurs as liquidus phase preferentially at low-*P* (≤300 MPa) and/or high melt-H_2O contents (> 2wt.%). Olivine phenocrysts saturate the melt at progressively lower *T*, as the composition of the system changes from shoshonite (1040-1190 °C) to latite-trachyte (1040-1090 °C);
2) the crystallization of clinopyroxene delineates very well the presence of polybaric-polythermal magmatic reservoirs within the plumbing system. Probability density functions show that primitive basaltic magmas equilibrate with clinopyroxene at high *P* (~550-750 MPa) and *T* (~1190-1220 °C) conditions. The *P*-*T* array changes significantly as the magma migrates towards shallower and colder storage regions characterized by either shoshonitic-latitic-trachytic (~100-450 MPa and ~1100-1180

°C) compositions or highly differentiated trachytic-rhyolitic (≤50 MPa and ≤1100 °C) compositions;

3) the saturation of clinopyroxene takes place at the early stage of magma differentiation and relative low melt-H_2O contents (0.5-2.0 wt.%), whereas plagioclase crystallizes from residual, more evolved, colder (~860-1100 °C), and H_2O-rich (~1.0-4.2 wt.%) melts. The combined effects of magma uprising and the late stage crystallization of anhydrous minerals lead to H_2O saturation in shallower magmatic reservoirs. Cooling, decompression, and degassing phenomena also enhance the stability field of titanomagnetite and plagioclase. As the amount of H_2O increases towards the saturation state of the melt, the Fe-Ti exchange in titanomagnetite tracks the formation of more oxidized (up to ΔQFM+3) magmas;
4) the liquid line of descent of both SHO and HKCA magmas can be modeled by thermodynamic simulations, starting from a putative parental basalt and terminating to a less differentiated trachyte. Silicic magmas with openly trachytic and rhyolitic compositions are derived only through mass balance calculations, in which the fractionation of plagioclase dominates over that of clinopyroxene. At this advanced stage of evolution, the total crystallinity (59-84%) of the system matches with that required for the extraction of interstitial melts from silicic mush regions;
5) FC and AFC processes based on major and trace element concentrations reproduce the majority of magmas erupted at Vulcano Island, in which crustal contamination accounts for the contribution of metamorphic rocks from the Calabro-Peloritano basement. On the other hand, enrichments (K, Rb, and Zr) and depletions (Eu, Sr, and Ti) in incompatible trace elements typical of highly differentiated trachytic and rhyolitic eruptions are better modeled by in-situ crystallization processes, due to upward migration of buoyant interstitial melts from a crystal mush;

6) the architecture of the plumbing system is characterized by multiple reservoirs in which compositionally distinct magmas pond and undergo polybaric-polythermal differentiation, before erupting to the surface.

References

Bachmann, O., Bergantz, G. W., 2004. On the origin of crystal-poor rhyolites: extracted from batholithic crystal mushes. Journal of Petrology, 45(8), 1565-1582.

Blundy, J. D., Wood, B. J., 1991. Crystal-chemical controls on the partitioning of Sr and Ba between plagioclase feldspar, silicate melts, and hydrothermal solutions. Geochimica et Cosmochimica Acta, 55(1), 193-209.

Bullock, L. A., Gertisser, R., O'Driscoll, B., Harland, S., 2019. Magmatic evolution and textural development of the 1739 CE Pietre Cotte lava flow, Vulcano, Italy. J. Volcanol. Geoth. Res., 372, 1-23.

Cashman, K., Blundy, J., 2000. Degassing and crystallization of ascending andesite and dacite. Philosophical Transactions of the Royal Society of London. Series A: Mathematical, Physical and Engineering Sciences, 358(1770), 1487-1513.

Clocchiatti, R., Del Moro, A., Gioncada, A., Joron, J. L., Mosbah, M., Pinarelli, L., Sbrana, A., 1994. Assessment of a shallow magmatic system: the 1888-90 eruption, Vulcano Island, Italy. Bulletin of Volcanology, 56, 466-486.

Costa, S., Masotta, M., Gioncada, A., Pistolesi, M., Bosch, D., Scarlato, P., 2020. Magma evolution at La Fossa volcano (Vulcano Island, Italy) in the last 1000 years: evidence from eruptive products and temperature gradient experiments. Contributions to Mineralogy and Petrology, 175(4), 1-22.

Crabtree, S. M., Lange, R. A., 2011. Complex phenocryst textures and zoning patterns in andesites and dacites: Evidence of degassing-induced rapid crystallization. Journal of Petrology, 52(1), 3-38.

Davì, M., De Rosa, R., Donato, P., Vetere, F., Barca, D., Cavallo, A., 2009. Magmatic evolution and plumbing system of ring-fault volcanism: the Vulcanello peninsula (Aeolian Islands, Italy). European Journal of Mineralogy, 21, 1009-1028.

De Astis, G., Frazzetta, G., La Volpe, L., 1989. I depositi di riempimento della caldera del Piano ed i depositi della Lentia. Bollettino GNV (Gruppo Nazionale di Vulcanologia), 2, 763-778.

De Astis, G., 1995. Evoluzione Vulcanologica e Magmatologica dell'isola di Vulcano (Isole Eolie). PhD thesis, Università degli Studi di Bari.

De Astis, G., La Volpe, L., Peccerillo, A., Civetta, L., 1997a. Volcanological and petrological evolution of Vulcano Island (Aeolian Arc, southern Tyrrhenian Sea). Journal of Geophysical Research, 102, 8021-8050.

De Astis, G., Dellino, P., De Rosa, R., La Volpe, L., 1997b. Eruptive and emplacement mechanisms of widespread fine-grained pyroclastic deposits on Vulcano Island (Italy). Bulletin of Volcanology, 59, 87-102.

De Astis, G., Peccerillo, A., Kempton, P. D., La Volpe, L., Wu, T. W., 2000. Transition from calc-alkaline to potassium-rich magmatism in subduction environments: geochemical and Sr, Nd, Pb isotopic constraints from the island of Vulcano (Aeolian arc). Contributions to Mineralogy and Petrology, 139, 684-703.

De Astis, G., Ventura, G., Vilardo, G., 2003. Geodynamic significance of the Aeolian volcanism (Southern Tyrrhenian Sea, Italy) in light of structural, seismological, and geochemical data. Tectonics, 22, 1040-1057.

De Astis, G., Lucchi, F., Dellino, P., La Volpe, L., Tranne, C. A., Frezzotti, M. L., Peccerillo, A., 2013. Geology, volcanic history and petrology of Vulcano (central Aeolian archipelago). In: Lucchi, F., Peccerillo, A., Keller, J., Tranne, C.A., Rossi, P.L. (Eds.), The Aeolian Islands Volcanoes. Geological Society, London, Memoirs 37, 181-349.

De Rosa, R., Frazzetta, G., La Volpe, L., Mazzuoli, R., 1988. The Spiaggia Lunga scoriae deposits: an example of fissural type eruption at Vulcano, Aeolian Islands, Italy. Rendiconti della Societa` Italiana di Mineralogia e Petrologia, 43, 1059-1068.

De Ritis, R., Ravat, D., Ventura, G., Chiappini, M., 2013. Curie isotherm depth from aeromagnetic data constraining shallow heat source depths in the central Aeolian Ridge (Southern Tyrrhenian Sea, Italy). Bulletin of Volcanology, 75(4), 710.

Del Moro, A., Gioncada, A., Pinarelli, L., Sbrana, A., Joron, J. L., 1998. Sr, Nd, and Pb isotope evidence for open system evolution at Vulcano, Aeolian Arc, Italy. Lithos, 43, 81-106.

Dellino, P., De Astis, G., La Volpe, L., Mele, D., Sulpizio, R., 2011. Quantitative hazard assessment of phreatomagmatic eruptions at Vulcano (Aeolian Islands, Southern Italy), as obtained by combining stratigraphy, event statistics and physical modelling. Journal of Volcanology and Geothermal Research, 201, 364-384.

Di Stefano, F., Mollo, S., Ubide, T., Petrone, C. M., Caulfield, J., Scarlato, P., Nazzari, M., Andronico, D., Del Bello, E., 2020. Mush cannibalism and disruption recorded by clinopyroxene phenocrysts at Stromboli volcano: New insights from recent 2003–2017 activity. Lithos, 360, 105440.

Dufek, J., Bachmann, O., 2010. Quantum magmatism: Magmatic compositional gaps generated by melt-crystal dynamics. Geology, 38(8), 687-690.

Ellam, R. M., Harmon, R. S., 1990. Oxygen isotope constrains on the crustal contributions to the subduction-related magmatism of the Aeolian Island, Southern Italy. Journal of Volcanology and Geothermal Research, 44, 105-122.

Forni, F., Ellis, B. S., Bachmann, O., Lucchi, F., Tranne, C. A., Agostini, S., Dallai, L., 2015. Erupted cumulate fragments in rhyolites from Lipari (Aeolian Islands). Contrib. Mineral. Petrol. 170, 49.

Frezzotti, M. L., Peccerillo, A., 2004. Fluid inclusion and petrological studies elucidate reconstruction of magma conduits. Transactions American Geophysical Union, 85, 157.

Frezzotti, M. L., Peccerillo, A., Zanon, V., Nigokosian, I., 2004. Silica-rich melts in quartz xenoliths from Vulcano Island and their bearing on processes of crustal anatexis and crust - magma interaction beneath the Aeolian Arc, Southern Italy. Journal of Petrology, 45, 3-26.

Gioncada, A., Clocchiatti, R., Sbrana, A., Bottazzi, P., Massare, D., Ottolini, L., 1998. A study of melt inclusions at Vulcano (Aeolian Islands, Italy): insights on the primitive magmas and on the volcanic feeding system. Bulletin of Volcanology, 60, 286-306.

Gioncada, A., Mazzuoli, R., Bisson, M., Pareschi, M. T., 2003. Petrology of volcanic products younger than 42 ka on the Lipari-Vulcano complex (Aeolian Islands, Italy): an example of volcanism controlled by tectonics. Journal of Volcanology and Geothermal Research, 122, 191-220.

Gualda, G. A., Ghiorso, M. S., Lemons, R. V., Carley, T. L., 2012. Rhyolite-MELTS: a modified calibration of MELTS optimized for silica-rich, fluid-bearing magmatic systems. Journal of Petrology, 53(5), 875-890.

Guilbaud, M. N., Blake, S., Thordarson, T., Self, S., 2007. Role of syn-eruptive cooling and degassing on textures of lavas from the AD 1783-1784 Laki eruption, south Iceland. Journal of Petrology, 48(7), 1265-1294.

Hammer, J. E., Rutherford, M. J., 2002. An experimental study of the kinetics of decompression-induced crystallization in silicic melt. Journal of Geophysical Research: Solid Earth, 107(B1), ECV-8.

Kamenetsky, V., Clocchiatti, R., 1996. Primitive magmatism of Mt. Etna: insights from mineralogy and melt inclusions. Earth and Planetary Science Letters, 142(3-4), 553-572.

Keller, J., 1980. The island of Vulcano. Rendiconti della Società Italiana di Mineralogia e Petrografia 3 (6), 369-414.

Kress, V. C., Carmichael, I. S., 1991. The compressibility of silicate liquids containing Fe_2O_3 and the effect of composition, temperature, oxygen fugacity and pressure on their redox states. Contributions to Mineralogy and Petrology, 108(1-2), 82-92.

Kuritani, T., 1999. Phenocryst crystallization during ascent of alkali basalt magma at Rishiri Volcano, northern Japan. Journal of volcanology and geothermal research, 88(1-2), 77-97.

Le Bas, M. J., Le Maitre, R. W., Streckeisen, A., Zanettin, B., 1986. A Chemical Classification of Volcanic Rocks Based on the Total Alkali-Silica Diagram. Journal of Petrology, 27 (3), 745-750.

Mandarano, M., Paonita, A., Martelli, M., Viccaro, M., Nicotra, E., Millar, I. L., 2016. Revealing magma degassing below closed-conduit active volcanoes: Geochemical features of volcanic rocks versus fumarolic fluids at Vulcano (Aeolian Islands, Italy). Lithos, 248-251, 272-287.

Marsh, B. D., 2002. On bimodal differentiation by solidification front instability in basaltic magmas, part 1: basic mechanics. Geochimica et Cosmochimica Acta, 66(12), 2211-2229.

Masotta, M., Mollo, S., Gaeta, M., Freda, C., 2016. Melt extraction in mush zones: The case of crystal-rich enclaves at the Sabatini Volcanic District (central Italy). Lithos, 248, 288-292.

Masotta M., Mollo S., 2019. A new plagioclase-liquid hygrometer specific to trachytic systems. Minerals, 9, 375, doi:10.3390/min9060375.

Métrich, N., Rutherford, M. J., 1998. Low pressure crystallization paths of H_2O-saturated basaltic-hawaiitic melts from Mt Etna: Implications for open-system degassing of basaltic volcanoes. Geochimica et Cosmochimica Acta, 62(7), 1195-1205.

Mollo, S., Giacomoni, P. P., Coltorti, M., Ferlito, C, Iezzi, G., Scarlato, P., 2015. Reconstruction of magmatic variables governing recent Etnean eruptions: constraints from mineral chemistry and P-T-fO_2-H_2O modelling. Lithos, 212-215, 311-320.

Mollo, S., Blundy, J., Scarlato, P., De Cristofaro, S. P., Tecchiato, V., Di Stefano, F., Vetere, F., Holtz, F., Bachmann, O., 2018. An integrated P-T-H_2O-lattice strain model to quantify the role of clinopyroxene fractionation on REE+Y and HFSE patterns of mafic alkaline magmas: Application to eruptions at Mt. Etna. Earth-Science Reviews, 185, 32-56.

Moore, G., Righter, K., Carmichael, I. S. E., 1995. The effect of dissolved water on the oxidation state of iron in natural silicate liquids. Contributions to Mineralogy and Petrology, 120(2), 170-179.

Morelli, A., 1975. The gravity map of Italy. Quad. Ric. Sci., 90, 427-440.

Morimoto, N., 1988. Nomenclature of pyroxenes. Mineralogy and Petrology, 39, 55-76.

Nicotra, E., Giuffrida, M., Viccaro, M., Donato, P., D'Oriano, C., Paonita, A., De Rosa, R., 2018. Timescales of pre-eruptive magmatic processes at Vulcano (Aeolian Islands, Italy) during the last 1000 years. Lithos, 316-317, 347-365.

Paonita, A., Federico, C., Bonfanti, P., Capasso, G., Inguaggiato, S., Italiano, F., Madonia, P., Pecoraino, G., Sortino, F., 2013. The episodic and abrupt geochemical changes at La Fossa fumaroles (Vulcano Island, Italy) and related constraints on the dynamics, structure, and compositions of the magmatic system. Geochim. Cosmochim. Acta, 120, 158-178.

Papale, P., Moretti, R., Barbato, D., 2006. The compositional dependence of the saturation surface of H_2O+CO_2 fluids in silicate melts. Chemical Geology, 229(1-3), 78-95.

Peccerillo, A., Taylor, S. R., 1976. Geochemistry of Eocene calcalkaline volcanic rocks of the Kastamonu area northern Turkey. Contribution to Mineralogy and Petrology, 58, 63-81.

Peccerillo, A., Frezzotti, M. L., De Astis, G., Ventura, G., 2006. Modeling the magma plumbing system of Vulcano (Aeolian Islands, Italy) by integrated fluid-inclusion geobarometry, petrology, and geophysics. Geology, 34 (1), 17-20.

Perugini, D., Valentini, L., Poli, G., 2007. Insights into magma chamber processes from the analysis of size distribution of enclaves in lava flows: a case study from Vulcano Island (Southern Italy). J. Volcanol. Geotherm. Res., 166, 193-203.

Pinarelli, L., Gioncada, A., Capaccioni, B., Vaselli, O., Downes, H., 2019. Mantle source heterogeneity in subduction zones: constraints from elemental and isotope (Sr, Nd, and Pb) data on Vulcano Island, Aeolian Archipelago, Italy. Mineral. Petrol., 113(1), 39-60.

Piochi, M., De Astis, G., Petrelli, M., Ventura, G., Sulpizio, R., Zanetti, A., 2009. Constraining the recent plumbing system of Vulcano (Aeolian Arc, Italy) by textural, petrological, and fractal analysis: The 1739 A.D. Pietre Cotte lava flow. Geochem. Geophys. Geosyst. 10 (No Q01009).

Putirka, K. D., 2008. Thermometers and barometers for volcanic systems. Reviews in Mineralogy and Geochemistry, 69, 61-120.

Rossi, S., Petrelli, M., Morgavi, D., Vetere, F., Almeev, R. R., Astbury, R. L., Perugini, D., 2019. Role of magma mixing in the pre-eruptive dynamics of the Aeolian Islands volcanoes (Southern Tyrrhenian Sea, Italy). Lithos, 324, 165-179.

Ruch, J., Vezzoli, L., De Rosa, R., Di Lorenzo, R., Acocella, V., 2016. Magmatic control along a strike-slip volcanic arc: The central Aeolian arc (Italy). Tectonics, 35(2), 407-424.

Scarlato, P., Mollo, S., Del Bello, E., von Quadt, A., Brown, R. J., Gutierrez, E., Martinez-Hackert, B., Papale, P., 2017. The 2013 eruption of Chaparrastique volcano (El Salvador): effects of magma storage, mixing, and decompression. Chemical Geology, 448, 110-122.

Stock, M. J., Humphreys, M. C., Smith, V. C., Isaia, R., Pyle, D. M., 2016. Late-stage volatile saturation as a potential trigger for explosive volcanic eruptions. Nature Geoscience, 9(3), 249-254.

Sun, S. S., McDonough, W. F., 1989. Chemical and isotopic systematics of ocean basalts: implications for mantle composition and processes. In: Saunders, A. D., Norry, M. J.

(eds) Magmatism in the Ocean Basins. Geological Society, London, Special Publications, 42, 313-345.

Ushioda, M., Takahashi, E., Hamada, M., Suzuki, T., 2014. Water content in arc basaltic magma in the Northeast Japan and Izu arcs: an estimate from Ca/Na partitioning between plagioclase and melt. Earth, Planets Sp., 66, 1-10.

Vetere, F., Petrelli, M., Morgavi, D., Perugini, D., 2015. Dynamics and time evolution of a shallow plumbing system: the 1739 and 1888-90 eruptions, Vulcano Island, Italy. J. Volcanol. Geotherm. Res., 306, 74-82.

Waters, L. E., Andrews, B. J., Lange, R. A., 2015. Rapid crystallization of plagioclase phenocrysts in silicic melts during fluid-saturated ascent: phase equilibrium and decompression experiments. Journal of Petrology, 56(5), 981-1006.

Zanon, V., Frezzotti, M. L., Peccerillo, A., 2003. Magmatic feeding system and crustal magma accumulation beneath Vulcano Island (Italy): evidence from fluid inclusion in quartz xenoliths. Journal of Geophysical Research, 108, 2298-2301.

Figure captions

Figure 1. Schematic map of Vulcano Island. The map legend refers to the eight Eruptive Epochs as reported in De Astis et al. (2013). The rock samples object of this study have been divided in three groups according to their bulk rock compositions.

Figure 2. Olivine thermometric calculations (see SM7 for further details).

Figure 3. Probability densities for pressure, temperature and melt-H_2O content obtained by clinopyroxene-based barometry, thermometry, and hygrometry (see SM7 for further details).

Figure 4. Plagioclase-based melt-H_2O contents derived by hygrometric estimates (see SM7 for further details).

Figure 5. Titanomagnetite-based oxygen barometric estimates (see SM7 for further details).

Figure 6. Stability and proportion of minerals obtained by rhyolite-MELTS simulations. Ol, olivine. Cpx, clinopyroxene. Plg, plagioclase. Sp, spinel.

Figure 7. Liquid lines of descent calculated using rhyolite-MELTS simulations have been integrated with results from least-square mass balance calculations derived for trachytic and rhyolitic compositions.

Figure 8. Results from the application of fractional crystallization (FC), assimilation and fractional crystallization (AFC) and in-situ crystallization (ISC) models. Data are presented for simplicity as Nd vs. K_2O (a), Zr (b), TiO_2 (c) and Sr (d) diagrams. *F* is the melt fraction, *r* is the mass ratio of assimilated to crystallized material, and *f* is the fraction of residual melt returned from the solidification front to the magmatic reservoir (see SM10 for further details).

Figure 9. Plumbing system architecture of Vulcano Island in the period 54-8 ka. A deep level of magma storage is located at depth ≥ 19 km and close to the Moho transition zone, hosting hot (1190-1250 °C), H_2O undersaturated (1.6-2.0 wt.%) basaltic melts. Shallower shoshonitic-latitic reservoirs and latitic-trachytic crystal mushes are located between 5.5 and 16 km of depth, crystallizing at temperature between 1100 and 1180 °C. Rhyolitic reservoirs, at about 2 km of depth, are prevalently generated by extraction of evolved melts from crystal mushes. Rhyolitic melts stall at temperatures lower than 1100 °C and close to H_2O (2.5-4.0 wt.%) saturation.

Figures

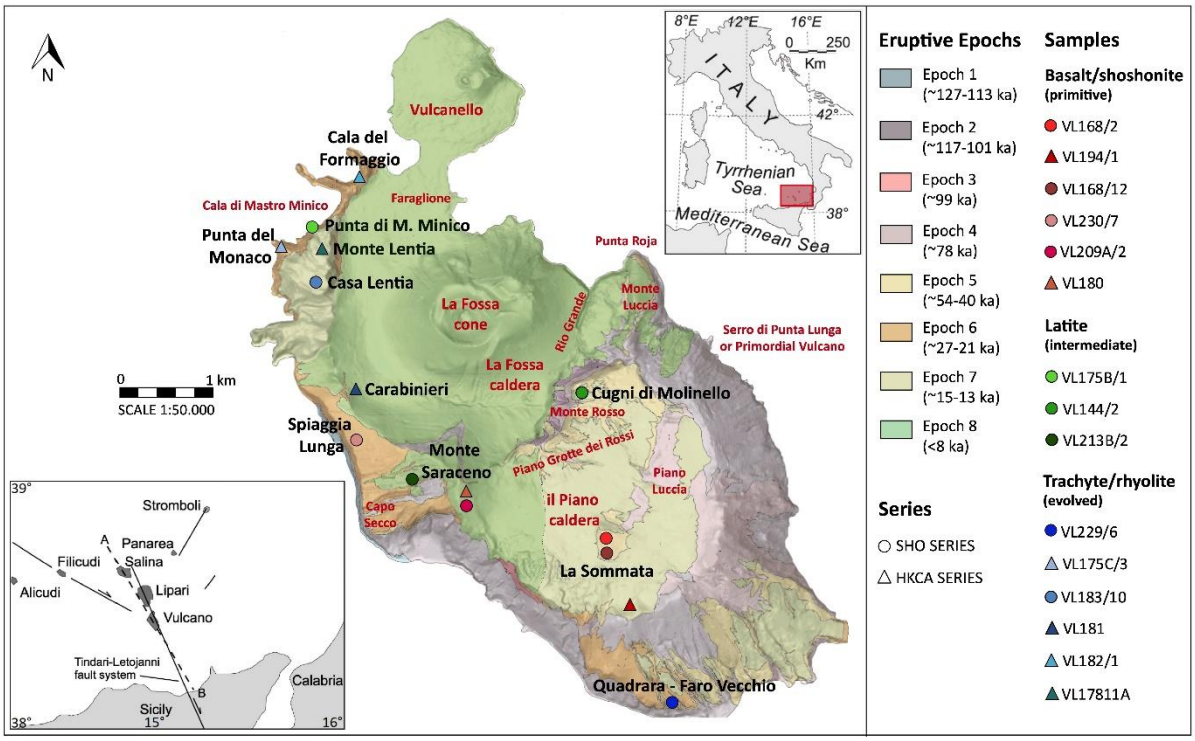

Figure 1

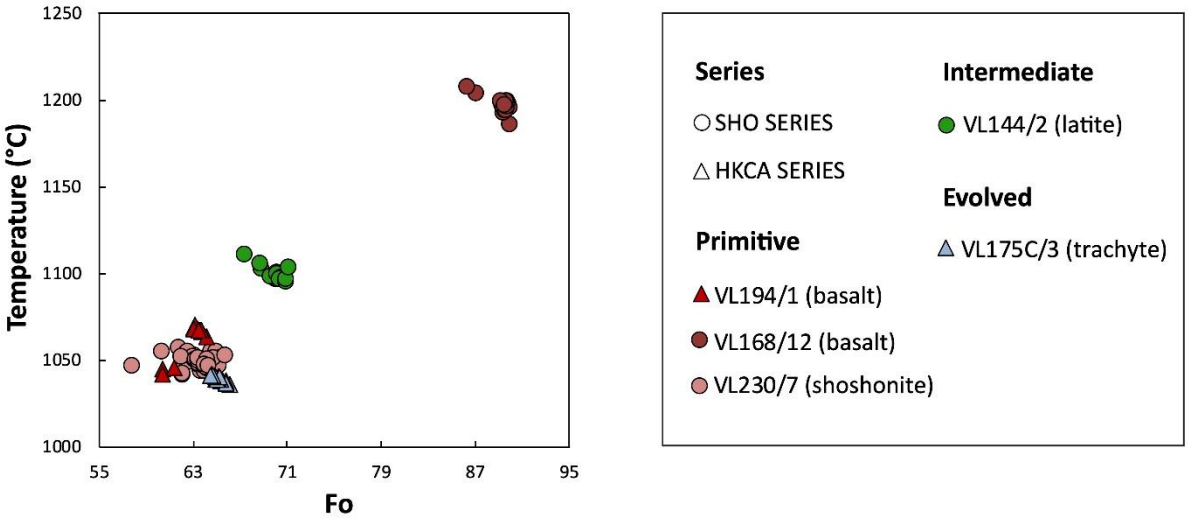

Figure 2

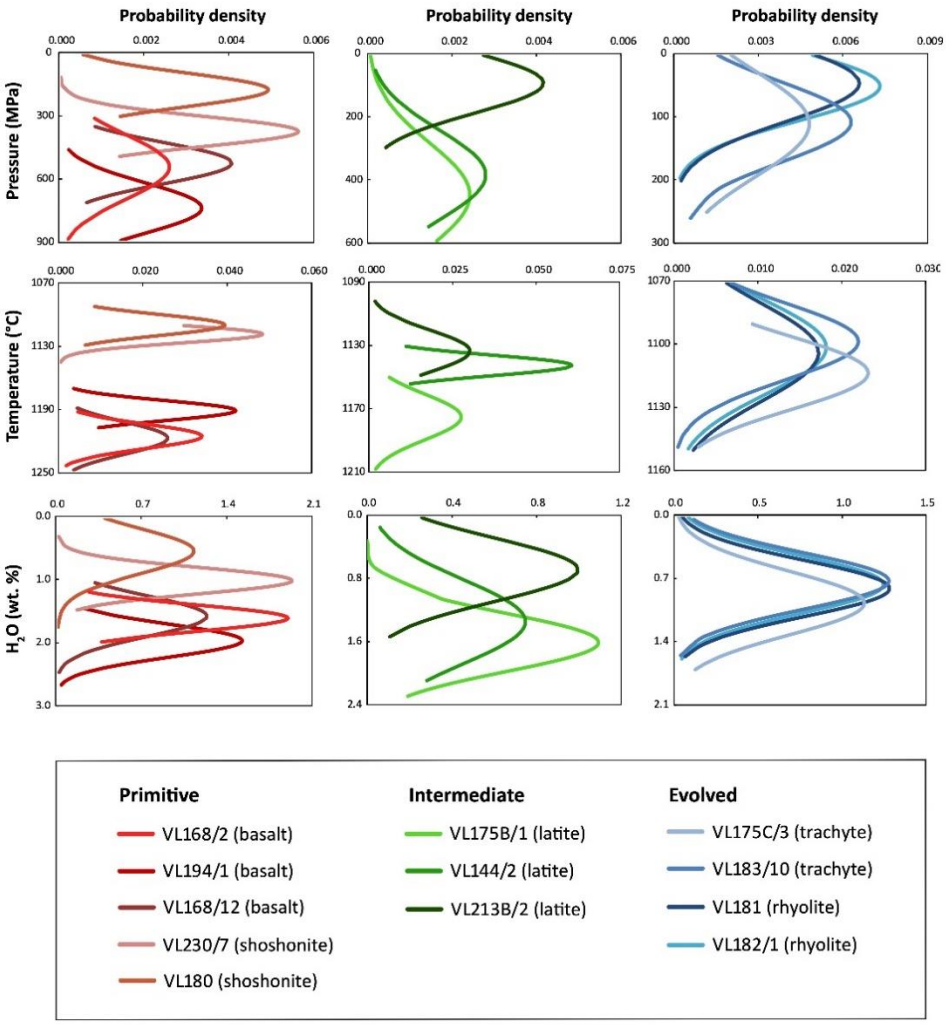

Figure 3

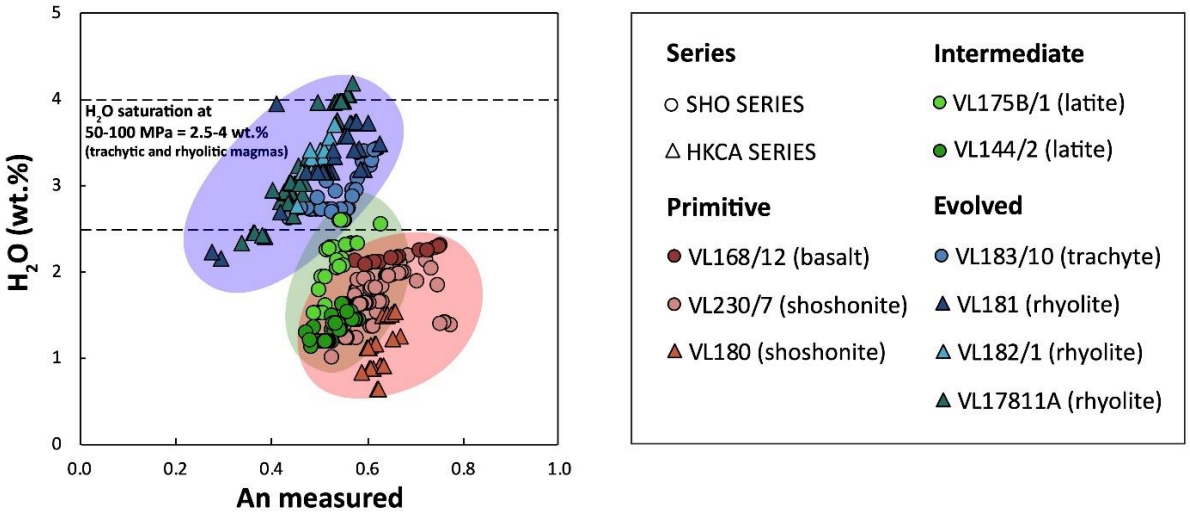

Figure 4

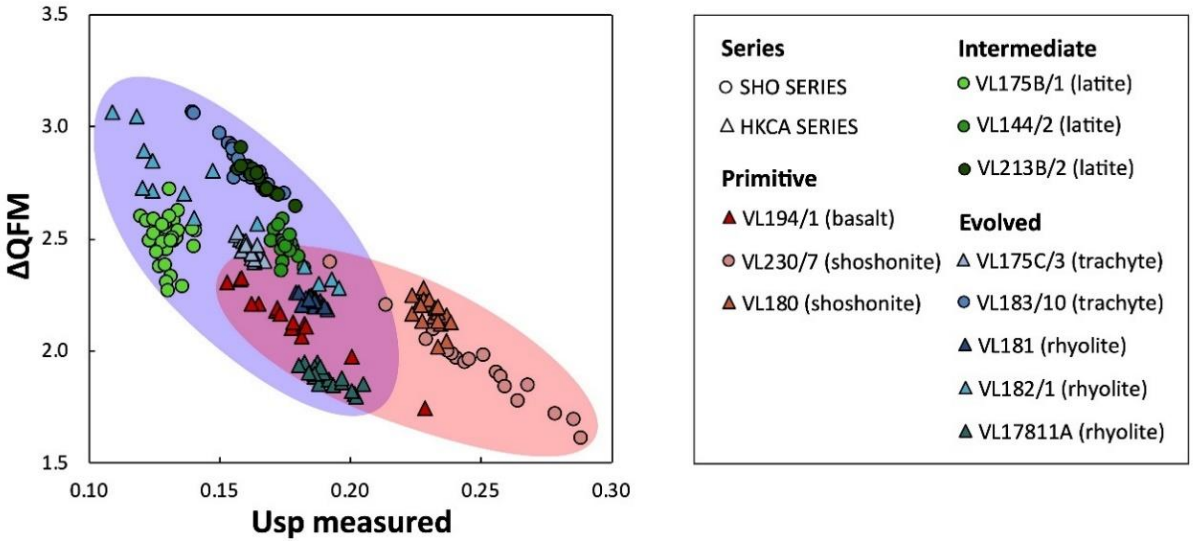

Figure 5

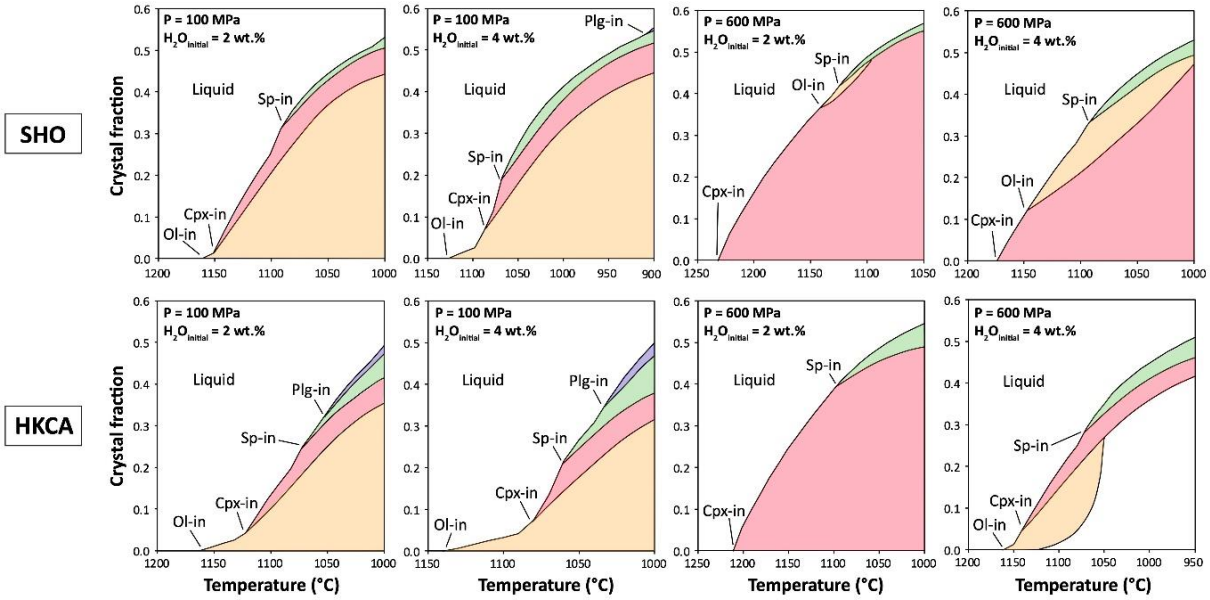

Figure 6

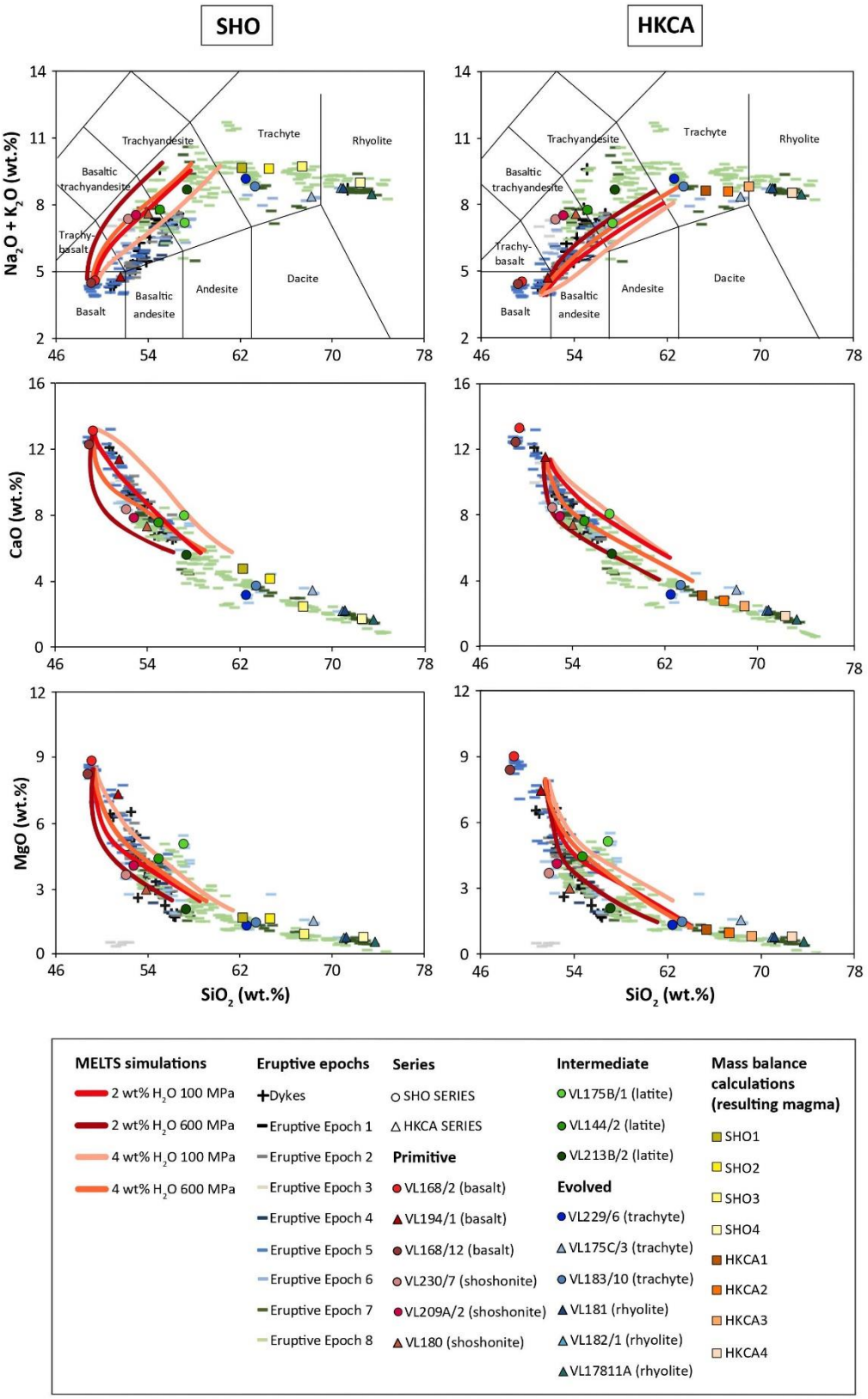
SHO
HKCA
Na2O + K2O (wt.%)
Trachyandesite
Trachyte
Rhyolite
Basaltic trachyandesite
Trachy-basalt
Andesite
Dacite
Basalt
Basaltic andesite
CaO (wt.%)
MgO (wt.%)
SiO2 (wt.%)
MELTS simulations
2 wt% H2O 100 MPa
2 wt% H2O 600 MPa
4 wt% H2O 100 MPa
4 wt% H2O 600 MPa
Eruptive epochs
Dykes
Eruptive Epoch 1
Eruptive Epoch 2
Eruptive Epoch 3
Eruptive Epoch 4
Eruptive Epoch 5
Eruptive Epoch 6
Eruptive Epoch 7
Eruptive Epoch 8
Series
SHO SERIES
HKCA SERIES
Primitive
VL168/2 (basalt)
VL194/1 (basalt)
VL168/12 (basalt)
VL230/7 (shoshonite)
VL209A/2 (shoshonite)
VL180 (shoshonite)
Intermediate
VL175B/1 (latite)
VL144/2 (latite)
VL213B/2 (latite)
Evolved
VL229/6 (trachyte)
VL175C/3 (trachyte)
VL183/10 (trachyte)
VL181 (rhyolite)
VL182/1 (rhyolite)
VL17811A (rhyolite)
Mass balance calculations (resulting magma)
SHO1
SHO2
SHO3
SHO4
HKCA1
HKCA2
HKCA3
HKCA4

Figure 7

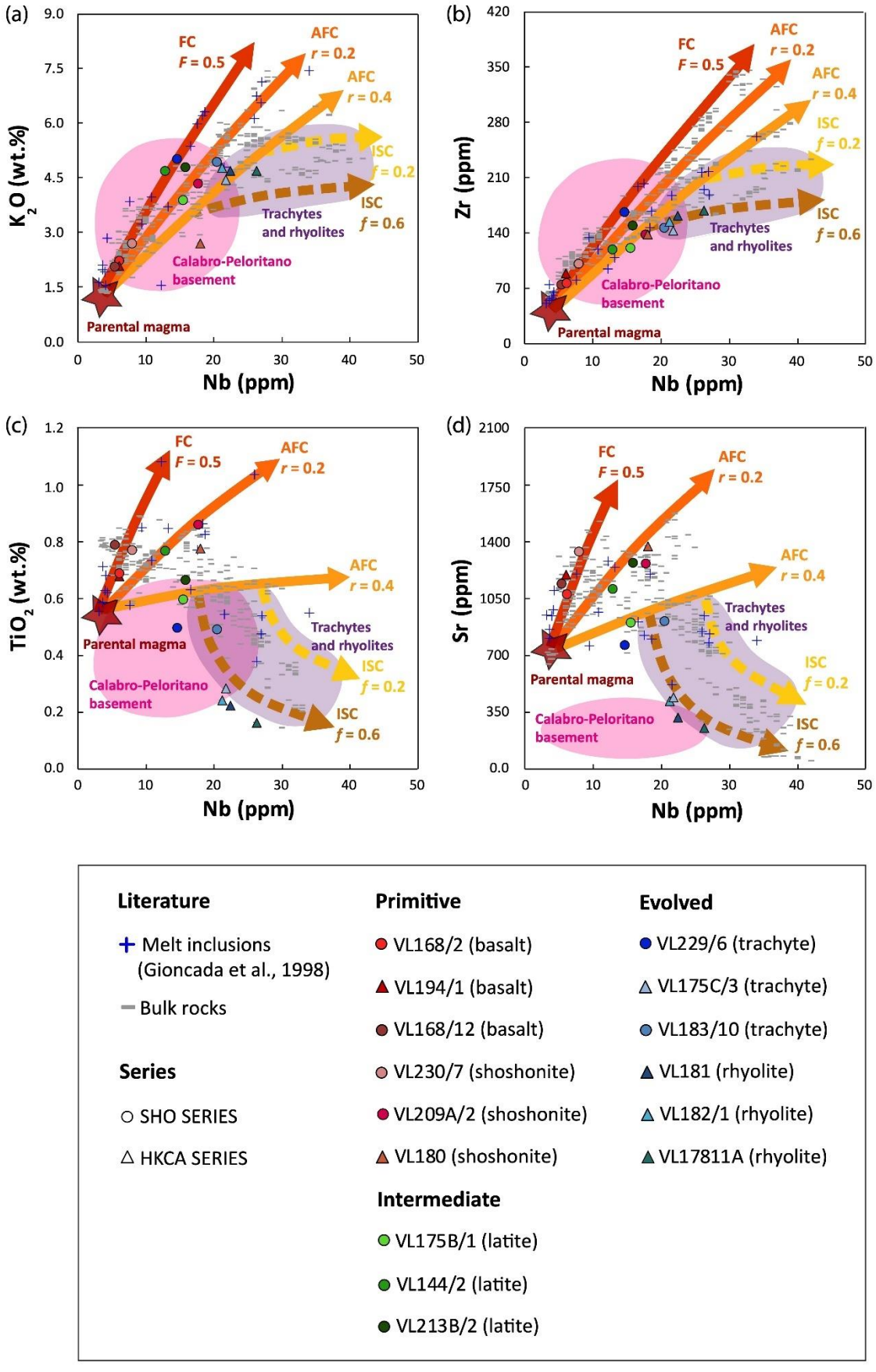
(a)
(b)
(c)
(d)
FC
F = 0.5
AFC
r = 0.2
AFC
r = 0.4
ISC
f = 0.2
ISC
f = 0.6
Trachytes
and rhyolites
Calabro-Peloritano
basement
Parental magma
K2O (wt.%)
Zr (ppm)
TiO2 (wt.%)
Sr (ppm)
Nb (ppm)
Literature
Melt inclusions
(Gioncada et al., 1998)
Bulk rocks
Series
SHO SERIES
HKCA SERIES
Primitive
VL168/2 (basalt)
VL194/1 (basalt)
VL168/12 (basalt)
VL230/7 (shoshonite)
VL209A/2 (shoshonite)
VL180 (shoshonite)
Intermediate
VL175B/1 (latite)
VL144/2 (latite)
VL213B/2 (latite)
Evolved
VL229/6 (trachyte)
VL175C/3 (trachyte)
VL183/10 (trachyte)
VL181 (rhyolite)
VL182/1 (rhyolite)
VL17811A (rhyolite)

Figure 8

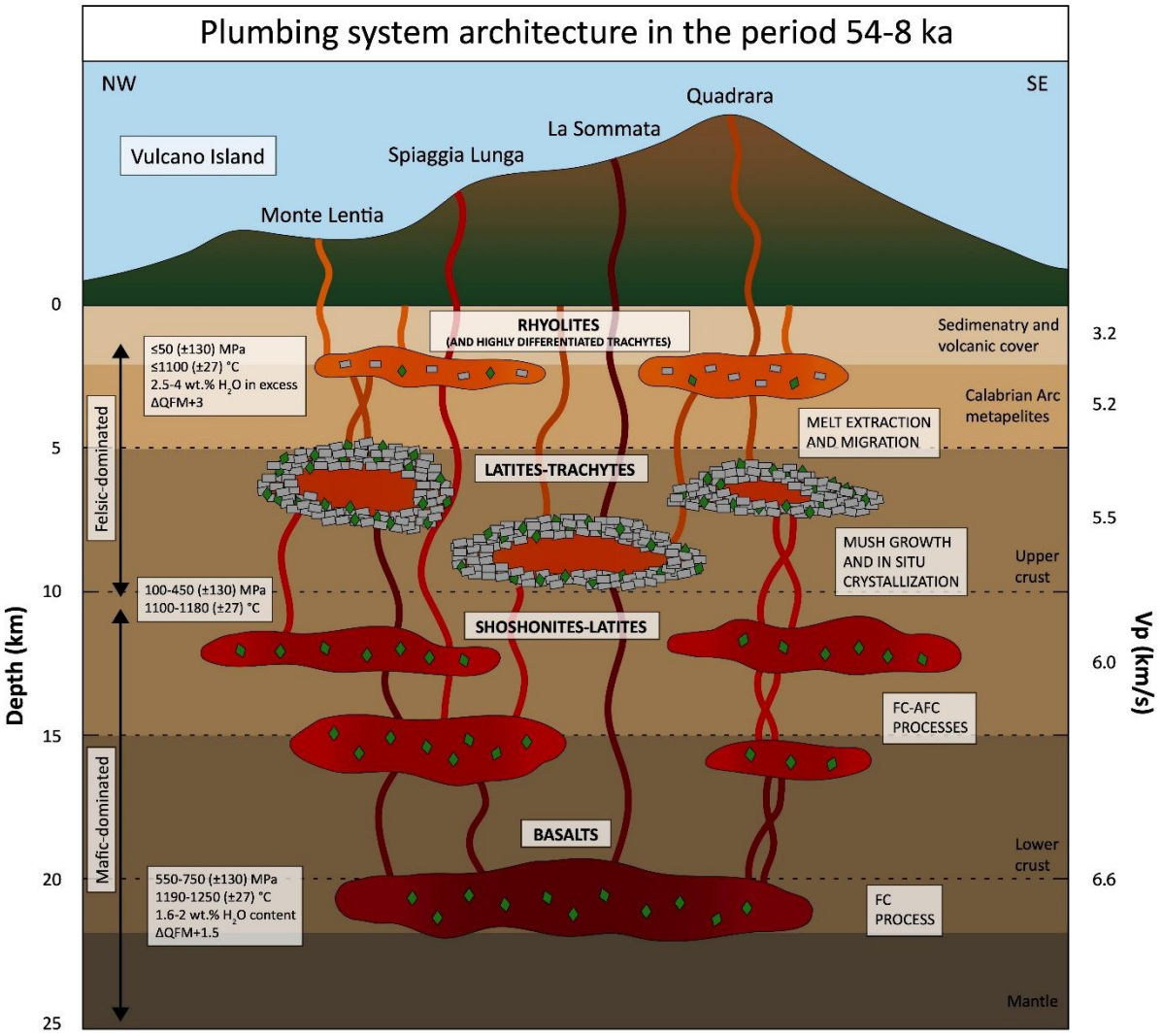

Figure 9

Supplementary data to this article can be found online at https://doi.org/10.1016/j.lithos.2020.105715.

Decoding multiple zoning patterns in clinopyroxene phenocrysts at Vulcano Island: A record of dynamic crystallization through interconnected reservoirs

[1]Flavia Palummo, [1,2]Silvio Mollo, [3]Chiara Maria Petrone, [4]Ben S. Ellis, [2]Gianfilippo De Astis, [2]Manuela Nazzari, [2]Piergiorgio Scarlato, [4]Olivier Bachmann

[1]Department of Earth Sciences, Sapienza - University of Rome, P. le Aldo Moro 5, 00185 Roma, Italy

[2]Istituto Nazionale di Geofisica e Vulcanologia - Department Roma 1, Via di Vigna Murata 605, 00143 Roma, Italy

[3]The Natural History Museum, Department of Earth Sciences, Cromwell Road, SW7 5BD, London, United Kingdom

[4]Institute of Geochemistry and Petrology, ETH Zürich, 8092 Zurich, Switzerland

Abstract

Here we document how the different growth features and intracrystalline distributions of both major and trace cations in clinopyroxene phenocrysts are important recorders of the intricate magma dynamics at Vulcano Island (Aeolian Arc, Italy). The compositions of clinopyroxene phenocrysts from products erupted over the last ~54 ka cluster at different degrees of evolution, paralleling the polybaric-polythermal differentiation of mantle-derived mafic magmas into more evolved silicic melts. The hotter lower crust is the most favorable location for the storage of mafic magmas and the early crystallization of diopsidic ($Mg\#_{91}$) clinopyroxene ($P_{max} \approx$ 750 MPa and $T_{max} \approx$ 1,220 °C). Diopsidic phenocrysts are depleted in both rare earth elements (REE) and high field strength elements (HFSE) but are enriched in transition elements (TE). The transfer and accumulation of primitive magmas in the colder upper crustal regions lead to the formation of an interconnected series of more differentiated magmatic reservoirs ($P \approx$ 100-450 MPa and $T \approx$ 1,100-1,180 °C) hosting discrete populations of clinopyroxene ($Mg\#_{84-85}$) with a broad spectrum of zonations and dissolution features. Recharge bands in clinopyroxene are markers of multiple inputs of primitive REE-HFSE-poor, TE-rich magmas from depth. Augitic phenocrysts ($Mg\#_{82}$) with strong negative Eu anomaly and REE + HFSE enrichments crystallizes from highly differentiated trachytic and rhyolitic melts stored at very shallow crustal conditions ($P \leq$ 50 MPa and $T \leq$ 1,100 °C). These silicic reservoirs represent residual melts trapped-extracted from crystal-dominated mush regions in the uppermost part of the plumbing system. The residence time of clinopyroxene increases from ~0.1 to ~44 years from basalt to rhyolite, together with an increasing number of recharge bands. The mineral assemblage in more silicic and viscous mush melts is sufficiently resilient to record numerous mafic injections and high degrees of magma mixing, hybridization, and crystallization before eruption. Overall, the compositional zoning pattern of clinopyroxene presents a picture of plumbing system that extends through the crust and is characterized by

distributions of melts and crystals which are progressively more evolved and heterogeneous in both space and time.

1. Introduction

Vulcano Island (Aeolian Arc, Italy) is characterized by a broad spectrum of clinopyroxene-bearing eruptive products, with a general temporal variation in compositions from basalt to rhyolite (e.g., Keller, 1980; Ellam et al., 1988; De Astis et al., 1997, 2013). The volcanic history is controlled by the continuous supply of mafic magma from mantle depths into shallow crustal levels, where high degrees of mixing and fractional crystallization lead to the formation of more differentiated reservoirs, together with occasional assimilation of small amounts of crustal materials (Bullock et al., 2019; Costa et al., 2020, 2021; De Astis et al., 1997; Gioncada et al., 1998, 2003; Forni et al., 2015; Nicotra et al., 2018; Palummo et al., 2020; Peccerillo et al., 2006; Piochi et al., 2009; Zanon et al., 2003).

The picture emerging from geophysical, volcanological, and petrological considerations is entirely consistent with a plumbing system that extends vertically through the crust and is characterized by a multi-faceted geometry (Clocchiatti et al., 1994; De Astis et al., 1997, 2013; Peccerillo et al., 2006; Zanon et al., 2003; Costa et al., 2020, 2021; Nicotra et al., 2018; Palummo et al., 2020). Considering this articulated architecture, we infer that complex zoning patterns in clinopyroxene phenocrysts have the potential to integrate a broad range of spatio-temporal information, providing an important record of the physico-chemical changes of magmas (Forni et al., 2016; Mollo et al., 2015, 2020a; Szymanowski et al., 2016; Ubide et al., 2019a; Welsch et al., 2016;). Clinopyroxene is an important recorder of mixing, hybridization, and differentiation mechanisms that control the dynamics of magma within the crust and, ultimately, preserves a detailed record of the magma recharge history (Di Stefano et

al., 2020; Dunworth et al., 2001; Gioncada et al., 2005; Mangler et al., 2020; Tecchiato et al., 2018; Ubide et al., 2019b). Deconvolution of systematic zoning patterns in clinopyroxene may help to reconstruct the recharge dynamics of magma reservoirs, as well as the time and length scales required to mobilize magmas before eruptions (e.g., Petrone et al., 2016, 2018; Ubide and Kamber, 2018). Additionally, the stability field of clinopyroxene encompasses a broad range of *P-T-X* conditions, from mantle depths to very shallow crustal levels, and its crystallization may strictly control the geochemical evolution of solidifying melts in terms of major and trace element contents (e.g., Beard et al., 2019; Masotta et al., 2013; Mollo and Masotta, 2014; Mollo et al., 2015; Putirka et al., 2008; Perinelli et al., 2016; Sun and Liang, 2012, 2017).

Although the investigation of clinopyroxene complexity and diversity can be a powerful tool to gain information on the dynamics of multi-stage plumbing systems, no studies have yet categorized and decoded the complex zoning patterns of clinopyroxene at Vulcano Island. For this purpose, we present a broad compositional data set for major and trace elements analyzed in clinopyroxene phenocrysts from twenty-one basaltic-to-rhyolitic products representative of the volcanism occurred from ~54 ka to historical times. A detailed petrological description, geochemical modeling, and petrogenetic significance of fifteen products with ages in the range of ~8-54 ka can be found in Palummo et al. (2020). Here the data set has been integrated with six latitic and trachytic rock samples, which extend the eruptive period to the youngest product of La Fossa cone dated at 1739 CE on the basis of contemporary historical chronicles (see De Astis et al., 2013 and references therein). Interrogation of the textural and compositional changes of clinopyroxene reveals that zonations are intrinsic to the process of magma solidification, thus providing a more comprehensive view of the geochemical evolution of multiple magma batches undergoing polybaric-polythermal crystallization under open-system conditions. The interpretation and modeling of major and trace cation distributions in

clinopyroxene affords considerable insight into the mechanisms and timescales by which multiple magma storage regions developed at variable depths and then interacted with each other, before feeding volcanic eruptions.

2. Vulcanological background

Vulcano Island is an active volcanic system located in the southernmost sector of the Aeolian Archipelago (Fig. 1a), a Quaternary volcanic arc generated by subduction of the oceanic Ionian plate underneath the Calabrian arc (Ventura, 2013). The Aeolian Archipelago consists of seven islands and nine seamounts forming a ring-like structure, whose northwestern sector lies on the oceanic crust of the Tyrrhenian abyssal plain and eastern and southern sectors on ~18-25 km thick continental crust of the Calabro-Peloritano basement (De Astis et al., 1997). The three islands of Vulcano, Lipari, and Salina are part of a volcanic complex that developed within a graben-like structure controlled by the NNW-SSE strike-slip Tindari–Letojanni fault system (Gioncada et al., 2003; Ventura, 2013). Accordingly, the structural pattern of Vulcano Island is dominated by major NW–SE- to NNW–SSE-striking fault system (De Astis et al., 2013). The island has a total surface area of ~22 km^2, its base lies at an average depth of ~1 km b.s.l. and the maximum height is ~499 m a.s.l. at Monte Aria (De Astis et al., 2013 and references therein). The calc-alkaline affinity of the erupted products is related to subduction processes due to the presence of a NW-dipping Benioff-Wadati zone (Davì et al., 2009). The subaerial volcanic activity at Vulcano Island started 127 ka in the southern sector of the island with the building of Primordial Vulcano stratocone (Fig. 1a; Mandarano et al., 2016). Afterwards, the volcanic edifice was affected by volcano-tectonic collapses occurring at 100, 80, and 50 ka. The first two collapses were related to the formation of Il Piano caldera, whereas the third collapse was associated to the early phases of La Fossa caldera (Fig. 1a; Davì

et al., 2009). The last eruption occurred from August 1888 to March 1890 at La Fossa cone (Keller, 1980). This is a 391-m-high tuff cone mainly developed through phreatomagmatic eruptions and minor lava effusions (Dellino et al., 2011). The peninsula of Vulcanello (Fig. 1a) formed as a new islet in Roman times. This peninsula represents the northernmost structure located along the northern border of La Fossa caldera, consisting of a lava platform and three nested scoria cones with alignment ENE-WSW (Davì et al., 2009; De Astis et al., 1997, 2013). According to De Astis et al. (2013), the overall eruptive history of Vulcano Island can be divided in eight Eruptive Epochs (Fig. 1a) that represent the principal building stages of the volcanic edifice interrupted by periods of quiescence, sometimes also associated with volcano-tectonic collapses (e.g., Il Piano Caldera, La Fossa Caldera).

3. Sampling and analytical methods

3.1. Sample selection

The magmatic activity of the last ~54 ka at Vulcano Island has been investigated through textural and chemical (major and trace elements) analyses of clinopyroxene phenocrysts (i.e., crystals with longest size dimensions >0.3 mm; Lanzafame et al., 2013 and references therein) from various volcanic rocks, mainly lavas and scoriae, erupted during the considered timespan.

A total of twenty-one rock samples, were collected from several strategic sectors and formations, in which the eruptive units were identified on the basis of their different lithostratigraphic and compositional characteristics (Table 1). The rock samples represent the last Eruptive Epochs 5, 6, 7, and 8 (i.e., between ~54 ka and 1739 CE; De Astis et al., 2013) of Vulcano Island (Fig. 1a). According to the TAS diagram (Total Alkali vs. Silica; Le Bas et al., 1986; Fig. 1b), samples are classified as five distinct groups: 1) basalts (SiO_2 ≈ 48.9-51.4 wt.%; $Na_2O + K_2O$ ≈ 4.3-4.6 wt.%), 2) basaltic trachyandesites (i.e., shoshonites; SiO_2 ≈ 52.2-54.4

wt.%; $Na_2O + K_2O \approx 7.3$-7.9 wt.%), 3) trachyandesites (i.e., latites; $SiO_2 \approx 54.2$-57.5 wt.%; $Na_2O + K_2O \approx 7.1$-9.2 wt.%), 4) trachytes ($SiO_2 \approx 62.4$-68.4 wt.%; $Na_2O + K_2O \approx 8.3$-9.1 wt.%) and 5) rhyolites ($SiO_2 \approx 71.0$-73.7 wt.%; $Na_2O + K_2O \approx 8.5$-8.7 wt.%). Bulk rock analyses of rock samples and a detailed description of their eruptive epochs are reported in Supplementary Material 1.

3.2. Analytical methods

Textural and chemical microanalyses on clinopyroxene phenocrysts were carried out with a field emission gun-scanning electron microscope (FE-SEM) and an electron microprobe (EMP), respectively, installed at the High Pressure - High Temperature (HP-HT) Laboratory of Experimental Volcanology and Geophysics of the Istituto Nazionale di Geofisica e Vulcanologia (INGV) in Rome (Italy). Trace element analyses of clinopyroxene phenocrysts were determined by laser ablation-inductively coupled plasma-mass spectrometry (LA-ICP-MS) at the Institute of Geochemistry and Petrology, ETH Zürich (Switzerland). Conditions used for analyses are reported in Supplementary Material 1.

4. Results

4.1. Clinopyroxene textural and chemical zonation

Clinopyroxene is the ubiquitous mineral phase in all the investigated samples and usually the length of its longest axis is comprised between 0.3 and 1 mm. Distinctive and complex textural changes are observed for clinopyroxene by combining grey level distribution of high-contrast BSE (backscattered electron) images (Fig. 2) and X-ray microprobe maps in false colors (Fig. 3). On this basis, five main clinopyroxene populations have been identified (Table 1):

- Type 1: unzoned phenocrysts. Euhedral phenocrysts with homogeneous compositions are extremely rare in the erupted products (Fig. 2). Unzoned phenocrysts are prevalently found in basalts and some primitive shoshonites, whereas they are absent in latites, trachytes and rhyolites (Table 1);
- Type 2: cores/resorbed cores. Several phenocryst cores are heralds of an early stage of crystallization and one or more resorbed cores preserve evidence of dissolution. In BSE photomicrographs, subhedral-to-anhedral dark grey (low mean atomic number) crystal portions are surrounded by light grey (high mean atomic number) mantles + rims (Figs. 2 and 3). The innermost parts of resorbed cores are unaffected by dissolution features, showing compositions identical to those of the homogeneous cores. Accordingly, resorbed cores represent early-formed cognate clinopyroxenes that crystallized in equilibrium with the resident magma before partial dissolution and recrystallization caused by injections of hotter recharge melts;
- Type 3: recharge bands. Dark grey concentric growth zones developed within the clinopyroxene light grey mantle (Figs. 2 and 3). These recharge bands show sharp interfaces and are composed of continuous, planar segments, each of which responds to growth under a certain crystal face. Within any given concentrically zoned overgrowth, the BSE intensity changes across the growth crystal boundary in the same sense, denoting that recharge bands are time-equivalent growth surfaces forming by supply of new magma to the advancing crystalline layer (Fig. 2 and 3). The darker BSE intensity of clinopyroxene cores, resorbed cores, and recharge bands is ascribed to higher contents of MgO and Cr_2O_3 and lower contents of Al_2O_3 and FeO compared to phenocryst mantles + rims (Fig. 3). Phenocrysts with recharge bands are more common in trachyte and rhyolite samples than in other rock types (Table 1);

- Type 4: mottled phenocrysts. Aggregation and/or conjoining of mutually touching resorbed crystals (Fig. 2), with indistinct boundaries due to the effect of dissolution (Dunworth et al., 2001). Mottled crystals are found from shoshonitic-to-rhyolitic products and their frequency increases with increasing degree of melt differentiation (Table 1). Irregular crystal portions show contrasting compositions, with both dark grey and light grey domains that are similar to those of resorbed cores and testify to dissolution and recrystallization of crystal aggregates during magma mixing;
- Type 5: sector-zoned phenocrysts. Sector zoning in clinopyroxene consists of hourglass (or basal) forms {-1 1 1} and prism forms {*h k* 0}, including {1 0 0}, {1 1 0}, and {0 1 0} faces. Sectors are identified by changes in BSE intensity from darker hourglass to lighter prism (Fig. 2) and are found only in shoshonites and latites (Table 1). Hourglass sectors grow faster along the c-axis, whereas prism sectors grow slower perpendicular to the *c* crystallographic axis (e.g., Ubide et al., 2020 and references therein). A growth sector boundary marks the interface between adjacent {-1 1 1} and {*h k* 0} forms, showing shapes either straight or slightly curved due to local variations in growth rates on the two faces (Fig. 2). Hourglass sectors are enriched in SiO_2 + MgO and depleted in Al_2O_3 + FeO_{tot} compared to prism sectors (Fig. 3). Both these sectors are sometimes crossed by concentric banding with sharp interfaces subparallel to the growing sector boundary (Fig. 2).

4.2. Clinopyroxene major elements

The whole data set derived for clinopyroxene major and trace element analyses is reported in Supplementary Material 1, together with variation diagrams where all the compositions of clinopyroxene cores, mantles + rims, and recharge bands are displayed on single plots.

Using the classification scheme reported in the review of Mollo et al. (2020b), we have calculated clinopyroxene cation fractions (X) and components (i.e., diopside, Di, $CaMgSi_2O_6$; hedenbergite, Hd, $CaFeSi_2O_6$; enstatite, En, $Mg_2Si_2O_6$; ferrosilite, Fs, $Fe_2Si_2O_6$), for each crystal population. Clinopyroxene cores are classified as diopside to diopside-augite (Di_{66-83}-Hd_{9-19}-En_{7-11}-Fs_{1-3}), whereas recharge bands and mantles + rims can be classified as augite (Di_{64-73}-Hd_{13-20}-En_{11-12}-Fs_{2-4} and Di_{65-61}-Hd_{19-21}-En_{13-16}-Fs_{4-5}, respectively).

Fig. 4 shows the Mg-number [Mg# = X_{Mg} / (X_{Mg} + X_{Fe2+}), where X is the cation fraction and all iron is expressed as Fe^{2+}] of clinopyroxene plotted against the sum of Di + Hd components (i.e., ΣDiHd) and the concentration of TiO_2 in phenocryst cores and phenocryst mantles + rims compared with recharge bands. The most relevant crystal chemical changes are presented here as average compositions of single samples. This comparison highlights that ΣDiHd decreases from clinopyroxene cores + recharge bands (0.80-0.88 on average) to clinopyroxene mantles + rims (0.76-0.79 on average). Conversely, the concentration of TiO_2 increases from 0.2 to 0.6 wt.% on average, as the growth of clinopyroxene takes place in more differentiated melt compositions (Fig. 4).

The Mg# of phenocryst cores abruptly decreases from basalts ($Mg\#_{91}$ on average) to shoshonites + latites ($Mg\#_{84-85}$ on average) to trachytes ($Mg\#_{82}$ on average) to rhyolites ($Mg\#_{78}$ on average), resembling the geochemical evolution of the host rocks (compare Figs. 1 and 4). Importantly, clinopyroxene is an early liquidus phase and its core is in equilibrium with the bulk rock composition as previously determined by Palummo et al. (2020). The equilibrium condition between clinopyroxene core and bulk rock compositions has been tested by the Fe-Mg exchange (0.28 ± 0.08) of Putirka (2008), in conjunction with models based on the difference (Δ) between measured vs. predicted ΣDiHd components (Mollo et al., 2013; Mollo and Masotta, 2014) and thermodynamically-predicted partition coefficients for Na (Blundy et al., 1995) and Ti (Mollo et al., 2018, 2020). Due to the effects of magma mixing and

hybridization phenomena, the equilibrium partitioning of Fe, Mg, Ti, and Na cations between the early-formed core and host magma has been restored by adding/subtracting to the bulk rock minimum amounts of minerals along the olivine-clinopyroxene-plagioclase cotectic (see supplementary data in Appendix A of Palummo et al., 2020). ΣDiHd decreases with proceeding magma differentiation from basalts (0.88 ± 0.01 on average) to latites + shoshonites + less differentiated trachytes (0.83 ± 0.01 on average) to more differentiated trachytes + rhyolites (0.80-0.82 ± 0.01 on average). The amount of TiO_2 in clinopyroxene remains almost identical from shoshonite to rhyolite (0.3-0.4 wt.% ± 0.04 on average). Conversely, diopsidic phenocrysts from mantle-derived basaltic rocks are characterized by lower TiO_2 concentrations (0.2 ± 0.04 wt.% on average; Fig. 4).

The entire compositional range of recharge bands is between $Mg\#_{80}$ and $Mg\#_{88}$, with an average of $Mg\#_{82}$ (Fig. 4). Recharge bands are more differentiated than diopsidic cores found in mantle-derived basalts and mimic the chemistry of clinopyroxene cores from shoshonites, latites, and trachytes. This compositional feature supports the idea of a polybaric-polythermal magmatic differentiation within the crust that proceeds in cooperation with recurrent mixing and hybridization processes (Gioncada et al., 2003). A small population of recharge bands from rhyolites (~13% of the whole data set) exhibits low TiO_2 abundances (≤0.2 wt.%; Fig. 4) resulting from the increased stability of titanomagnetite in the upper crust (Palummo et al., 2020).

Clinopyroxene mantles + rims from basalts to rhyolites depict a narrower and more evolved compositional range of $Mg\#_{75\text{-}78}$ relative to phenocryst cores + recharge bands (Fig. 4). The amount of ΣDiHd significantly decreases in clinopyroxene mantles + rims, especially due to strong CaO depletion caused by the incipient late-stage crystallization of feldspar (plagioclase + sanidine) during magma cooling and decompression (De Astis et al., 2013).

Clinopyroxene mantles + rims from basalts ($Mg\#_{78}$ on average) remain systematically less differentiated than those ($Mg\#_{76}$ on average) from other rocks. Most of the compositions of mantles + rims from shoshonites to rhyolites overlap, without displaying any clear evolutionary trend neither for ΣDiHd or TiO_2 (Fig. 4). Clinopyroxene mantles + rims from latites ($Mg\#_{75}$ on average) are slightly more evolved than those from rhyolites ($Mg\#_{76}$ on average), in agreement with the increased number of recharge bands observed in phenocrysts from silicic host rocks and suggesting recurrent inputs of fresh and more primitive magmas from depth (Table 1).

4.3. Clinopyroxene trace elements

The chondrite-normalized patterns (Sun and McDonough, 1989) of rare earth elements (REE) in clinopyroxenes exhibit sub-parallel trends, shifting towards progressive trace element enrichments from basalt to rhyolite according to the more differentiated character of magma (Fig. 5). The concentration of light REE (LREE) is typically higher than that of heavy REE (HREE). Clinopyroxene mantles + rims exhibit lower LREE/HREE ratios (i.e., the normalized La/Yb ratio; La_N/Yb_N) and more pronounced negative Eu anomalies (i.e., $Eu/Eu^* = Eu_N/(Sm_N \times Gd_N)^{0.5}$) than clinopyroxene cores and recharge bands (Fig. 5). From basalts to rhyolites, both Eu/Eu* and La_N/Yb_N measured in clinopyroxene cores decrease from ~0.92 ± 0.06 to ~0.61 ± 0.06 on average and from ~2.8 ± 0.2 to ~2.3 ± 0.2 on average, respectively. In clinopyroxene mantles + rims, the values of Eu/Eu* and La_N/Yb_N further decrease to ~0.5 and ~2.0, respectively, responding to the abundant crystallization of feldspar at the late stage of melt differentiation.

The primordial mantle-normalized patterns (Sun and McDonough, 1989) of trace elements in clinopyroxenes show typical features of arc magmas, with enrichments in large ion lithophile element (LILE) to high field strength element (HFSE) ratios (Fig. 5). Both

clinopyroxene cores, recharge bands, and mantles + rims display troughs at Ba, K, Nb, P, Zr, and Ti in (Fig. 5). The concentration of incompatible elements in clinopyroxene cores shows a marked increase from basalts to rhyolites, while the incompatible element concentrations partly overlap in clinopyroxene mantles + rims from trachytes to rhyolites (Fig. 5). Negative spikes of K, Sr, P, and Ti are more marked in clinopyroxene cores from trachytes and rhyolites, in agreement with the phase assemblage (i.e., feldspar + oxide ± apatite) that characterizes the more differentiated eruptions.

From clinopyroxene cores to recharge bands to mantles + rims, the amount of compatible transition elements (TE) decreases from 1,005 to 242 ppm and from 99 to 89 ppm for Cr and Ni, respectively. In particular, Cr is extremely high in phenocrysts from basalts (2,131 ± 102 ppm on average) relative to those from rhyolites (440 ± 107 ppm on average) and is well correlated with the Mg# of clinopyroxene. Conversely, V, Co, and Zn behave like incompatible elements and their average concentration increases with the host rock differentiation from 126 to 209 ppm, from 41 to 54 ppm, and from 40 to 76 ppm, respectively (Supplementary Material 1).

Scandium is highly compatible in clinopyroxene (cf. Mollo et al., 2020a) and its concentration decreases from clinopyroxene cores (87 ± 4 ppm on average) to mantles + rims (76 ± 2 ppm on average), resembling the progressive melt depletion with proceeding crystallization (Supplementary Material 1).

5. Discussion

5.1. The geochemical evolution of clinopyroxene

Fig. 6 shows that the differentiation path of magmas is faithfully recorded by major and trace element contents of clinopyroxene cores from products with different degrees of evolution. Diopsidic cores ($Mg\#_{91}$) from mantle-derived basalts support the idea of a unique deep level of magma, whose bulk composition is characterized by low incompatible LREE (i.e., Ce) and HFSE (i.e., Zr) concentrations, in conjunction with high TE/HREE ratios (i.e., Cr/Yb and V/Yb ratios; Fig. 6). Forsteritic ($Fo_{87–91}$) olivines are in equilibrium with diopsidic cores and the homogenization temperature of olivine-hosted melt inclusions indicates crystallization at $T \approx$ 1,190–1,250 °C (Gioncada et al., 1998). Thermobarometric constraints and thermodynamic calculations based on the equilibrium between clinopyroxene core and bulk rock compositions (see above), confirm that diopsidic phenocrysts equilibrated with primitive basaltic magmas at $P_{max} \approx$ 750 MPa and $T_{max} \approx$ 1,220 °C (Fig. 7). Primitive basaltic magmas are inferred to originate at mantle depths via partial melting of a depleted peridotitic source veined by metasomatic, clinopyroxene-rich regions (Kamenetsky and Clocchiatti, 1996). The occurrence of a mafic mineral assemblage in equilibrium with deep-seated magmas is in accordance with a Moho depth estimated at ~21–25 km, corresponding to $P \approx$ 620–740 MPa for a continental crust density of 2.7 g/cm^3 (Peccerillo et al., 2006 and references therein).

The *P*-*T* array traced by the crystallization of clinopyroxene changes significantly as the basaltic magmas migrate and differentiate towards two shallower and colder storage regions hosting 1) shoshonitic, latitic, and less differentiated trachytic melts at $P \approx$ 100-450 MPa and $T \approx$ 1,100-1,180 °C and 2) highly differentiated trachytic and rhyolitic melts at $P \leq$ 50 MPa and $T \leq$ 1,100 °C (Fig. 7). As *P* decreases, the stability field of clinopyroxene decreases in favor of olivine crystallization (Palummo et al., 2020) and the clinopyroxene composition shifts from

diopside-augite ($Mg\#_{84-85}$) to augite ($Mg\#_{82-77}$). More evolved magmas residing at shallower crustal conditions are saturated with feldspar and titanomagnetite at $T < 1{,}100$ °C (Fig. 7). The abundant formation of plagioclase is also promoted by cooling-decompression regimes related to H_2O exsolution and degassing (cf. Mandarano et al., 2016 and references therein). Ce and Zr enrichments in clinopyroxene cores from basalts to rhyolites are in accord with the progressive differentiation of magma (Fig. 6). The Mg# of clinopyroxene plotted against the TE/HREE ratio highlights that basalts, shoshonites + latites, and trachytes + rhyolites cluster at different degrees of evolution (Fig. 6). In particular, the abrupt decrease of Cr/Yb ratio from basalts (9,500-12,500) to shoshonites + latites (500-2,500) to trachytes + rhyolites (100-500; Fig. 6) confirms the early and extensive crystallization of mafic minerals (olivine + clinopyroxene), in which Cr is prevalently incorporated (e.g., Tecchiato et al., 2018). As the composition of magma evolves, the concentration of incompatible Ce and Zr elements progressively increases in clinopyroxene cores. At the same time, the increasing stability of plagioclase leads to stronger negative Eu anomalies (Eu/Eu*) and lower LILE/HREE ratios (i.e., Sr/Yb ratios), especially for trachytes and rhyolites (Fig. 6). Silicic magmas are stored in upper and colder crustal environments located at $P \leq 50$ MPa (Fig. 7) and, likely, are generated by the extraction of interstitial melts from crystal-rich (mushy) reservoirs. Abundant segregation of feldspar phenocrysts is inferred to be responsible for the development of distinct magma-mush pockets (Palummo et al., 2020; Nicotra et al., 2018). Feldspar-liquid separation processes can be also favored by second boiling of the melt and consequent volatile exsolution of a fluid phase at $T \approx 860$–$1{,}100$ °C and H_2O concentrations in excess of ~2.5–4.0 wt.% (Gioncada et al., 2003; Costa et al., 2020; Palummo et al., 2020).

Intracrystalline heterogeneities in clinopyroxene are recorders of recurrent magma recharge and mixing events (Type 3 recharge bands; Figs. 2 and 3), generally accompanied by multi-stage crystal dissolution phenomena (Type 2 resorbed cores and Type 4 mottled

aggregates; Figs. 2 and 3). Resorbed cores are interpreted as evidence of corrosion by thermal and/or chemical disequilibrium with the melt. This open-system behavior is caused by the injection of hotter and more mafic magmas into compositionally distinct reservoirs within the crust (Bullock et al., 2019; Costa et al., 2020; De Astis et al., 2013; Nicotra et al., 2018). Concentric Cr zonation in clinopyroxene indicates subtle modulations in the history of melt composition involved in clinopyroxene growth (Fig. 3). Several clinopyroxene phenocrysts contain Cr-rich resorbed cores that likely formed by replenishment of the crystallizing reservoir. These cores were partially dissolved during protracted storage at magmatic temperature and finally incorporated into the new recharge melt (Ubide and Kamber, 2018; Mollo et al., 2020a). Owing to the broad compositional range of clinopyroxene-bearing magmas (Fig. 1a), the destabilization-dissolution of clinopyroxene cores is probably controlled by mutual thermal and chemical effects caused by the transport of crystals through the upper crust (e.g., Mollo and Masotta, 2014; Forni et al., 2016, 2018). In a similar fashion, the formation of Type 3 concentrically zoned phenocrysts can be ascribed to repeated recharge events that are inferred to be drivers of convective dynamics in crustal storage regions (Bergantz et al., 2015). Given that some Cr-rich bands developed at the clinopyroxene rim (Fig. 3), it is plausible that the eruption was triggered by the injection of mafic magma (Ubide and Kamber, 2018; Petrone et al., 2018). Magma mixing is frequently suggested as an effective eruption trigger (Sparks et al., 1977; Druitt et al., 2012) and is sometimes associated with volatile exsolution during magma ascent from depth towards the surface (Cashman et al., 2017).

Fig. 8 shows that recharge bands ($Mg\#_{81-85}$) are markers of primitive REE-HFSE-poor, TE-rich magmas injecting into more differentiated REE-HFSE-rich, TE-poor domains, where clinopyroxene mantles + rims ($Mg\#_{75-78}$) developed at the late stage of magma mixing-hybridization. The abrupt decrease of averaged Sr/Yb ratio from 89 (recharge bands) to 42

(mantles + rims) and the strong negative Eu anomaly (Fig. 8) confirm that most of the evolutionary path is controlled by incipient plagioclase crystallization (De Astis et al., 2013; Nicotra et al., 2018). In view of this magma compositional shift, the concentration of Zr markedly increases up to 52 ppm in clinopyroxene mantles + rims, whereas the Cr/Yb ratio reaches a minimum of 0.5 (Fig. 8). It is also interesting to note that clinopyroxene mantles + rims from trachytes and rhyolites appear less differentiated than expected for silicic magmas, mostly showing major and trace element contents similar to the crystal cargo of basaltic and shoshonitic products (Fig. 8). This compositional observation matches with the numerous recharge bands enclosed within clinopyroxenes from trachytes and rhyolites (Table 1), attesting to continuous replenishment of the shallow plumbing system and consequent magma hybridization within the crystal mush (e.g., Forni et al., 2016).

Type 5 sector-zoned clinopyroxene phenocrysts are sporadically found in shoshonites and latites (Figs. 2 and 3). Si-Mg-rich hourglass forms {-1 1 1} are depleted in REE (e.g., Ce = 14 ± 1.2 and Yb = 1 ± 0.01 ppm on average) and HFSE (e.g., Hf = 1 ± 0.01 ppm and Zr = 19 ± 1.3 ppm on average) relative to Al-Fe-rich prism forms {*h k* 0} (e.g., Ce = 31 ± 3.1 ppm, Yb = 3 ± 0.02 ppm, Zr = 36 ± 3.4 ppm, and Hf = 2 ± 0.02 ppm on average). The intracrystalline distribution of major cations among the different sectors agrees with that observed for sector-zoned augites at Mt. Etna (Downes, 1974; Ubide et al., 2019a) and Stromboli (Ubide el al., 2019b). Sectoral partitioning of REE and HFSE cations is strictly controlled by both charge-balanced and -imbalanced configurations taking place in the structural sites of {-1 1 1} and {*h k* 0} sectors as the number of Al cations in tetrahedral coordination increases (Ubide et al., 2019a). The magnitude of sectoral partitioning at Vulcano Island is very similar to that measured at Stromboli, whereas the compositional difference between {-1 1 1} and {*h k* 0} sectors is much more marked for the clinopyroxene populations at Mt. Etna. For example, the $Al_2O_{3\{-1\ 1\ 1\}}/Al_2O_{3\{h\ k\ 0\}}$ ratios in phenocrysts at Vulcano Island, Stromboli, and Mt. Etna are on

the order of 0.88, 0.81, and 0.58, respectively. According to literature, the differential partitioning of cations between {-1 1 1} and {*h k* 0} faces is proportional to the degree of undercooling that, in turn, governs the growth of clinopyroxene under different magmatic conditions (Kouchi et al. 1983; Welsch et al., 2016; Ubide el al., 2019b; Giuliani et al., 2020; Masotta et al., 2020). Ubide el al. (2019b) compared the stronger sector zonation of clinopyroxenes from Mt. Etna with the weaker sector zonation of crystals from Stromboli. The authors concluded that the slow growth of clinopyroxene at Stromboli was generated by magmas undergoing very low degrees of undercooling comprised between 10 and 20 °C. Building on constraints from clinopyroxene growth experiments carried out by Kouchi et al. (1983), we observe that $Al_2O_{3\{-1\ 1\ 1\}}/Al_2O_{3\{h\ k\ 0\}}$ ratios for phenocrysts from Vulcano Island and Stromboli are generated by a degree of undercooling of ~13 °C. On the other hand, Masotta et al. (2020) have experimentally documented that sectoral partitioning of natural phenocrysts from Mt. Etna is caused by higher degrees of undercooling, mostly comprised between 23 and 32 °C. In this regard, magma dynamics driving the eruption of shoshonites-latites at Vulcano Island can be interpreted as the effect of sluggish crystallization kinetics under growth-dominated regimes during very slow magma ascents (Ubide el al., 2019b). It is also plausible that sector-zoned clinopyroxenes originated by small-scale convective transport of crystals through thermally heterogeneous magma reservoirs (cf. Welsch et al., 2009) that are located within the plumbing system at ~10-17 km of depth (De Astis et al., 2013; Palummo et al., 2020).

5.2. Timescales record of pre-eruptive processes

As discussed above, high-Mg# and Cr_2O_3-rich recharge bands of Type 3 clinopyroxene phenocrysts (Figs. 2 and 3) indicate crystallization from 1) a high-*T*, mafic magma that is recorded by the recharge band and 2) a low-*T*, resident magma which is homogenized by

mixing and hybridization after the mafic injection. Fe-Mg compositional zoning profiles in clinopyroxene phenocrysts have been examined to quantify the crystal residence time (Δt) via elemental diffusion chronometry using the NIDIS (Non-Isothermal Diffusion Incremental Step) model of Petrone et al. (2016). BSE microphotographs and greyscale profiles are used as proxies for Fe-Mg compositional zoning boundary layers along transects normal to the recharge band-rim interface (see Supplementary Material 2). The crystallization temperatures of clinopyroxene recharge bands and rims in equilibrium with different melt components have been calculated by using thermobarometric models based on exchange equilibria (cf. Palummo et al., 2020; see also temperature histograms in Supplementary Material 1): 1) 1,200-1,220 °C (high-Mg# recharge band) and 1,190-1,200 °C (low-Mg# rim) for basalts, 2) 1,130-1,180 °C (high-Mg# recharge band) and 1,100-1,160 °C (low-Mg# rim) for shoshonites, latites, and trachytes, and 3) 1,090-1,100 °C (high-Mg# recharge band) and 1,080-1,090 °C (low-Mg# rim) for rhyolites. The error of estimate has been minimized by probability density function analysis and corresponds to ±15 °C. We adapted the NIDIS model to evaluate the diffusive timescale (Δt) in the low-T resident magma (i.e., recharge band-rim interface) which represents the time spent in the last magmatic environment prior to eruption (Petrone et al., 2016).

Smoother recharge band-rim profiles are generally observed in clinopyroxenes from silicic rocks, in agreement with longer temporal intervals after mafic injection in the reservoir and prior to eruption (Fig. 9a). Conversely, steeper diffusion profiles are measured for recharge band-rim boundaries analyzed in clinopyroxene phenocrysts from more primitive products, as the result of diffusive re-equilibration of compositional zoning for shorter time periods (Fig. 9a). All timescales are summarized in Fig. 9b. Shorter timescales of ~0.1-9 years are quantified for clinopyroxenes from basalts, shoshonites, and latites, whereas longer timescales on the order of ~7-18 years and ~16-44 years are calculated for clinopyroxenes from trachytes and rhyolites, respectively (Fig. 9b). The longer crystal residence times measured for the more

differentiated eruptive products are in agreement with the general increase over time of the degree of chemical evolution of magmas and the enrichment in incompatible trace elements (e.g., De Astis et al., 2013). This time-related compositional shift from basalts to rhyolites is also confirmed by the geochemical evolution of clinopyroxene core from Eruptive Epoch 5 to 8 (Fig. 6).

Mixing phenomena between high-*T* mafic and low-*T* felsic end-members are intimately related to magma dynamics recorded by the recurrent concentric zonation and dissolution texture of clinopyroxene phenocrysts, which tend to be slightly more abundant in trachyte and rhyolite (Figs. 2 and 3; Table 1). More silicic trachytes and rhyolites represent residual melts trapped-extracted from crystal mushes that are approximatively located between 5 and 10 km depth (Palummo et al., 2020). The most favorable window for crystal-melt separation occurs at a crystallinity of ~50–70% (Dufek and Bachmann, 2010), such that eruptible silicic melts can be extracted from the crystal mush, without bulk melting or remobilization of its crystalline framework (Stelten et al., 2015). Coherently, the differentiation of basalts to trachytes at Vulcano Island takes place at crystal content of ~52%, whereas the formation of highly differentiated trachytes and rhyolitic melts requires a mush system with crystallinity comprised between 59% and 84% (Palummo et al., 2020).

The compositional similarity between clinopyroxene cores and mantles + rims from trachytes and rhyolites (compare Figs. 6 and 8) suggests mutual crystallization in a colder and shallower mush region over prolonged crystal residence times (Fig. 9). The great number of recharge bands observed in silicic products, alongside resorbed cores and mottled crystals (Table 1) indicates that phenocrysts remained trapped in the mush for a prolonged period of time, thereby recording sustained injections of less differentiated magmas. Longer diffusion timescales are typically measured for phenocrysts hosted in silicic melts extracted from crystal-rich regions (Cooper, 2019). By interpolating 1) the empirical viscosity equation of Giordano

et al. (2008), 2) the bulk rock analyses of products erupted at Vulcano Island (Fig. 1a), and 3) the *P*-*T*-H_2O crystallization paths of clinopyroxene-bearing magmas (Palummo et al., 2020), we found that the geochemical evolution of clinopyroxene is accompanied by an average melt viscosity increase, on the order of ~1.2 (basalt), ~2.3 (shoshonite), ~2.5 (latite), ~3.8 (trachyte), ~4.6 (rhyolite) log Pa s. In the lower crust, low viscosity basaltic magmas remain above the solidus state due to the effect of high temperature conditions. These thermal and rheological regimes allow extensive magma segregation and migration. During ascent, however, basaltic magmas cool and crystallize to develop more differentiated melts leading to the growth of clinopyroxene phenocrysts progressively more enriched in REE and HFSE (Figs. 5 and 6). In the uppermost crust, the formation of non-eruptible crystal-rich mush regions takes place by strong cooling-induced crystallization phenomena and high viscosity rhyolitic lenses develop by percolative melt transfer (Bachmann and Bergantz, 2004; Dufek and Bachmann, 2010; Masotta et al., 2016). Protracted residence times recorded by clinopyroxene phenocrysts (Fig. 9) are consistent with the tendency for phenocrysts to remain suspended in more silicic melts with a higher viscosity, as the temperature of the solidifying system decreases and the degree of crystallization increases (e.g., Hawkesworth et al., 2000 and references therein). As outlined by thermobarometric constraints (Fig. 7), after extraction of melt from the crystal mush, small-volume rhyolitic magmas stall temporarily at very shallower levels of the reservoir. Therefore, resorbed cores (Type 2), recharge bands (Type 3), and mottled resorption textures (Type 4) found in clinopyroxene phenocrysts (Figs. 2 and 3) may be also interpreted as the result of mixing between low-*T* rhyolitic magmas extracted from the crystal-rich region and fresh inputs of high-*T* free magmas rising from shoshonitic and latitic reservoirs located at moderate depths of 10-17 km (De Astis et al., 2013; Palummo et al., 2020).

5.3. Modeling magma recharge and mixing dynamics

Cr/Yb ratios measured for clinopyroxene cores, recharge bands, and mantles + rims are comparatively plotted in Fig. 10a in order to place constrain on the recharge processes and mixing dynamics governing the evolutionary history of magmas at Vulcano Island. An important aspect emerging from this comparison is the compositional diversity of clinopyroxene, characterized by decreasing Cr/Yb ratios as the geochemical evolution of magma proceeds from basalt to rhyolite (Fig. 10a). Differently from the more homogeneous chemistry of basalts erupted during the Eruptive Epoch 5, younger rhyolitic melts from Eruptive Epoch 8 were dominated by abundant crystallization of felsic minerals plus low degrees of crustal assimilation (Bullock et al., 2019; De Astis et al., 1997, 2000, 2003; Gioncada et at., 2003; Peccerillo et al., 2006). Clinopyroxene zoning patterns with highly variable Cr/Yb ratios reflect substantial chemical modifications in more silicic reservoirs due to open-system processes associated with the input of fresh magma into distinct crustal regions and related mixing and hybridization phenomena (Forni et al., 2016; Gioncada et al., 1998; Nicotra et al., 2018; Peccerillo et al., 2006; Piochi et al., 2009). Moreover, Cr/Yb ratios in clinopyroxene decrease with the sequential growth of phenocryst, from core to mantle + rim (Fig. 10a). This change validates the idea that magma mixing was likely accompanied by cooling-degassing processes, especially during the storage of magma in shallower and colder crustal regions (Mandarano et al., 2016), where the most evolved chemistry of clinopyroxene rims reflects the latest residual melt composition, immediately preceding the eruption.

With the only exception represented by the diopsidic clinopyroxene cores from basalts, there is always some degree of overlap between the trace element inventory of clinopyroxene cores, recharge bands, and mantle + rims (Fig. 10a). As schematically illustrated in Fig. 10b, the compositional heterogeneity of clinopyroxene results from the transfer of magma between different storage regions that are interconnected with each other (cf. Palummo et al., 2020).

The isolated compositional group of clinopyroxene cores from basalts with extremely high Cr/Yb ratios (Fig. 10a) represent early crystal-melt equilibration in the lower crust (Fig. 10b). Conversely, the Cr/Yb ratio in clinopyroxene cores from shoshonites to rhyolites progressively decreases (Fig. 10a), in accord with the formation of more differentiated reservoirs that, however, explore continuous physico-chemical changes due to interaction between compositionally distinct magma batches (Fig. 10b).

Recharge bands in clinopyroxene phenocrysts from basalts show Cr/Yb ratios that are intermediate between those measured for clinopyroxene cores from shoshonites + latites and trachytes + rhyolites (Fig. 10a). This suggests that an early-formed crystal cargo residing in the deeper parts of the crust was remobilized and transported by mafic melts (e.g., Petrone et al., 2018; Cooper, 2019) passing through an interconnected series of differentiated magma storage regions (Fig. 10b). In a similar fashion, the occurrence of Type 4 mottled phenocrysts (i.e., aggregates of partially dissolved clinopyroxenes; Fig, 2) suggests that crystals were assembled from different parts of the crust (Fig. 10b), in agreement with analogous dynamic processes documented for clinopyroxenes erupted at Mt. Etna (Armienti et al., 2007) and Stromboli (Di Stefano et al., 2020). In this scenario, intracrystalline heterogeneities indicate a multi-stage history of magma that is characterized by mixing and hybridization phenomena operating within an articulated plumbing system (Fig. 10b), where recharge inputs encounter partially or wholly crystallized reservoirs generated by different prior magma batches. The broad compositional interval recorded by recharge bands from rhyolites (Fig. 10a) testifies to multiple inputs of mafic magma from depth, abundant cooling-induced crystallization, and protracted crystal residence times in a highly crystalline storage region.

The bulk (crystal + melt) chemical evolution of magmas points towards a unified view of cogenetic differentiation processes operating in two main magma storage regions within the crust (cf. Bachmann and Huber, 2016). The first storage region is located in lower crust near

the crust-mantle boundary and is fed by primitive basalts that represent the most mafic endmembers of the differentiation series (Fig. 10b). A high-pressure crystallization assemblage develops within this lower crustal storage region (see for example Ozdemir et al., 2011). The second main storage region is located at shallower depths in the upper crust (typically between 250 and 150 MPa; see Huber et al., 2019), where magmas pond at the apex of a series of interconnected magma transfer zones (Fig. 10b). Magma dynamics at Vulcano Island are controlled by the interplay between lower and upper crust storage regions and only transient magma bodies are generated at intermediate depths (Fig. 10b), partly by mixing of magmas from these two main storage regions (Bachmann and Huber, 2016; Huber et al., 2019).

To better elucidate the clinopyroxene-related geochemical changes characterizing the eruptive history of Vulcano Island, we have investigated the evolutionary path of LREE (i.e., La) and HREE (i.e., Yb) in magmas through the partitioning model of Mollo et al. (2018, 2020b). Different equations describing the excess of strain energy (Wood and Blundy, 1997) and electrostatic energy (Wood and Blundy, 2001) are integrated in this model, in order to calculate the partitioning energetics controlling heterovalent REE cation substitutions in clinopyroxene. This makes it possible to quantify the role of clinopyroxene crystallization on the REE pattern of a magma through the estimate of a different clinopyroxene-melt partition coefficient (i.e., $D_{REE} = {}^{cpx}REE / {}^{melt}REE$ on a weight basis) for each stage of crystallization. The *P*-*T*-H_2O saturation conditions of clinopyroxene phenocrysts (i.e., *P* = 20-750 MPa, *T* = 1,000-1,220 °C, and H_2O = 1.6-4.0 wt.%) that are required as input data for the partitioning modeling come from the petrological work of Palummo et al. (2020). REE cations were chosen for the modeling because of 1) the diverse but systematic zoning patterns in clinopyroxene phenocrysts, 2) the complete thermodynamic description of partitioning behavior as a function of intensive-extensive parameters, and 3) the preferential control of clinopyroxene crystallization on REE contents in the residual melt relative to other mineral phases (i.e.,

according to the relation between mineral weight fractions and the bulk partition coefficient; Mollo et al., 2018, 2020b). A spectrum of partition coefficients has been determined for clinopyroxene cores and recharge bands (Supplementary Material 1). Recalling the free energy exchange of the fusion reaction $^{cpx}REEMgSiO_2O_6 \leftrightarrow {}^{melt}REEMgSiO_2O_6$ (Wood and Blundy, 1997), the estimated values of D_{La} and D_{Yb} were used to invert the concentrations of REE in the melts from clinopyroxene cores and recharge bands (i.e., $^{melt}REE = {}^{cpx}REE / D_{REE}$).

Results from calculations are plotted in Fig. 10c and compared with the bulk rock analyses of the eruptive products. Different compositional vectors (i.e., colored arrows in Fig. 10c) represent the putative REE contents of end-member magmas in equilibrium with the more homogeneous clinopyroxene cores, as calculated by the partitioning equations of Mollo et al. (2018, 2020b). These vectors are almost aligned along a common differentiation path involving the progressive increase of La-Yb contents from basalt to rhyolite. The La-Yb array resulting from partitioning modeling is divided in three distinct groups for basalts, shoshonites + latites, and trachytes + rhyolites (Fig. 10c) that roughly reflect the plumbing system architecture of Vulcano Island (Fig. 10b). The grey dashed symbols represent the putative REE contents of magmatic injections recorded by the more heterogeneous recharge bands (Fig. 10c). While most of recharge bands from basalts converge in a narrow range that is close to the compositional vector, recharge bands from trachytes and rhyolites show the largest compositional variability. This implies that the number of recharge bands and their chemical diversity axiomatically increase with increasing the silicic character of magma, thereby depicting a fan-like array indicative of open-system processes (Fig. 10c). Importantly, our modelled data set reproduce very well the bulk rock analyses of natural eruptions and their fan-like pattern (Fig. 10c). This correspondence reflects a plumbing system evolution that is persistently controlled by crystal-melt dynamics due to the interaction between different

crystallizing reservoirs in which the supply of fresh magma modulates the final texture and composition of the erupted product.

We conclude that the lower crust is the most favorable location for the origin of compositionally homogeneous basaltic magmas (i.e., melt-dominated domains) and their initial stages of crystallization during transfer at intermediate depths (Fig. 10b). However, magma percolation and accumulation in the upper crustal regions lead to the formation of an interconnected series of magmatic reservoirs (i.e., crystal-dominated domains), many of which may be composed of crystal-rich mush systems (Fig. 10b). According to this conceptual model, the physical (e.g., crystallinity and melt viscosity) and chemical (e.g., degree of evolution of crystals and melts) state of magma changes dramatically in the shallowest parts of the feeding system. The discrete populations, complex compositional zoning patterns, and different residence times of clinopyroxene phenocrysts reflect the intricate crystallization history of magma. The mineral assemblage in silicic mush melts is sufficiently resilient to record numerous mafic injections and high degrees of magma mixing, hybridization, and crystallization before eruption. Taken together, the textural and compositional changes of clinopyroxene phenocrysts present a picture of a plumbing system that extends through the crust and is characterized by distributions of melts and crystals which are progressively more evolved and heterogeneous in both space and time (Fig. 10b).

6. Concluding remarks

This study illustrates the textural and compositional changes of clinopyroxene phenocrysts from basaltic to rhyolitic products erupted at Vulcano Island over a period of time from ~54 ka to 1739 CE. Phenocrysts have been categorized on the presence or absence of complex zoning patters and five distinct populations have been recognized (i.e., Type 1 homogeneous crystals,

Type 2 core/resorbed cores, Type 3 recharge bands, Type 4 mottled crystals, and Type 5 sector-zoned crystals). The different growth features and intracrystalline distributions of major and trace cations in clinopyroxene closely reflect the physico-chemical changes of magma under the effects of closed- and open-system processes. By combining microanalytical data and trace element modeling, we gained useful insights into the plumbing system architecture and the intricate magmatic history of Vulcano Island. According to this approach, the following conclusions can be drawn:

1) the compositional evolution of clinopyroxene highlights that basaltic magmas are characterized by Types 1 and 2 populations, in which diopsidic cores are heralds of crystallization in the lower crust. The compositional change of clinopyroxene proceeds from diopside-augite to augite, following the polybaric-polythermal differentiation of basalts towards more differentiated melts residing in the upper crust;
2) the number of chemical heterogeneities in clinopyroxene increases in silicic eruptive products, in accord with the more frequent observation of Types 3 and 4 populations in trachytes and rhyolites. This chemical diversity reflects an open-system behavior due to injection of hotter and more primitive magmas into compositionally distinct colder and shallower reservoirs. Open-system processes are testified by multi-stage clinopyroxene dissolution phenomena that results from thermal and/or chemical disequilibrium with the recharge melt;
3) Type 5 sector-zoned crystals are typically found in shoshonites and latites. The weak sector zonation between {-1 1 1} hourglass and {h k 0} basal prism forms suggests sluggish crystallization kinetics during very slow magma ascents and/or small-scale convective transport of crystals through thermally heterogeneous magma reservoirs;
4) shorter timescales (~0.1-9 years) are quantified for clinopyroxenes from basaltic, shoshonitic, and latitic magmas, whereas longer timescales are measured for

phenocrysts crystallizing in trachytic (~7-18 years) and rhyolitic (~16-44 years) reservoirs. Protracted residence times are consistent with the tendency for clinopyroxene to remain suspended in more silicic and viscous melts extracted from shallow crystal-rich regions;

5) results from partitioning modeling based on the concentrations of rare earth elements (REE) in clinopyroxene confirm the cogenetic origin for the eruptive products along a common differentiation path. Magma percolation and accumulation in the upper crustal regions lead to the formation of an interconnected series of magmatic reservoirs with different degrees of REE concentrations. Both the compositional diversity of melt and the intracrystalline heterogeneity of clinopyroxene are exacerbated in crystal-dominated mush zones, responding to the stronger diversification of REE via intense magma mixing, hybridization, and crystallization phenomena.

References

Armienti, P., Francalanci, L., Landi, P., 2007. Textural effects of steady state behavior of the Stromboli feeding system. J. Volcanol. Geotherm. Res. 160, 86-98.

Bachmann, O., Huber, C., 2016. Silicic magma reservoirs in the Earth's crust: American Mineralogist, v. 101, p. 2377-2404.

Bachmann, O., Bergantz, G.W., 2004. On the origin of crystal-poor rhyolites: extracted from batholithic crystal mushes. J. Petrol. 45 (8), 1565-1582.

Beard, C.D., van Hinsberg, V.J., Stix, J., Wilke, M., 2019. Clinopyroxene/melt trace element partitioning in sodic alkaline magmas. J. Petrol. 60, 1797-1823. https://doi.org/10.1093/petrology/egz052.

Bergantz, G.W., Schleicher, J.M., Burgisser, A., 2015. Open-system dynamics and mixing in magma mushes. Nature Geoscience, 8(10), 793-796.

Blundy, J. D., Falloon, T. J., Wood, B. J., Dalton, J. A., 1995. Sodium partitioning between clinopyroxene and silicate melts. J. Geophys. Res. Solid Earth, 100, 15501-15515.

Bullock, L.A., Gertisser, R., O'Driscoll, B., Harland, S., 2019. Magmatic evolution and textural development of the 1739 CE Pietre Cotte lava flow, Vulcano, Italy. J. Volcanol. Geoth. Res. 372, 1-23.

Cashman, K.V., Sparks, R.S.J., Blundy, J.D., 2017. Vertically extensive and unstable crystals mushes: a unifying view of igneous processes associated with volcanoes. Science 355 (6331) eaag3055.

Clocchiatti, R., Del Moro, A., Gioncada, A., Joron, J.L., Mosbah, M., Pinarelli, L., Sbrana, A., 1994. Assessment of a shallow magmatic system: the 1888-90 eruption, Vulcano Island, Italy. Bull. Volcanol. 56, 466-486.

Cooper, K.M., 2019. Time scales and temperatures of crystal storage in magma reservoirs: Implications for magma reservoir dynamics. Philosophical Transactions of the Royal Society A, 377(2139), 20180009.

Costa, S., Masotta, M., Gioncada, A., Pistolesi, M., Bosch, D., Scarlato, P., 2020. Magma evolution at La Fossa volcano (Vulcano Island, Italy) in the last 1000 years: evidence from eruptive products and temperature gradient experiments. Contrib. Mineral. Petrol. 175 (4), 1-22.

Costa, S.; Masotta, M.; Gioncada, A.; Pistolesi, M. A Crystal Mush Perspective Explains Magma Variability at La Fossa Volcano (Vulcano, Italy). Minerals, 2021, 11, 1094. https://doi.org/10.3390/min11101094

Davì, M., De Rosa, R., Donato, P., Vetere, F., Barca, D., Cavallo, A., 2009. Magmatic evolution and plumbing system of ring-fault volcanism: the Vulcanello peninsula (Aeolian Islands, Italy). Eur. J. Mineral. 21, 1009-1028.

De Astis, G., La Volpe, L., Peccerillo, A., Civetta, L., 1997. Volcanological and petrological evolution of Vulcano Island (Aeolian Arc, southern Tyrrhenian Sea). J. Geophys. Res. 102, 8021-8050.

De Astis, G., Peccerillo, A., Kempton, P.D., La Volpe, L., Wu, T.W., 2000. Transition from calc-alkaline to potassium-rich magmatism in subduction environments: geochemical and Sr, Nd, Pb isotopic constraints from the island of Vulcano (Aeolian arc). Contrib. Mineral. Petrol. 139, 684-703.

De Astis, G., Ventura, G., Vilardo, G., 2003. Geodynamic significance of the Aeolian volcanism (Southern Tyrrhenian Sea, Italy) in light of structural, seismological, and geochemical data. Tectonics 22, 1040-1057.

De Astis, G., Lucchi, F., Dellino, P., La Volpe, L., Tranne, C.A., Frezzotti, M.L., Peccerillo, A., 2013. Geology, volcanic history and petrology of Vulcano (central Aeolian archipelago). In: Lucchi, F., Peccerillo, A., Keller, J., Tranne, C.A., Rossi, P.L. (Eds.), The Aeolian Islands Volcanoes. Geological Society, London, Memoirs vol. 37, 181-349.

Dellino, P., De Astis, G., La Volpe, L., Mele, D., Sulpizio, R., 2011. Quantitative hazard assessment of phreatomagmatic eruptions at Vulcano (Aeolian Islands, Southern Italy), as obtained by combining stratigraphy, event statistics and physical modelling. J. Volcanol. Geotherm. Res. 201, 364-384.

Di Stefano, F., Mollo, S., Ubide, T., Petrone, C. M., Caulfield, J., Scarlato, P., Nazzari, M., Andronico, D., Del Bello, E., 2020. Mush cannibalism and disruption recorded by

clinopyroxene phenocrysts at Stromboli volcano: New insights from recent 2003–2017 activity. Lithos, 360, 105440.

Downes, M.J., 1974. Sector and oscillatory zoning in calcic augites from M. Etna, Sicily. Contrib. Mineral. Petrol. 47, 187-196.

Druitt, T.H., Costa, F., Deloule, E., Dungan, M., Scaillet, B., 2012. Decadal to monthly timescales of magma transfer and reservoir growth at a caldera volcano. Nature 482, 77-80.

Dufek, J., Bachmann, O., 2010. Quantum magmatism: Magmatic compositional gaps generated by melt-crystal dynamics. Geology 38 (8), 687-690.

Dunworth, E., Neumann, E.R., Rosenbaum, J., 2001. The Skien lavas, Oslo Rift: petrological disequilibrium and geochemical evolution. Contributions to Mineralogy and Petrology, 140(6), 701-719.

Ellam, R.M., Menzies, M.A., Hawkesworth, C.J., Leeman, W.P., Rosi, M., Serri, G., 1988. The transition from calc-alkaline to potassic orogenic magmatism in the Aeolian Islands, Southern Italy. Bulletin of Volcanology, 50, 386-398.

Forni, F., Ellis, B.S., Bachmann, O., Lucchi, F., Tranne, C.A., Agostini, S., Dallai, L., 2015. Erupted cumulate fragments in rhyolites from Lipari (Aeolian Islands). Contrib. Mineral. Petrol. 170, 49.

Forni, F., Bachmann, O., Mollo, S., De Astis, G., Gelman, S.E., Ellis, B.S., 2016. The origin of a zoned ignimbrite: Insights into the Campanian Ignimbrite magma chamber (Campi Flegrei, Italy), Earth and Planetary Science Letters, 449, 259-271. http://dx.doi.org/10.1016/j.epsl.2016.06.003.

Forni, F., Degruyter, W., Bachmann, O., De Astis, G., Mollo, S., 2018. Long-term magmatic evolution reveals the beginning of a new caldera cycle at Campi Flegrei. Science Advances 4 (11), eaat9401. http://dx.doi.org/10.1126/sciadv.aat9401.

Gioncada, A., Clocchiatti, R., Sbrana, A., Bottazzi, P., Massare, D., Ottolini, L., 1998. A study of melt inclusions at Vulcano (Aeolian Islands, Italy): insights on the primitive magmas and on the volcanic feeding system. Bull. Volcanol. 60, 286-306.

Gioncada, A., Mazzuoli, R., Bisson, M., Pareschi, M.T., 2003. Petrology of volcanic products younger than 42 ka on the Lipari-Vulcano complex (Aeolian Islands, Italy): an example of volcanism controlled by tectonics. J. Volcanol. Geotherm. Res. 122, 191-220.

Gioncada, A., Mazzuoli, R., Milton, A.J., 2005. Magma mixing at Lipari (Aeolian Islands, Italy): insights from textural and compositional features of phenocrysts. Journal of Volcanology and Geothermal Research, 145(1-2), 97-118.

Giordano, D., Russell, J.K., Dingwell, D.B., 2008. Viscosity of magmatic liquids: a model. Earth and Planetary Science Letters, 271(1-4), 123-134.

Giuliani, L., Iezzi, G., Mollo, S., 2020, Dynamics of volcanic systems: physical and chemical models applied to equilibrium versus disequilibrium solidification of magmas, p.101-132, in Vetere F. eds., Dynamic Magma Evolution, Geophysical Monograph Series 254, 206 pp., ISBN: 9781119521136, John Wiley & Sons Inc., New Jersey, USA. https://doi.org/10.1002/9781119521143.ch5.

Hawkesworth, C.J., Blake, S., Evans, P., Hughes, R., Macdonald, R., Thomas, L.E., Turner, S.P., Zellmer, G., 2000. Time scales of crystal fractionation in magma chambers-integrating physical, isotopic and geochemical perspectives. Journal of Petrology, 41(7), 991-1006.

Huber, C., Townsend, M., Degruyter, W., Bachmann O., 2019. Optimal depth of subvolcanic magma chamber growth controlled by volatiles and crust rheology. Nature Geoscience 12, 762–768.

Kamenetsky, V., Clocchiatti, R., 1996. Primitive magmatism of Mt. Etna: insights from mineralogy and melt inclusions. Earth Planet. Sci. Lett. 142 (3-4), 553-572.

Keller, J., 1980. The island of Vulcano. Rendiconti della Società Italiana di Mineralogia e Petrografia 3 (6), 369-414.

Kent, A.J.R., Darr, C., Koleszar, A. M., Salisbury, M.J., Cooper, K.M., 2010. Preferential eruption of andesitic magmas through recharge filtering. Nat. Geosci. 3, 631-636.

Kouchi, A., Sugawara, Y., Kashima, K., Sunagawa, I., 1983. Laboratory growth of sector zoned clinopyroxenes in the system CaMgSi2O6-CaTiAl2O6. Contributions to Mineralogy and Petrology, 83(1-2), 177-184.

Lanzafame, G., Mollo, S., Iezzi, G., Ferlito, C., Ventura, G., 2013. Unraveling the solidification path of a pahoehoe “cicirara” lava from Mount Etna volcano. Bulletin of Volcanology, 75(4), 1-16.

Le Bas, M.J., Le Maitre, R.W., Streckeisen, A., Zanettin, B., 1986. A chemical classification of volcanic rocks based on the total alkali-silica diagram. J. Petrol. 27 (3), 745-750.

Mandarano, M., Paonita, A., Martelli, M., Viccaro, M., Nicotra, E., Millar, I.L., 2016. Revealing magma degassing below closed-conduit active volcanoes: Geochemical features of volcanic rocks versus fumarolic fluids at Vulcano (Aeolian Islands, Italy). Lithos 248-251, 272-287.

Mangler, M., Petrone, C.M., Hill, S., Delgado-Granados, H., Prytulak, J., 2020. A pyroxenic view on magma hybridisation and crystallisation at Popocatépetl Volcano, Mexico. Frontiers Earth Sciences 8:362, doi: 10.3389/feart.2020.00362.

Masotta, M., Mollo, S., Freda, C., Gaeta, M., Moore, G., 2013. Clinopyroxene-liquid thermometers and barometers specific to alkaline differentiated magmas. Contrib. Mineral. Petrol. 166, 1545-1561.

Masotta, M., Mollo, S., Gaeta, M., Freda, C., 2016, Melt extraction in mush zones: The case of crystal-rich enclaves at the Sabatini Volcanic District (central Italy), Lithos, 248-251, 288-292. http://dx.doi.org/10.1016/j.lithos.2016.01.030.

Masotta, M., Pontesilli, A., Mollo, S., Armienti, P., Ubide, T., Nazzari, M., Scarlato, P., 2020. The role of undercooling during clinopyroxene growth in trachybasaltic magmas: Insights on magma decompression and cooling at Mt. Etna volcano. Geochimica et Cosmochimica Acta, 268, 258-276. https://doi.org/10.1016/j.gca.2019.10.009.

Mollo S., Putirka K., Misiti V., Soligo M., Scarlato P., 2013. A new test for equilibrium based on clinopyroxene-melt pairs: Clues on the solidification temperatures of Etnean alkaline melts at post-eruptive conditions. Chemical Geology, 352, 92-100, doi: 10.1016/j.chemgeo.2013.05.026.

Mollo S., Masotta M., 2014, Optimizing pre-eruptive temperature estimates in thermally and chemically zoned magma chambers, Chemical Geology, 368, 97-103. https://doi.org/10.1016/j.chemgeo.2014.01.007.

Mollo, S., Giacomoni, P.P., Coltorti, M., Ferlito, C., Iezzi, G., Scarlato, P., 2015. Reconstruction of magmatic variables governing recent Etnean eruptions: constraints from mineral chemistry and P-T-fO2-H2O modelling. Lithos 212-215, 311-320.

Mollo, S., Blundy, J., Scarlato, P., De Cristofaro, S.P., Tecchiato, V., Di Stefano, F., Vetere, F., Holtz, F., Bachmann, O., 2018. An integrated P-T-H2O-lattice strain model to quantify the role of clinopyroxene fractionation on REE+Y and HFSE patterns of mafic alkaline magmas: Application to eruptions at Mt. Etna. Earth Sci. Rev. 185, 32-56. https://doi.org/10.1016/j.earscirev.2018.05.014.

Mollo S., Ubide T., Di Stefano F., Nazzari M., Scarlato P., 2020a. Polybaric/polythermal magma transport and trace element partitioning recorded in single crystals: A case study of a zoned clinopyroxene from Mt. Etna. Lithos 356-357, 105382. https://doi.org/10.1016/j.lithos.2020.105382.

Mollo, S., Blundy, J., Scarlato, P., Vetere F., Holtz, F, Bachmann, O., Gaeta, M., 2020b. A review of the lattice strain and electrostatic effects on trace element partitioning between clinopyroxene and melt: Applications to magmatic systems saturated with Tschermak-rich clinopyroxenes. Earth-Science Reviews, 210, 103351. https://doi.org/10.1016/j.earscirev.2020.103351.

Nicotra, E., Giuffrida, M., Viccaro, M., Donato, P., D'Oriano, C., Paonita, A., De Rosa, R., 2018. Timescales of pre-eruptive magmatic processes at Vulcano (Aeolian Islands, Italy) during the last 1000 years. Lithos 316-317, 347-365.

Özdemir, Y., Blundy, J., Güleç, N., 2011. The importance of fractional crystallization and magma mixing in controlling chemical differentiation at Süphan stratovolcano, eastern Anatolia, Turkey. Contrib Mineral Petrol 162, 573–597. https://doi.org/10.1007/s00410-011-0613-8

Palummo, F., Mollo, S., De Astis, G., Di Stefano, F., Nazzari, M., Scarlato, P., 2020. Petrological and geochemical modeling of magmas erupted at Vulcano Island in the

period 54-8 ka: Quantitative constraints on the sub-volcanic architecture of the plumbing system. Lithos, 374, 105715.

Peccerillo, A., Frezzotti, M.L., De Astis, G., Ventura, G., 2006. Modeling the magma plumbing system of Vulcano (Aeolian Islands, Italy) by integrated fluid-inclusion geobarometry, petrology, and geophysics. Geology 34 (1), 17-20.

Perinelli, C., Mollo, S., Gaeta, M., De Cristofaro, S.P., Palladino, D.M., Armienti, P., Scarlato, P., Putirka, K.D., 2016. An improved clinopyroxene-based hygrometer for Etnean magmas and implications for eruption triggering mechanisms. Am. Mineral. 101, 2774-2777.

Petrone, C.M., Bugatti, G., Braschi, E., Tommasini, S., 2016. Pre-eruptive magmatic processes re-timed using a non-isothermal approach to magma chamber dynamics. Nat. Commun. 7, 12946.

Petrone, C.M., Braschi, E., Francalanci, L., Casalini, M., Tommasini, S., 2018. Rapid mixing and short storage timescale in the magma dynamics of a steady-state volcano. Earth Planet. Sci. Lett. 492, 206-221.

Piochi, M., De Astis, G., Petrelli, M., Ventura, G., Sulpizio, R., Zanetti, A., 2009. Constraining the recent plumbing system of Vulcano (Aeolian Arc, Italy) by textural, petrological, and fractal analysis: The 1739 A.D. Pietre Cotte lava flow. Geochem. Geophys. Geosyst. 10 (No Q01009).

Putirka, K.D., 2008. Thermometers and barometers for volcanic systems. Rev. Mineral. Geochem. 69, 61-120.

Sparks, R.S.J., Sigurdsson, H., Wilson, L., 1977. Magma mixing: a mechanism for triggering acid explosive eruptions. Nature 267, 315-318.

Stelten, M.E., Cooper, K.M., Vazquez, J.A., Calvert, A.T., Glessner, J.J., 2015. Mechanisms and timescales of generating eruptible rhyolitic magmas at Yellowstone caldera from zircon and sanidine geochronology and geochemistry. Journal of Petrology, 56(8), 1607-1642.

Sun, C.G., Liang, Y., 2012. Distribution of REE between clinopyroxene and basaltic melt along a mantle adiabat: effects of major element composition, water, and temperature. Contrib. Mineral. Petrol. 163, 807-823. https://doi.org/10.1007/S00410-011-0700-X.

Sun, C., Graff, M., Liang, Y., 2017. Trace element partitioning between plagioclase and silicate melt: the importance of temperature and plagioclase composition, with implications for terrestrial and lunar magmatism. Geochim. Cosmochim. Acta 206, 273-295.

Sun, S.S., McDonough, W.F., 1989. Chemical and isotopic systematics of ocean basalts: implications for mantle composition and processes. In: Saunders, A. D., Norry, M. J. (eds) Magmatism in the Ocean Basins. Geol. Soc. Lond. Spec. Publ. 42, 313-345.

Szymanowski, D., Ellis, B.S., Wotzlaw, J.F., Buret, Y., von Quadt, A., Peytcheva, I., Bindeman, I.N., Bachmann, O., 2016. Geochronological and isotopic records of crustal storage and assimilation in the Wolverine Creek-Conant Creek system, Heise eruptive centre, Snake River Plain. Contributions to Mineralogy and Petrology, 171(12), 1-15.

Tecchiato, V., Gaeta, M., Mollo, S., Scarlato, P., Bachmann, O., Perinelli, C., 2018. Petrological constraints on the high-Mg basalts from Capo Marargiu (Sardinia, Italy): Evidences of cryptic amphibole fractionation in polybaric environments, Journal of Volcanology and Geothermal Research, 349, 31-46. https://doi.org/10.1016/j.jvolgeores.2017.09.007.

Ubide, T., Kamber, B.S., 2018. Volcanic crystals as time capsules of eruption history. Nat. Commun. 9, 326.

Ubide, T., Mollo, S., Zhao, J.-X., Nazzari, M., Scarlato, P., 2019a. Sector-zoned clinopyroxene as a recorder of magma history, eruption triggers, and ascent rates. Geochimica et Cosmochimica Acta, 251, 265-283. https://doi.org/10.1016/j.gca.2019.02.021.

Ubide, T., Caulfield, J., Brandt, C., Bussweiler, Y., Mollo, S., Di Stefano, F., Nazzari, M., Scarlato, P., 2019b. Deep Magma Storage revealed by Multi-Method Elemental Mapping of Clinopyroxene Megacrysts at Stromboli Volcano. Frontiers in Earth Science, 7:239. https://doi.org/10.3389/feart.2019.00239.

Ventura, G., 2013. Kinematics of the Aeolian volcanism (Southern Tyrrhenian Sea) from geophysical and geological data. In: Lucchi, F., Peccerillo, A., Keller, J., Tranne, C.A., Rossi, P.L. (Eds.), The Aeolian Islands Volcanoes. Geological Society, London, Memoirs 37, 3-11.

Welsch, B., Hammer, J., Baronnet, A., Jacob, S., Hellebrand, E., Sinton, J., 2016. Clinopyroxene in postshield Haleakala ankaramite: 2. Texture, compositional zoning and supersaturation in the magma. Contrib. Mineral. Petrol. 171, 6. https://doi.org/10.1007/s00410-015-1213-9.

Welsch, B., Faure, F., Bachèlery, P., Famin, V., 2009. Microcrysts record transient convection at Piton de la Fournaise volcano (La Réunion hotspot). Journal of Petrology, 50(12), 2287-2305.

Wood, B.J., Blundy, J.D., 1997. A predictive model for rare earth element partitioning between clinopyroxene and anhydrous silicate melt. Contrib. Mineral. Petrol. 129, 166-181. https://doi.org/10.1007/s004100050330.

Wood, B.J., Blundy, J.D., 2001. The effect of cation charge on crystal–melt partitioning of trace elements. Earth Planet. Sci. Lett. 188, 59-71. https://doi.org/10.1016/S0012-821X(01)00294-1.

Zanon, V., Frezzotti, M.L., Peccerillo, A., 2003. Magmatic feeding system and crustal magma accumulation beneath Vulcano Island (Italy): evidence from fluid inclusion in quartz xenoliths. J. Geophys. Res. 108, 2298-2301.

Figure captions

Figure 1. Schematic map of Vulcano Island showing the locations of rock samples that are the subject of the present study (a). The map legend refers to Eruptive Epochs from 1 to 8, as reported in De Astis et al. (2013). Total alkali vs. silica (TAS) diagram after Le Bas et al. (1986) (b). The rock samples are classified as basalts, basaltic trachyandesites (shoshonites), trachyandesites (latites), trachytes, and rhyolites.

Figure 2. Back-scattered electron (BSE) photomicrographs showing the most important textural features of clinopyroxene phenocrysts: Type 1 homogeneous crystals, Type 2 core/resorbed cores, Type 3 recharge bands, Type 4 mottled crystals, and Type 5 sector-zoned crystals.

Figure 3. Electron microprobe intensity maps showing chemical zonation patterns of Type 2 core/resorbed cores, Type 3 recharge bands, and Type 5 sector-zoned crystals. For Type 3 recharge bands, note the development of Cr-rich concentric growth zones on early-formed clinopyroxene cores, within the clinopyroxene mantle, and at the clinopyroxene rim.

Figure 4. Compositional ranges of clinopyroxene cores and mantles + rims are compared with the recharge bands. The Mg-number [Mg# = X_{Mg} / (X_{Mg} + X_{Fe2+}), where X is the cation fraction

and all iron is expressed as Fe^{2+}] of clinopyroxene is plotted against the sum of diopside + hedenbergite components (i.e., ΣDiHd) and the concentration of TiO_2.

Figure 5. Chondrite- (a) and primordial mantle- (b) normalized patterns of trace elements in clinopyroxene cores and mantles + rims. Normalization data are from Sun and McDonough (1989).

Figure 6. Trace element patterns in clinopyroxene cores are compared with those from recharge bands. Elements have been selected in order to represent different geochemical groups: 1) light rare earth elements (LREE; Ce and Eu), 2) heavy rare earth elements (HREE; Yb), 3) high field strength elements (HFSE; Zr), and 4) transition elements (TE; Cr and V). The Eu anomaly has been calculated as $Eu/Eu^* = Eu_N / (Sm_N \times Gd_N)^{0.5}$, where the subscript N indicates element concentrations normalized to the chondrite analysis reported in Sun and McDonough (1989).

Figure 7. *P* and *T* histograms obtained by clinopyroxene-based barometric and thermometric calculations performed by equilibrating clinopyroxene core and bulk rock compositions as described in Palummo et al. (2020).

Figure 8. Trace element patterns in clinopyroxene mantles + rims are compared with those from recharge bands. Elements have been selected in order to represent different geochemical groups: 1) light rare earth elements (LREE; Ce and Eu), 2) heavy rare earth elements (HREE; Yb), 3) high field strength elements (HFSE; Zr), and 4) transition elements (TE; Cr and V).

The Eu anomaly has been calculated as $Eu/Eu^* = Eu_N / (Sm_N \times Gd_N)^{0.5}$, where the subscript N indicates element concentrations normalized to the chondrite analysis reported in Sun and McDonough (1989).

Figure 9. Grey value diffusion profiles of two representative clinopyroxene crystals from shoshonite and rhyolite products (a). The diffusion profiles were calculated inside the blue area in the red box of the associated back-scattered electron (BSE) microphotograph. The analytical data set was modelled using the NIDIS code of Petrone et al. (2016) to quantify the time (Δt) elapsed between recharge band and the onset of eruption. Summary of all the time scales estimated through the application of NIDIS to clinopyroxene phenocrysts (b). Error bars represent minimum and maximum Δt uncertainties from NIDIS modeling.

Figure 10. Cr/Yb ratios measured for clinopyroxene cores, recharge bands, and mantles + rims are comparatively displayed in order to place constraints on the recharge processes and mixing dynamics governing the evolutionary history of magmas (a). Working model for the extended plumbing system at Vulcano Island and the dynamic growth of clinopyroxene from magmas exploring continuous physico-chemical changes due to the presence of interconnected reservoirs (b). Results from calculations based on the partitioning model of Mollo et al. (2018, 2020b) (c). The estimated values of La and Yb partitioning were used to invert the concentrations of REE in the melts from clinopyroxene cores and recharge bands. Different compositional vectors (i.e., colored arrows) represent the putative REE contents of end-member magmas in equilibrium with the more homogeneous clinopyroxene cores. The grey dashed symbols represent the putative REE contents of magmatic injections recorded by the more heterogeneous recharge bands.

Figures

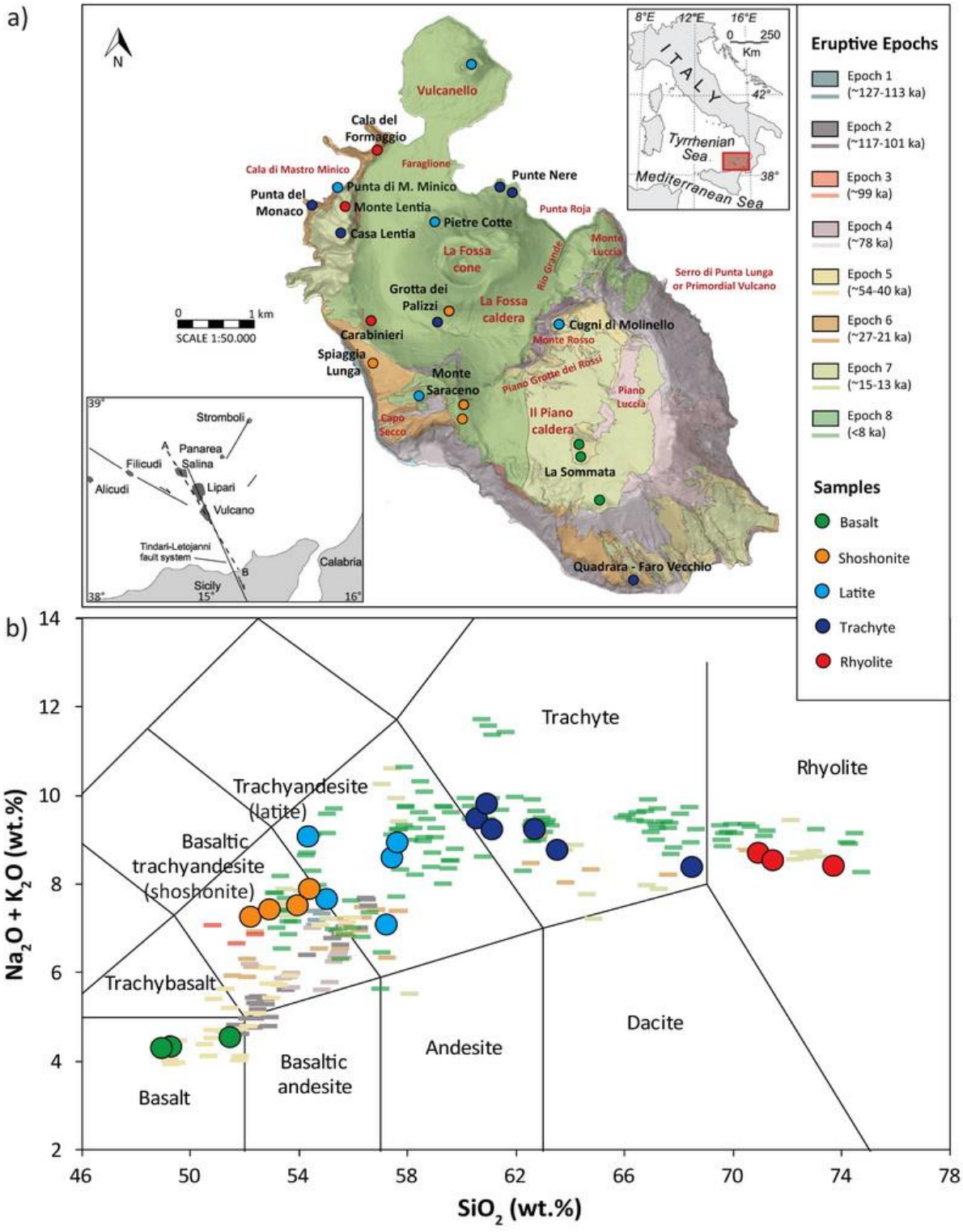

Figure 1

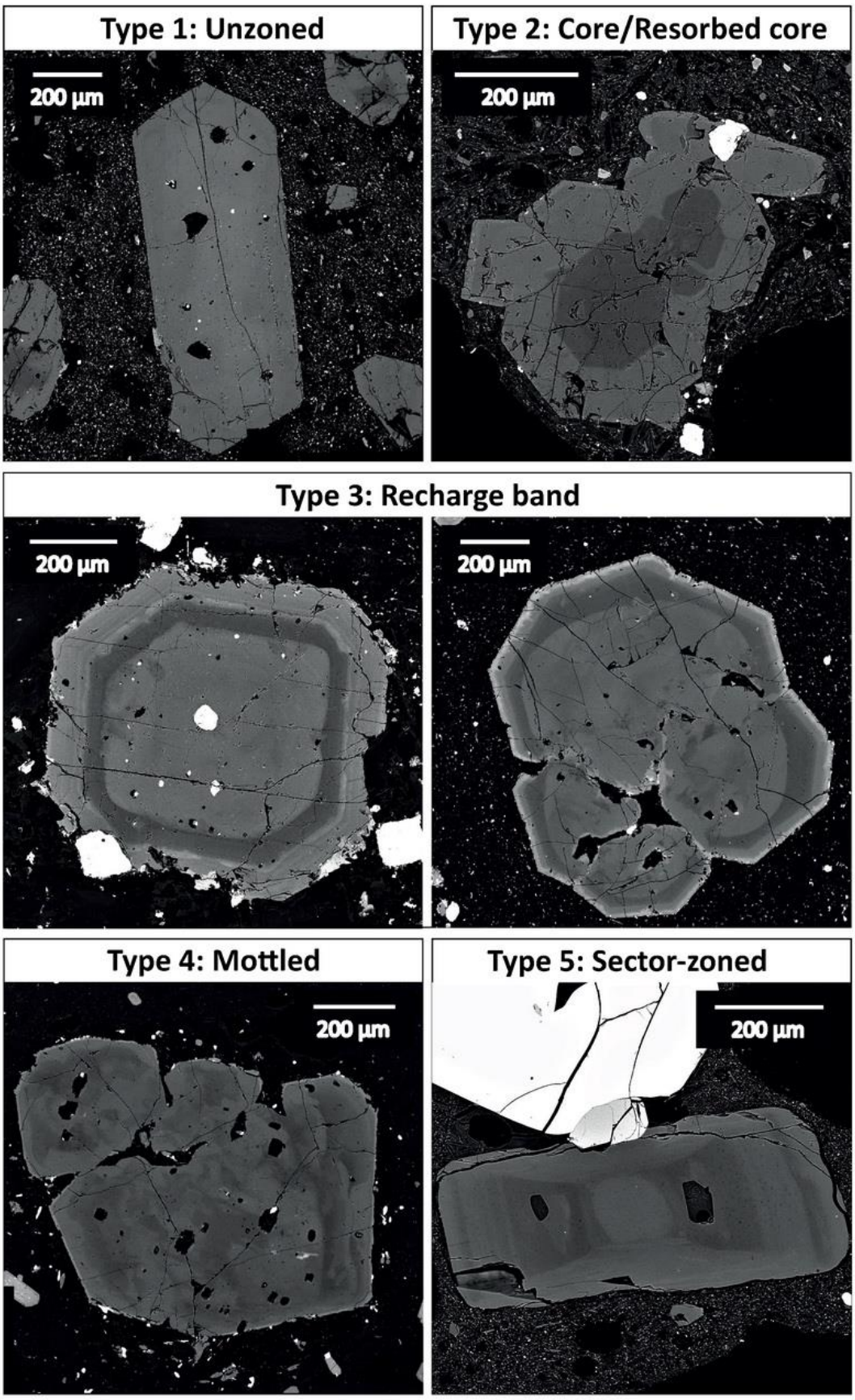
Type 1: Unzoned
200 µm
Type 2: Core/Resorbed core
200 µm
Type 3: Recharge band
200 µm
200 µm
Type 4: Mottled
200 µm
Type 5: Sector-zoned
200 µm

Figure 2

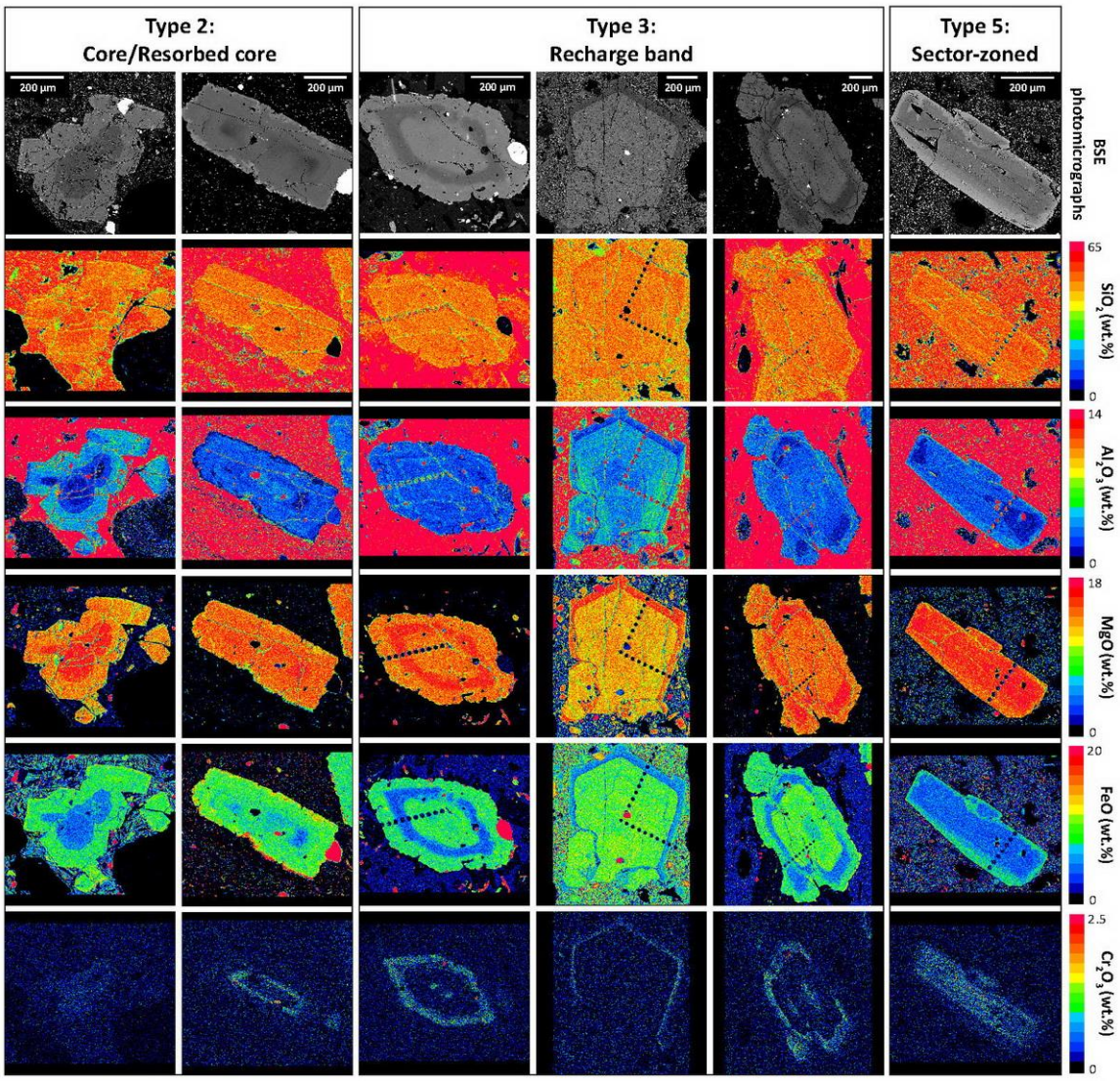
Type 2:
Core/Resorbed core
Type 3:
Recharge band
Type 5:
Sector-zoned
200 µm
BSE photomicrographs
65
SiO2 (wt.%)
0
14
Al2O3 (wt.%)
0
18
MgO (wt.%)
0
20
FeO (wt.%)
0
2.5
Cr2O3 (wt.%)
0

Figure 3

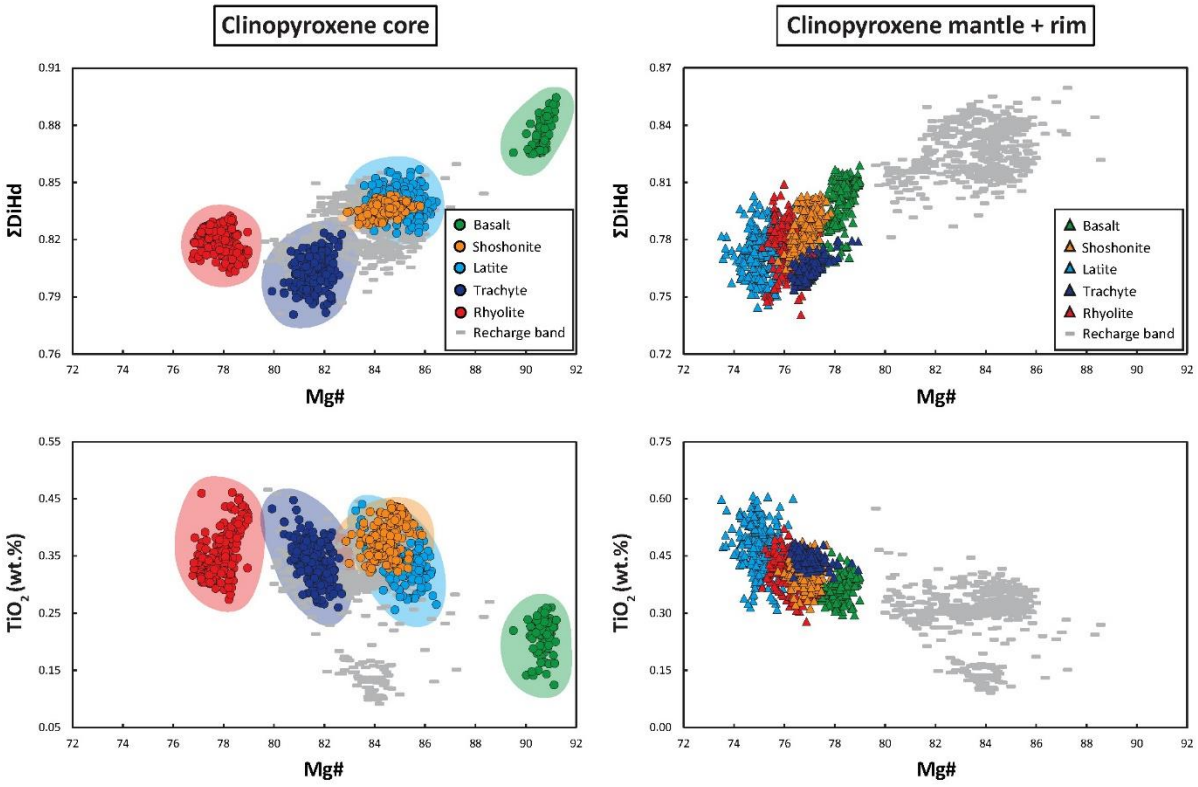

Figure 4

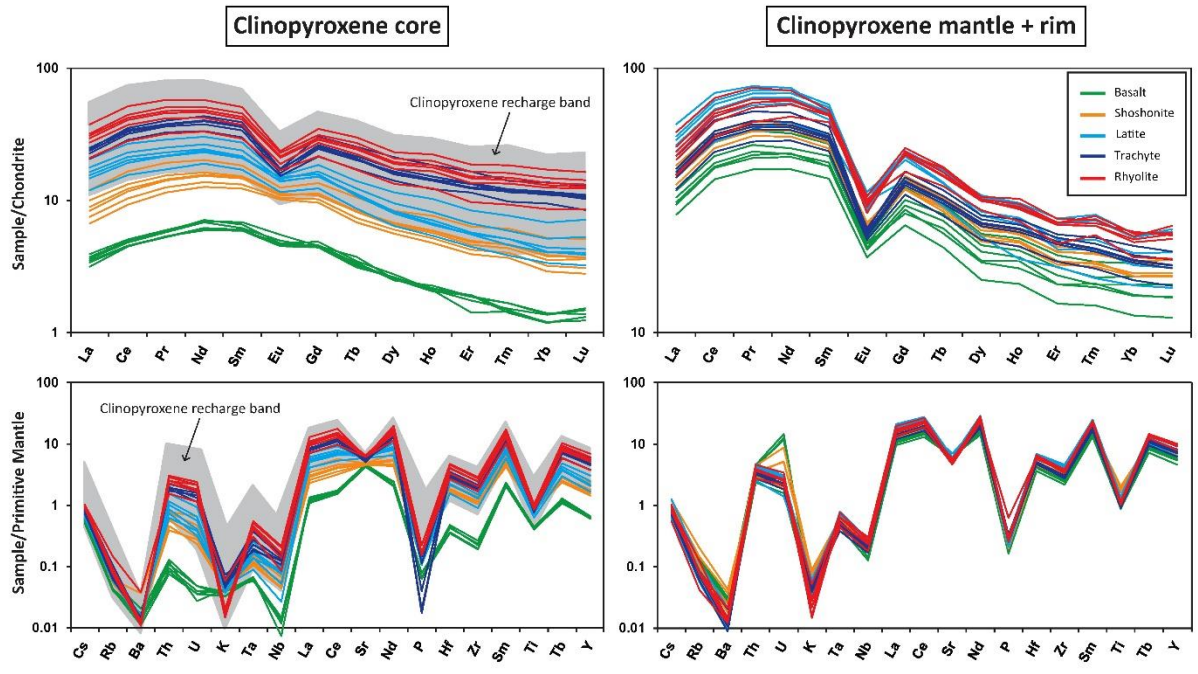

Figure 5

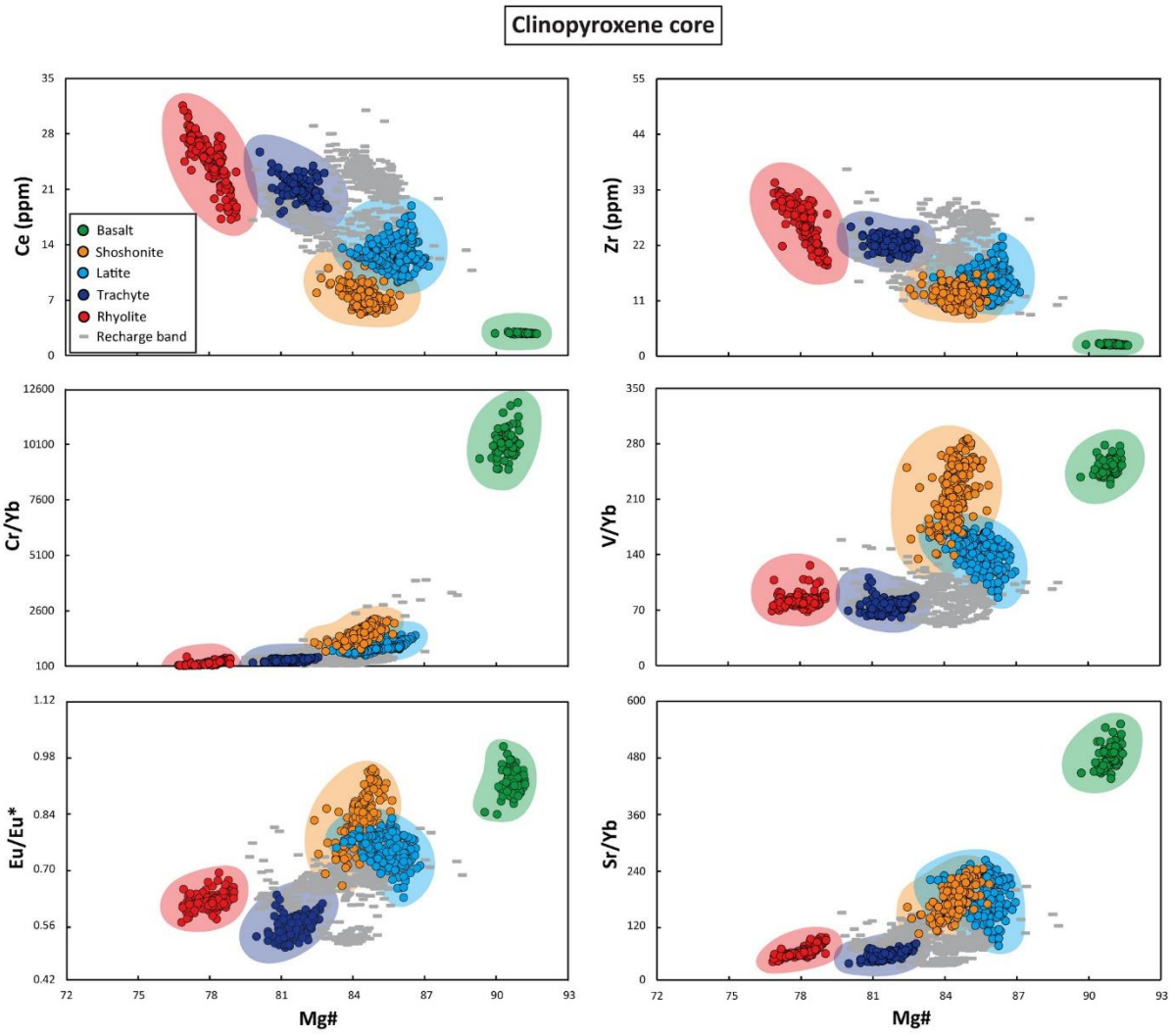

Figure 6

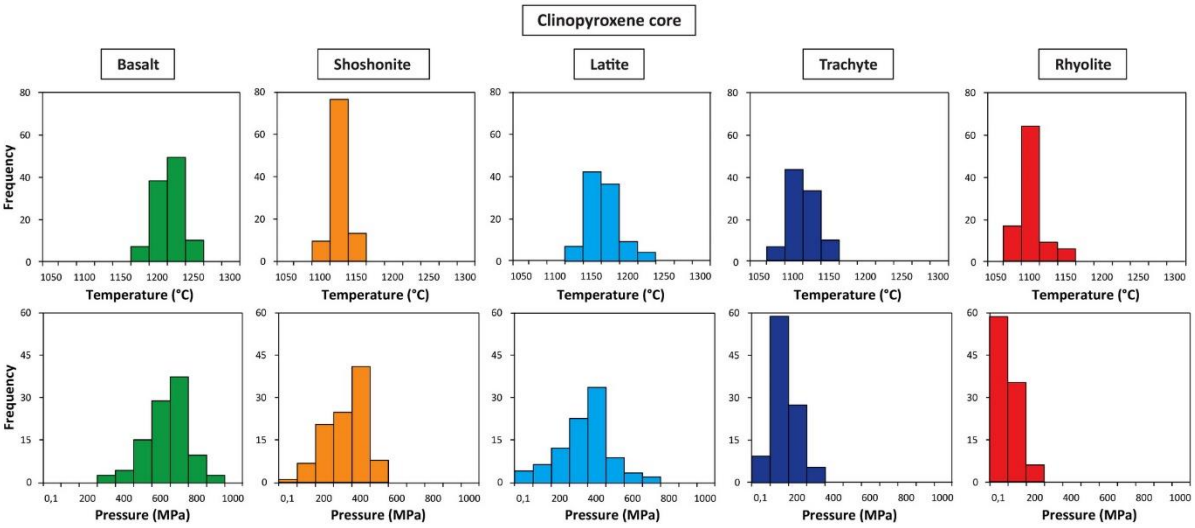

Figure 7

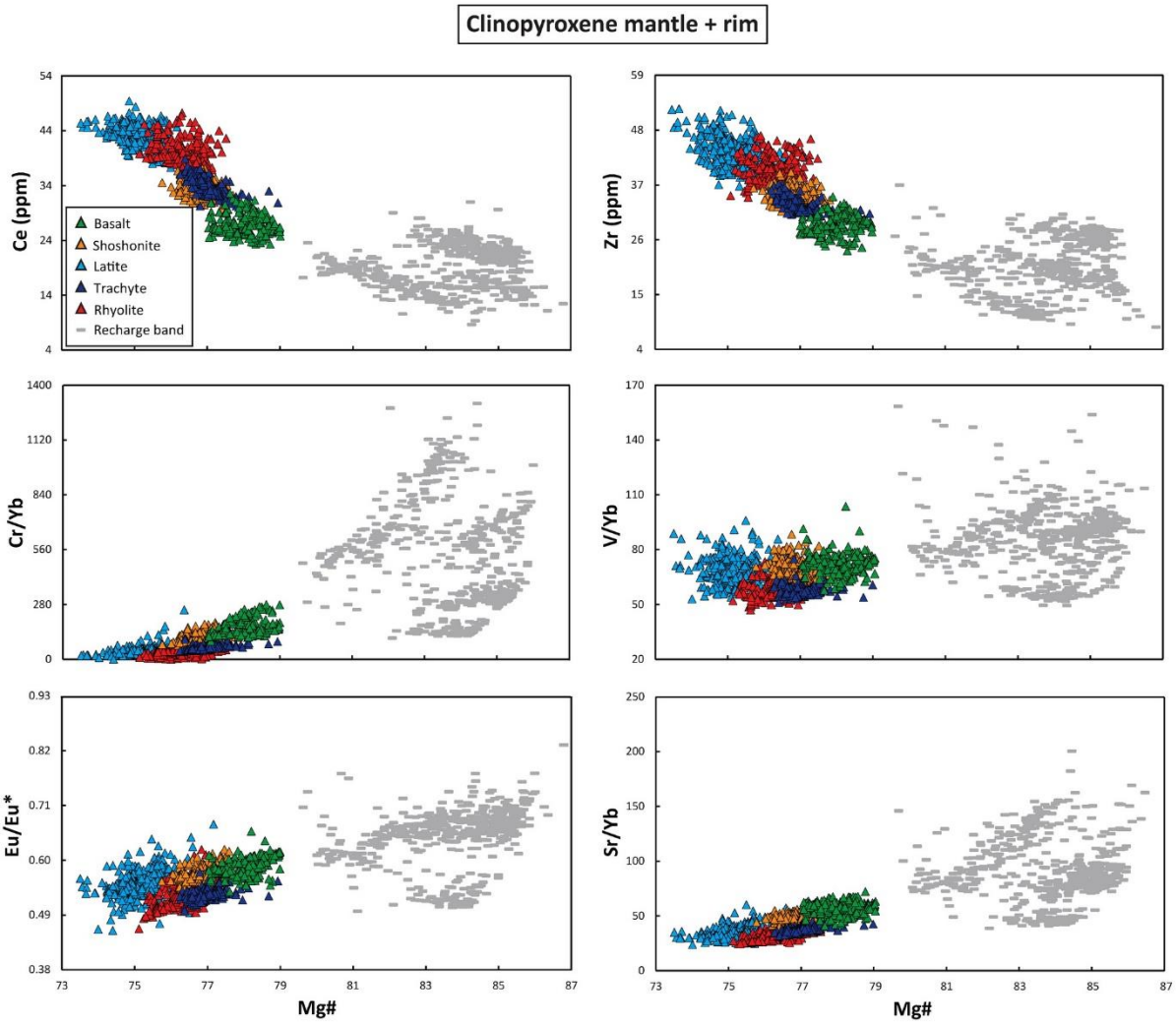
Clinopyroxene mantle + rim
Ce (ppm)
Zr (ppm)
Cr/Yb
V/Yb
Eu/Eu*
Sr/Yb
Mg#
Mg#
Basalt
Shoshonite
Latite
Trachyte
Rhyolite
Recharge band

Figure 8

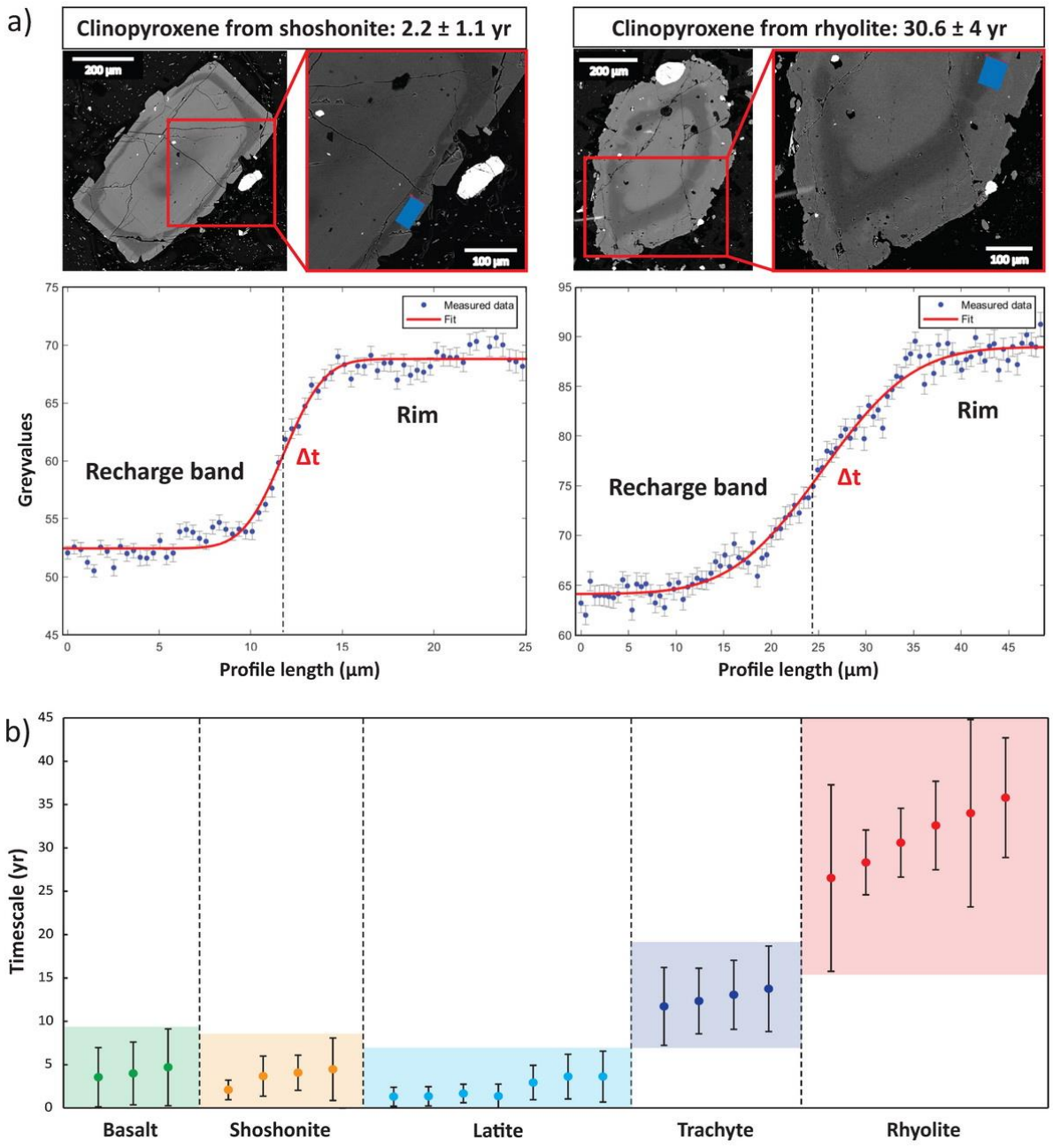
a)
Clinopyroxene from shoshonite: 2.2 ± 1.1 yr
Clinopyroxene from rhyolite: 30.6 ± 4 yr
200 µm
100 µm
Measured data
Fit
Greyvalues
Recharge band
Δt
Rim
Profile length (µm)
b)
Timescale (yr)
Basalt
Shoshonite
Latite
Trachyte
Rhyolite

Figure 9

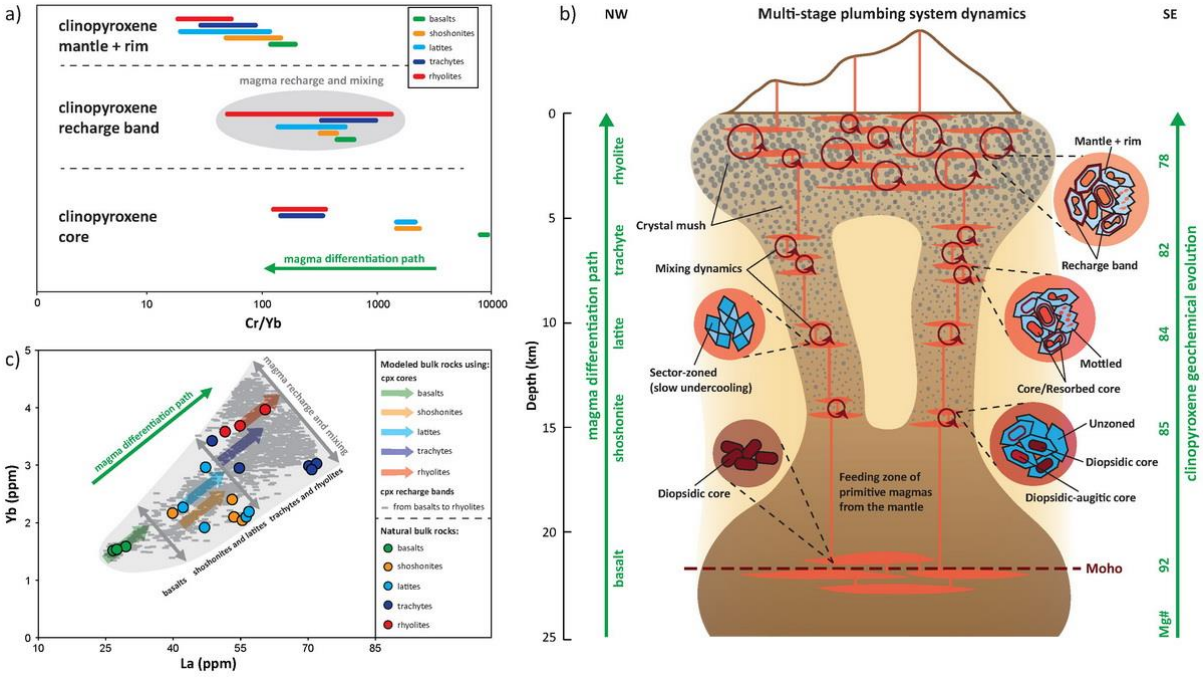

Figure 10

Supplementary data to this article can be found online at https://doi.org/10.1016/j.lithos.2021.106517.

Tables

Table 1: Textural features of clinopyroxene phenocrysts from basalts to rhyolites erupted at Vulcano Island in the last ~54 ka

Number of observations for each rock sample	**Host rock**	**Basalt**	**Basalt**	**Basalt**	**Shoshonite**	**Shoshonite**	**Shoshonite**	**Shoshonite**	**Latite**	**Latite**	**Latite**	**Latite**
	Eruptive Epoch	5	5	5	6	8	8	8	6	7	8	8
	Formation	La Sommata	La Sommata	La Sommata	Spiaggia Lunga	Monte Saraceno	Monte Saraceno	Grotta dei Palizzi	Mastro Minico	Cugni di Molinello	Monte Saraceno	Vulcanello
	Sample	*VL168/2*	*VL 168/12*	*VL 194/1*	*VL230/7*	*VL209.4/2*	*VL180*	*VL90/1*	*VL175B/1*	*VL144/2*	*VL213B/2*	*VL286*
	Type 1: unzoned crystals	9	8	9	7	6	-	-	-	-	-	-
	Type 2: cores/resorbed cores	7	8	7	7	8	9	8	8	9	10	11
	Type 3: recharge bands	-	6	6	7	8	8	9	10	10	10	10
	Type 4 : mottled crystals	-	-	-	6	6	7	6	7	6	7	6
	Type 5: sector-zoned crystals	-	-	-	6	6	6	6	7	7	6	6
	Host rock	**Latite**	**Trachyte**	**Trachyte**	**Trachyte**	**Trachyte**	**Trachyte**	**Trachyte**	**Rhyolite**	**Rhyolite**	**Rhyolite**	
	Eruptive Epoch	8	6	6	7	8	8	8	6	7	8	
	Formation	Pietre Cotte	Punta del Monaco	Quadrara	Casa Lentia	Punte Nere	Punte Nere	Grotta dei Palizzi	Cala del Formaggio	Monte Lentia	Carabinieri	
	Sample	*VL339/1*	*VL175C/3*	*VL229/6*	*VL183/10*	*VLPNa*	*VLPNb*	*VLP4*	*VL182/1*	*VL178/11A*	*VL181*	
	Type 1: unzoned crystals	-	-	-	-	-	-	-	-	-	-	
	Type 2: cores/resorbed cores	10	11	10	10	11	10	11	12	12	13	
	Type 3: recharge bands	11	11	12	11	12	11	12	13	12	12	
	Type 4 : mottled crystals	6	8	8	8	8	9	9	10	10	9	
	Type 5: sector-zoned crystals	6	-	-	-	-	-	-	-	-	-	

Conclusions

During the last decades, technological and methodological improvements have supported the progresses of geochemistry and petrology, as well as our knowledge about magma chamber processes. The picture emerging from these new considerations is consistent with a dynamic concept of interconnected ponding zones forming a plumbing system that extends vertically through the crust. This system is characterized by a multi-faceted geometry and comprises melt, crystals, and dissolved/exsolved volatiles that are heterogeneously distributed in space and time. This is accompanied by an increased knowledge on what petrology can provide about the determination of the intensive variables and timescales of processes governing the magmatic evolution.

In this PhD study, I have reconstructed the physico-chemical conditions driving the crystallization path of magmas erupted at Vulcano Island over a period of time from 54 to 8 ka. Mineral-melt equilibrium and thermodynamic models show that olivine appears as liquidus phase in mafic magmas, preferentially at high *P* and high melt-H_2O contents. Afterwards, the melt is cosaturated with clinopyroxene and, lastly, plagioclase. As the composition of magma evolves from basalt to rhyolite, the crystallization of clinopyroxene takes place at decreasing *P* and *T* conditions, delineating very well the presence of polybaric-polythermal magmatic reservoirs within the plumbing system. H_2O saturation in shallower magmatic reservoirs is a combined effect of magma uprising and late stage crystallization of anhydrous minerals. Titanomagnetite equilibrates with progressively more oxidized melts as the magma composition evolves. Mass balance calculations and major/trace element modeling indicate that basaltic to trachytic magmas are prevalently controlled by fractional crystallization processes and a variable degree of assimilation of crustal rocks. Conversely, rhyolitic and highly differentiated trachytic magmas are generated by extraction of interstitial melts from silicic mush zones.

Chemically zoned clinopyroxene phenocrysts cluster at different degrees of evolution. On the basis of textural and compositional changes, five distinct populations of clinopyroxene have been recognized (homogeneous crystals, core/resorbed cores, recharge bands, mottled crystals, and sector-zoned crystals). The hotter, lower crust is the most favorable location for the crystallization of diopsidic clinopyroxene cores. The compositional change of clinopyroxene proceeds from diopside-augite to augite, following the differentiation of basalts towards more differentiated melts residing in the upper crust. Augitic phenocrysts crystallize from highly differentiated trachytic and rhyolitic melts stored at very shallow crustal conditions. Recharge bands in clinopyroxene are markers of mafic, high-*T* magma injections into the shallow reservoirs, whereas resorbed cores are caused by partial dissolution and recrystallization via injections of hotter recharge melts. The number of chemical heterogeneities in clinopyroxene increases in trachytes and rhyolites. Fe-Mg diffusion chronology indicates that the residence time of clinopyroxene increases from ~0.1 to ~44 years from basalt to rhyolite, together with an increasing number of recharge bands. Protracted residence times are consistent with the tendency for clinopyroxene to remain suspended in more silicic and viscous melts extracted from shallow crystal-rich regions. Overall, the compositional zoning pattern of clinopyroxene presents a picture of plumbing system that characterized by distributions of melts and crystals which are progressively more evolved and heterogeneous in both space and time.

Acknowledgements

I would like to thank at first my supervisors, Prof. Silvio Mollo for his valuable advice, continuous support, and patience during my PhD study. His plentiful experience and fruitful discussions have encouraged me in all the time of my academic research. Many thanks also to

Dr. Gianfilippo De Astis for co-supervising all my research activities, providing important rock samples from Vulcano Island to start my work.

I thank Dr. Manuela Nazzari for her assistance with the electron microprobe and with the scanning electron microscope. I would like to express my gratitude to all people of High Pressure High Temperature (HP-HT) Laboratory of Geophysics and Volcanology of the Istituto Nazionale di Geofisica e Vulcanologia - Sezione di Roma 1.

I wish to thank Dr. Ben S. Ellis, Prof. Olivier Bachmann, Dr. Marcel Guillong, and Dr Oscar Laurent (Institute of Geochemistry and Petrology - ETHZ) for their assistance with laser ablation inductively coupled plasma mass spectrometry analyses and mapping and for the inspiring discussions. I am also grateful to Dr. Chiara Maria Petrone (Natural History Museum - London) for teaching me the NIDIS (Non-Isothermal Diffusion Incremental Step) model.